FACULTÉ DES SCIENCES

Jülich Centre for Neutron Science JCNS and Peter Grünberg Institut PGI
JCNS-2, PGI-4: Scattering Methods
"Lattice Dynamics in Emerging Functional Materials" group
Forschungszentrum Jülich GmbH

Lattice Dynamics of Nanostructured Thermoelectric Materials

Année académique 2012-2013

Dissertation présentée par
Tania Claudio Weber
en vue de l'obtention du grade de
Docteur en Sciences

2nd edition

“When you are courting a nice girl an hour seems like a second. When you sit on a red-hot cinder a second seems like an hour. That’s relativity.“ (Albert Einstein)

Acknowledgements

This PhD thesis could only be accomplished with the scientific, technical and emotional support of many people to whom I'm deeply grateful.

First of all, I'd like to express my special gratitude to my supervisor Dr. Raphaël P. Hermann and my co-supervisor Dr. Werner Schweika for giving me this opportunity, for all the guidance and very helpful input not only for scientific matters, but also for my personal and prospective career life.

I am thankful to all my collaborators who prepared and/or characterized the samples: Dr. G. Schierning, N. Stein, Dr. N. Petermann, Dr. H. Wiggers, Dr. R. Theissmann, Dr. C. S. Birkel, G. Kieslich, Dr. M. Panthöfer and Prof. Dr. W. Tremel.

My special gratitude to all the beamline scientists: Dr. I. Sergueev, Dr. H.-C. Wille, Dr. A. Chumakov, Dr. R. Rüffer, Dr. D. Robinson, Dr. M. M. Koza, Prof. H. Schober, Dr. F. Juranyi and Dr. J. Wuttke.

I am in debt to all my colleagues from JCNS-2 / PGI-4 for helpful scientific and technical discussions, especially Dr. D. Bessas, Dr. S. Disch, Drs. Andreas and Anne Houben, Dr. B. Klobes, Dr. K. Friese and Mr. B. Schmitz.

I'm also very thankful to my supervisors at the University of Liege, Prof. R. Cloots and Prof. F. Remacle.

Many thanks to my whole lovely family who have always supported me and without whom I would never be where I am today, and to my wonderful Jülich friends who made my life happier.

The Helmholtz Gemeinschaft Deutscher Forschungszentren is acknowledged for funding VH NG-407 "Lattice dynamics in emerging functional materials".

I'd like to express my eternal gratitude to the three people who were my rock during this period and gave me strength to accomplish everything I am today,

both professionally and personally. Dr. Gabi Schierning for being much more than a collaborator; Dr. Paula Bauer Pereira for being much more than a work colleague and a great friend; and the love of my life, Dieter Weber, for being not only a wonderful husband and father, but also my best friend.

And finally, I would like to thank God for giving me this amazing opportunity and providing me the strength to make the best of it.

Publication Dissertation

Chapter 2-5 of this dissertation are manuscripts that are published or will be submitted shortly.

Chapter 2:

Effects of Impurities on the Lattice Dynamics of Nanocrystalline Si for Thermoelectric Application

Claudio, T.; Schierning, G.; Theissmann, R.; Wiggers, H.; Schober, H.; Koza, M. M. and Hermann, R. P.

Journal of Materials Science, **48**:2836-2845, 2013.

Chapter 3:

Nanocrystalline Silicon: Lattice Dynamics and Enhanced Thermoelectric Properties

Claudio, T.; Stein, N.; Stroppa, D. G.; Klobes, B.; Koza, M. M.; Kudejova, P.; Petermann, N.; Wiggers, H.; Schierning, G. and Hermann, R. P.

Submitted to: Energy & Environmental Science

Chapter 4:

Lattice Dynamics and Thermoelectric Properties of Nanocrystalline $Si_{80}Ge_{20}$

Claudio, T.; Stein, N.; Stroppa, D. G.; Koza, M. M.; Petermann, N.; Wiggers, H.; Schierning, G. and Hermann, R. P.

Submitted to: Journal of Applied Physics

Chapter 5:

Enhanced Debye Level in nano $Zn_{1+x}Sb$, $FeSb_2$ and NiSb: Nuclear Inelastic Spectroscopy on ^{121}Sb

Claudio, T.; Bessas, D.; Birkel, C. S.; Kieslich, G.; Panthöfer, M.; Sergueev, I.; Tremel, W.; Hermann, R. P.

Submitted to: Physica Status Solidi

Abstract

In the wake of climate change, the development of more environmentally-friendly and energy-efficient devices has been the focus of much research. In this scenario, thermoelectric generators are an interesting option for waste heat recovery or for refrigeration. Up to now, the low efficiency of such generators, the high price and the use of toxic heavy metal compounds has confined thermoelectrics to niche applications.

A good thermoelectric material should possess a high Seebeck coefficient, high electrical conductivity and low thermal conductivity. One approach to improve the thermoelectric properties of a material is consequently to decrease the thermal conductivity by nanostructuration while avoiding a negative impact on electronic properties. A deeper understanding about the mechanisms behind a decrease on the thermal conductivity is achieved by a study about the lattice dynamics of nanostructured thermoelectric materials.

In this thesis it was demonstrated how for silicon and silicon-germanium alloys nanostructuration with a suitable process can increase the thermoelectric performance dramatically. The effects of nanostructuration on the lattice dynamics of antimonides were studied as well. Bulk nanocrystalline materials and nanopowder were investigated. The composition, microstructure and structural defects were analyzed with transmission electron microscopy, X-ray diffraction and pair distribution function analysis. The lattice dynamics of the bulk samples were investigated macroscopically with measurements of the heat capacity, elastic constants with resonant ultrasound spectroscopy, and thermal conductivity. Microscopically they were investigated with measurements of the density of phonon states with inelastic neutron scattering. The lattice dynamics of transition metal antimonides nanopowders was investigated microscopically through measurements of the element specific density of phonon states with nuclear inelastic scattering on ^{121}Sb.

Phosphorus doped Si and Si-Ge samples were produced by a gas phase synthesis and sintered into bulk pellets with spark plasma sintering. The influence of impurities, sintering time, and dopant concentration on the lattice dynamics and thermoelectric properties of these materials was analyzed.

It was found that exposing the nanopowder to air before sintering leads to a significant amount of SiO_2 and H impurities on the sample. An analysis of the SiO_2 content in the Si samples could be conducted since its contribution appeared as a Boson peak, which is characteristic for amorphous materials, in the lattice dynamics measurements. The thermal conductivity is strongly reduced due to nanostructuration and the incorporation of impurities, but such impurities also have a negative impact on the electronic properties of the material resulting in a non-optimal values of the thermoelectric figure of merit ZT.

Handling the nanopowder in an inert atmosphere throughout the production process resulted into nanocrystalline materials that were mostly free of impurities. The Si samples showed a dependence of the thermoelectric properties on sintering time and on initial nanoparticles size. A systematic decrease of the speed of sound was observed upon nanostructuration. When compared with previously reported results on nanocrystalline Si, the samples still present a somewhat large thermal conductivity, which compensated by a very high power factor resulted on a peak ZT of 0.57 at 973°C.

Similar measurements on nanocrystalline SiGe have shown that nanostructuration combined with a 20% substitution of Si atoms by Ge atoms causes a significant reduction on the speed of sound, resulting in a 50% reduction of the thermal conductivity when compared with the bulk material, and a peak ZT of 0.88 at 900°C, independently of the dopant concentration.

The study of the lattice dynamics of $Zn_{1+x}Sb$, $FeSb_2$ and NiSb nanopowders show a systematic increase of the Debye level when compared with the bulk counterpart and therefore a decrease of the speed of sound was also observed. Such study indicates that not only grain-boundaries can affect the lattice thermal conductivity of a material, but also a reduction on the speed of sound can be observed in the nanoparticles themselves.

Résumé

Dans le contexte du changement climatique global, le développement de technologies plus neutres sur le plan environnemental et plus efficaces sur le plan énergétique a fait l'objet de nombreuses recherches. Les générateurs récupérateur de chaleur résiduelle et les réfrigérateurs thermoélectriques constituent des options intéressante dans ce contexte. Cependant, jusqu'à présent la faible efficacité relative de tels générateurs, les coûts élevés et l'utilisation de composés à base de métaux lourds toxiques a restreint la thermoélectricité au rang d'application de niche.

Un bon matériau thermoélectrique devrait posséder un grand coefficient de Seebeck, une bonne conductivité électrique et une faible conductivité thermique. Une approche visant à améliorer les performances d'un matériau est par conséquent la diminution de la conductivité thermique par nanostructuration, pour autant que les propriétés électroniques ne soient pas affectées négativement. Une compréhension plus détaillée des mécanismes liés à une telle diminution de la conductivité thermique peut se faire par une étude de la dynamique de réseau des matériaux thermoélectriques nanostructurés.

Dans cette thèse nous montrons comment, pour le silicium et un alliage silicium-germanium, un processus adapté de nanostructuration peut améliorer les performances de façon appréciable. Les effets des nanostructures sur la dynamique de réseau de certains antimoniures ont également été étudiés. Des matériaux nanocrystallins massifs et des nanopoudres ont été examinés. La composition, la microstructure et les défauts structurels ont été analysés par microscopie électronique, par diffraction de rayons X et par analyse de la fonction de distribution de paires. La dynamique de réseau de matériaux massifs a été étudiée macroscopiquement par des mesures de chaleur spécifique, de constantes élastiques par l'utilisation de la spectroscopie de résonances d'ultrasons et de conductivité thermique. Microscopiquement, des mesures de la densité d'états de phonons par

la diffusion inélastique de neutrons a été utilisée. La dynamique de réseau de nanopoudres d'antimoniure de métaux de transition a été étudié microscopiquement par des mesures de la densité d'états de phonons élémentaire de l'antimoine en utilisant la diffusion nucléaire inélastique par ^{121}Sb.

Les échantillons de Si et Si-Ge dopés au phosphore ont été produits par une synthèse en phase gazeuse et agglomérés en pastilles massives par un frittage assisté par champs électrique. L'influence des impuretés, du temps de frittage et de la concentration en dopant sur la dynamique de réseau à été étudiée.

Il apparaît que l'exposition des nanopoudres à l'air avant frittage conduit à une quantité importante d'impuretés SiO_2 et H dans les échantillons. Une analyse du contenu en SiO_2 dans les échantillons de silicium a pu être réalisée car dans les mesures de dynamique de réseau il conduit à l'apparition d'un pic de bosons caractéristique de matériaux amorphes. La conductivité thermique est fortement réduite à cause des nanostructures et de l'incorporation d'impuretés, mais ces impuretés influencent négativement les propriétés électroniques du matériau, ce qui résulte en des valeurs suboptimales pour le facteur de qualité thermoélectrique, ZT.

Une manipulation des nanopoudres en atmosphère inerte durant tout le processus de production résulte en un matériau nanocrystallin essentiellement dépourvu d'impuretés. Les échantillons de Si montrent que les propriétés thermoélectriques dépendent du temps de frittage et de la taille initiale des nanoparticules. Une réduction systématique de la vitesse du son est observée. En comparaison avec des résultats antérieurs pour le Si nanocrystallin, les échantillons ont toujours une conductivité thermique assez grande qui compense partiellement un facteur de puissance très important, pour résulter finalement un facteur de qualité thermoélectrique pic de $ZT = 0.57$ à 973°C.

Des mesures similaires effectuées sur SiGe nanocrystallin montrent que la nanostructuration combinée avec une substitution de 20% de Si par Ge provoque une réduction de la vitesse du son et résulte en une réduction de 50% de la conductivité thermique en comparaison du matériau massif. Un maximum de $ZT = 0.88$ est observé à 900°C, indépendamment de la concentration en dopant.

L'étude de la dynamique de réseau dans $Zn_{1+x}Sb$, $FeSb_2$ et NiSb indique une augmentation systématique du niveau de Debye en comparaison avec la contrepartie

massive et ainsi une diminution de la vitesse du son. Cette étude indique que en plus des joints de grains qui affectent la conductivité thermique d'un matériau, une réduction systématique de la vitesse du son est observée également dans les nanoparticules elles-mêmes.

Kurzfassung

Wegen des Klimawandels ist die Forschung in letzter Zeit stark auf umweltfreundliche und energieeffiziente Technologien fokussiert. Thermoelektrische Generatoren sind in diesem Szenario eine interessante Möglichkeit, um Abwärme zu nutzen oder um zu kühlen. Bis jetzt stehen die geringe Effizienz, der hohe Preis und die Verwendung von toxischen Schwermetallverbindungen einer breiten Anwendung im Wege.

Ein gutes Material für thermoelektrische Anwendungen soll einen hohen Seebeck-Koeffizienten, eine hohe elektrische Leitfähigkeit und eine geringe thermische Leitfähigkeit haben. Konsequenterweise kann ein thermoelektrisches Material verbessert werden, indem man durch Nanostrukturierung die thermische Leitfähigkeit herabsetzt, ohne die elektronischen Eigenschaften zu verschlechtern. Durch Untersuchung der Gitterdynamik nanostrukturierter Thermoelektrika können die Mechanismen, welche die thermische Leitfähigkeit reduzieren, besser verstanden werden.

In dieser Arbeit wird gezeigt, wie Nanostrukturierung von Silizium und Silizium-Germanium-Legierungen mit einem geeigneten Prozess die thermoelektrische Leistungsfähigkeit dramatisch verbessern kann. Der Einfluss von Nanostrukturierung auf die Gitterdynamik von Antimoniden wurde ebenfalls erforscht. Untersucht wurden sowohl Nanopulver als auch gesintertes nanostrukturiertes Material. Die Zusammensetzung, Mikrostruktur und Defekte wurden mit Transmissionselektronenmikroskopie, Röntgendiffraktometrie und einer Bestimmung der Paarverteilungsfunktion analysiert. Die Gitterdynamik wurde makroskopisch durch Messungen der Wärmekapazität, der Elastizitätsmodule mittles Ultraschallresonanzspektroskopie und der Wärmeleitfähigkeit aufgeklärt. Mikroskopisch wurde die Phononen-zustandsdichte mit inelastischer Neutronenstreuung gemessen. Für Übergangsmetalantimonide in Form von Nanopulvern wurde die elementspezifische Phononen-Zustandsdichte von ^{121}Sb mit inelastischer Kernresonanzstreuung bestimmt.

Phosphordotiertes Nanopulver aus Silizium und einer Silizium-Germanium-Legierung wurde aus der Gasphase synthetisiert und dann mit Funkenplasma-Sintern zu Presslingen verdichtet. Der Einfluss von Verunreinigungen, Sinterzeit und Dotierkonzentration auf die Gitterdynamik und die thermoelektrischen Eigenschaften wurden analysiert.

Es stellte sich heraus, dass signifikante Mengen von SiO_2 und Wasserstoff als Verunreinigung in die Proben gelangen, wenn das Nanopulver vor dem Sintern der Luft ausgesetzt war. Der SiO_2-Gehalt in Silizium-Proben konnte bestimmt werden, weil SiO_2 zu einem Bosonen-Peak in der Zustandsdichte führt, was charakteristisch für ein amorphes Material ist. Die Nanostrukturierung verringert zusammen mit den Verunreinigungen die thermische Leitfähigkeit stark, aber die Kontamination verschlechtert ebenfalls die elektronischen Eigenschaften. Dadurch ist die thermoelektrische Gütezahl nicht optimal.

Wenn das Nanopulver während des Herstellungsprozesses unter Schutzgas gehandhabt wird, können weitgehend verunreinigungsfreie nanokristalline Materialien erzeugt werden. Bei den Silizium-Proben hat die Sinterzeit und die Partikelgröße der Nanopartikel einen Einfluss auf die thermoelektrischen Eigenschaften. Nanostrukturierung verringert die Schallgeschwindigkeit systematisch. Im Vergleich zu Literatur-Ergebnissen über nanostrukturiertes Silizium haben die Proben immer noch eine vergleichsweise hohe thermische Leitfähigkeit, aber im Ausgleich einen sehr hohen Leistungsfaktor. Die Gütezahl, ZT, erreicht im Ergebnis ihr Maximum von 0.57 bei 973°C.

Ähnliche Messungen an nanokristallinem SiGe haben gezeigt, dass Nanostrukturierung zusammen mit 20% Substituierung von Silizium durch Germanium die Schallgeschwindigkeit signifikant reduziert, die thermische Leitfähigkeit im Vergleich zu unstrukturiertem Material halbiert, und zu einer maximalen Gütezahl von 0.88 bei 900°C führt, unabhängig von der Dotierstoffkonzentration.

Die Untersuchung der Gitterdynamik von $Zn_{1+x}Sb$, $FeSb_2$ and NiSb in Form von Nanopulvern hat ergeben, dass das Debye-Niveau im Vergleich zu makrokristallinen Proben erhöht und damit die Schallgeschwindigkeit reduziert ist. Diese Ergebnisse zeigen, dass nicht nur die Korngrenzen die thermische Leitfähigkeit beeinflussen, sondern dass die Schallgeschwindgkeit auch in den Nanopartikeln selbst herabgesetzt ist.

Contents

List of Figures

List of Tables

Chapter 1

Introduction

In recent years, climate change has been the highlight of many discussions throughout the media, scientific communities, political debates, etc. The main consensus to stop climate change was established to be a global decrease in greenhouse gases emissions by using more energy efficient means and decarbonization, *i.e.* reduction of carbon intensity in primary energy over time, drawing a lot of attention to research in the area of renewable and sustainable energy [1].

In this scenario, thermoelectric generators (TEGs) provide an opportunity for waste heat recovery and environmentally-friendly refrigeration. The main advantage of TEGs lies in the fact that the power is derived from heat which would otherwise dissipate into its surroundings, *e.g.* from burners, exhaust systems of automobiles, etc. Another advantage is that they are made of solid-state constructions, which make them highly durable. But TEGs still didn't reach their whole potential due to high costs and low efficiency. Therefore research on the improvement of the efficiency of low cost thermoelectric materials is highly required.

1.1 Thermoelectricity

Thermoelectric devices provide cooling through the Peltier effect when an applied current pumps heat from the cold side at a temperature T_C towards the hot side at T_H (Figure 3.5 A [2]), or they recover waste heat by drawing electrical power from a thermal gradient through the Seebeck effect (Figure 3.5 B [2]).

A conversion module is made of several p-type and n-type thermocouple legs thermally in parallel and electrically in series (Figure 3.5 C [2]). A Seebeck voltage appears when the junctions are kept at different temperatures, and an open circuit electromotive force, emf, is generated: $V = S(T_1 - T_2)$. The Seebeck coefficient is thus defined as $S = V/\Delta T$.

The Peltier effect describes the reverse situation, when an external emf source is applied and a current (I) flowing through the junctions causes a temperature difference, with a rate of heating $\dot{Q}$ and the Peltier coefficient is given by $\pi = \dot{Q}/I$.

The Seebeck and the Peltier effects are related by the Kelvin relationship: $S = \pi/T$.

The maximum efficiency of a thermoelectric device (ϕ_{max}) is given by the product of the Carnot efficiency ($\eta_c < 1$) and a value related to the material's parameters (γ).

$$\phi_{max} = \eta_c \gamma \tag{1.1}$$

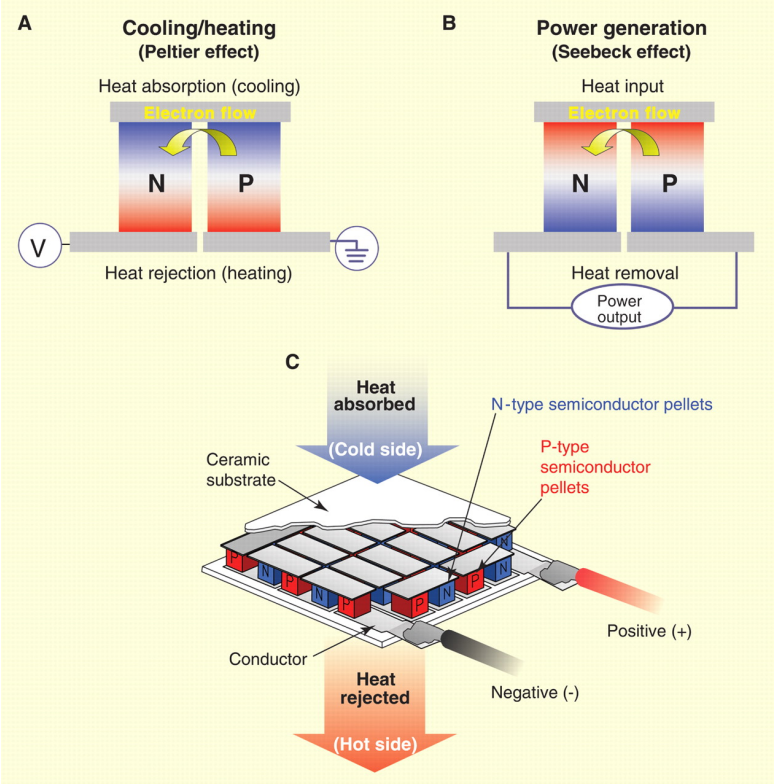

Figure 1.1: A) Cooling: an applied current transports heat through the material (Peltier effect); B) Heat recovery: generation of electrical power from a heat gradient (Seebeck effect); C) TE generators: connect large numbers of junctions in series to increase operating voltage and spread heat flow. Reproduced from Ref. [2].

Where $\eta_c = \frac{T_H - T_C}{T_H}$ and $\gamma = \frac{\sqrt{1+Z_c\overline{T}}-1}{\sqrt{1+Z_c\overline{T}}+\frac{T_C}{T_H}}$, with the average temperature $\overline{T} = \frac{T_H+T_C}{2}$ and the only parameter which explicitly includes the materials properties $Z_c = \frac{S^2\sigma}{\kappa}$ where S is the Seebeck coefficient, σ is the electrical conductivity and κ is the thermal conductivity.

The material's parameters (γ) comes from the maximization of the efficiency of a generator, *i.e.*, the electrical input divided by the heat adsorbed at the hot side.

Since a thermoelectric couple is produced with a p- and a n-doped leg, the geometries and material constants of both thermocouple legs are usually the same, and the concept of an average dimensionless figure of merit can be employed and is given by

$$ZT = \frac{S^2\sigma}{\kappa}T \tag{1.2}$$

A good thermoelectric material should therefore possess a large Seebeck coefficient, S, a large electrical conductivity σ, and low thermal conductivity κ in order to maximize the dimensionless figure of merit for the thermoelectric performance of a material [3, 4, 5]. In other words, it should behave as an phonon-glass electron-crystal [6, 7, 8].

The thermal conductivity can be divided into an electronic and an lattice contribution:

$$\kappa = \kappa_{el} + \kappa_{lat} \tag{1.3}$$

The electronic contribution to the thermal conductivity is directly related to the electrical resistivity (ρ): $\kappa_{el} = \frac{LT}{\rho}$ where L is the Lorentz number [1]. Therefore reducing the lattice contribution to the thermal conductivity is a natural way to improve the performance of a thermoelectric material, and can be achieved by nanostructuration, among others methods [9], where additional scattering centers for phonons at grain boundaries are created.

In this work an in-depth study on the effects of nanostructuration on the lattice dynamics of known thermoelectric materials as shown in Figure 1.2 [10], will be presented and correlated to the implications of nanostructuration on the decrease of the lattice thermal conductivity.

[1] More details about this thermal transport will be given in Section 1.3.2.3

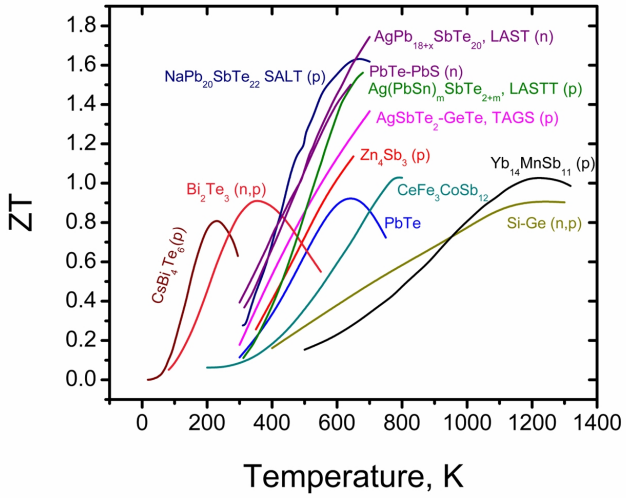

Figure 1.2: Dimensionless figure of merit (ZT) of selected thermoelectric materials. Reproduced from Ref. [10].

1.2 Materials

1.2.1 Silicon, Germanium and their Alloys

Si and Ge have the diamond crystal structure (space group $Fd\bar{3}m$). They differ in lattice constant (5.431 Å for Si and 5.6512 Å for Ge) and are miscible at all ratios, forming a solid solution.

Both materials are widely used semiconductors for electronics, since the conductivity and electronic properties of those materials can be easily adjusted by doping with elements such as phosphorus and boron. The materials themselves and also precursor materials for gas phase synthesis are therefore available in industrial quantities and at exceptional purity and quality for a comparatively low price. The entire technology around silicon – synthesis, machining, etching, doping and so on – is well-established and silicon is one of the most studied and simplest model materials in solid state physics, for which reference data is therefore abundant.

Silicon has furthermore attractive chemical properties for many applications. It passivates with a very thin and stable layer of amorphous SiO_2 when in contact with oxygen or water, which prevents further oxidation. At higher temperature, this layer grows thicker, but still prevents bulk oxidation even in air at temperatures up to 1000 °C. Silicon is non-toxic und

unproblematic from a safety and environmental point of view, unlike other thermoelectric materials that are lead or tellurium based.

Pure silicon and germanium have a very high lattice thermal conductivity [1] due to their low density and high Young's modulus, which is a direct result of their lattice structure with stiff tetrahedral covalent bonds connecting the atoms, resulting in a hard and brittle material (see section 1.3.2).[2] This has a negative impact on the thermoelectric figure of merit of pure silicon and germanium. Lowering the lattice thermal conductivity of silicon or germanium with nanostructuration has potentially a large impact on the thermoelectric properties.

Alloys of Si and Ge have a competitive figure of merit at high temperatures [3, 4, 12]; and silicon nanowires with a rough surface has been reported to present a drastic reduction in thermal conductivity resulting in a $ZT \approx 0.6$ to 1 at room temperature [13, 14]. Silicon and germanium have a very different atomic mass, so that alloying creates scattering centers for phonons, resulting in a $\kappa_{\mathrm{SiGe}} = 4 - 5\,\mathrm{W/K\text{-}m}$ at room temperature [15]. The principle of "phonon glass, electron crystal" is therefore fulfilled in Si-Ge alloys.

The sensitivity of silicon and germanium to surface oxidation can be a problem for handling nanopowders. Upon contact with air, they immediately react and form an oxide surface layer. Furthermore, they adsorb water from moist air. Due to the high surface area of nanopowders, this can be a significant fraction of the material. For that reason, nanopowders have to be stored and handled in an inert atmosphere. Once the powder is sintered into a dense pellet, it is not sensitive anymore.

In this thesis the lattice dynamics of nanocrystalline Si, Ge and SiGe samples prepared by collaborators by a gas phase synthesis followed by spark plasma sintering, was studied.

1.2.2 Antimonides: $Zn_{1+x}Sb$, $FeSb_2$ and NiSb

Transition metal antimonides such as Zn_4Sb_3, $FeSb_2$ and NiSb belong to the big family of semiconducting compounds of metals with pnictides or chalcogens. They are narrow-gap semiconductors, which makes them candidate materials for thermoelectric applications at low and intermediate temperature. The band gap of a thermoelectric materials should be sufficiently large in order to have only a single carrier type (p- or n-type material) but also small enough to have a reasonably high electrical conductivity at the operating temperature.

[1] At room temperature, $\kappa_{\mathrm{Si}} = 156\,\mathrm{W/m\text{-}K}$ and $\kappa_{\mathrm{Ge}} = 60\,\mathrm{W/m\text{-}K}$ [11].

[2] Diamond with a similar structure, but even lower density and higher Young's modulus, is one of the best heat conductors ($\kappa = 2200\,\mathrm{W/m\text{-}K}$), about five times better than silver.

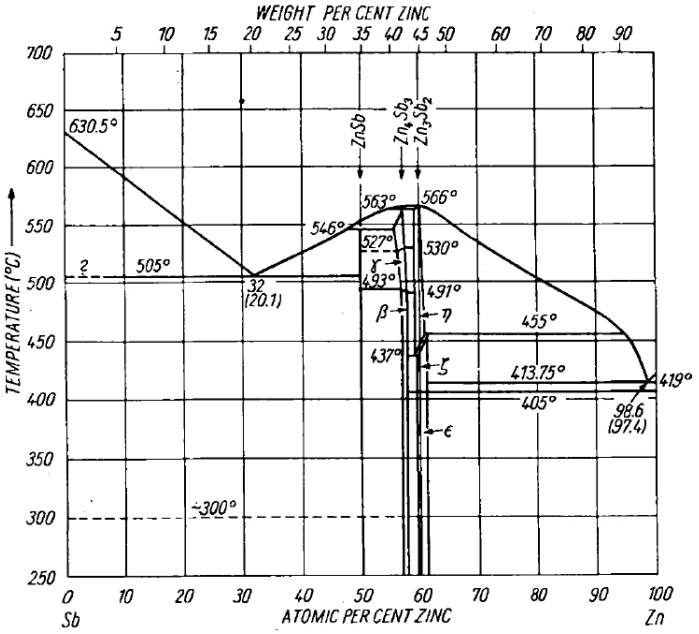

Figure 1.3: Zn-Sb phase diagram. Reproduced from Ref. [16].

The complex phase diagram of Zn with Sb (Figure 1.3 [16]) shows a number of intermetallic phases between the compositions ZnSb and Zn_3Sb_2. Zn_4Sb_3 [1] (space group $R\bar{3}c$ with $a = 12.2282$ and $c = 12.4067$ Å) is a well known thermoelectric material [17, 18] used from room temperature up to approximately 700 K. Due to a very low thermal conductivity [17, 18], Zn_4Sb_3 exhibits an outstanding figure of merit between 450 and 670 K with $ZT \approx 1.3$ at 670 K. When trying to synthesize nanoparticles of this phase with a wet chemistry approach, Birkel *et. al.* [19] obtained a new phase "$Zn_{1+x}Sb$" according to electron diffraction tomography results. These particles were analyzed with nuclear inelastic scattering and the results are presented in this thesis.

The phase diagram of Fe with Sb is much simpler (Figure 1.4 [20]). Besides a solid solution of low Sb amounts in a Fe host phase, the Fe-Sb phase diagram features two intermetallic phases, $FeSb_{1+x}$ (ε) and $FeSb_2$. $FeSb_2$ (space group $Pnnm$ with $a = 5.820$, $b = 6.519$ and $c = 3.188$ Å) decomposes into FeSb and a Sb-rich melt at 1011 K and can therefore not be grown from a stoichiometric melt. It is possible to obtain this phase from a melt with surplus Sb in accordance with the phase diagram.

Bentien *et al.* [21] reported a colossal Seebeck coefficient at 10 K in strongly correlated $FeSb_2$ of approx. $45000\,\mu VK^{-1}$ giving a record value for the thermoelectric power factor

[1] The precise stoichiometry of Zn_4Sb_3 is actually $Zn_{3.95(5)}Sb_3$ [7].

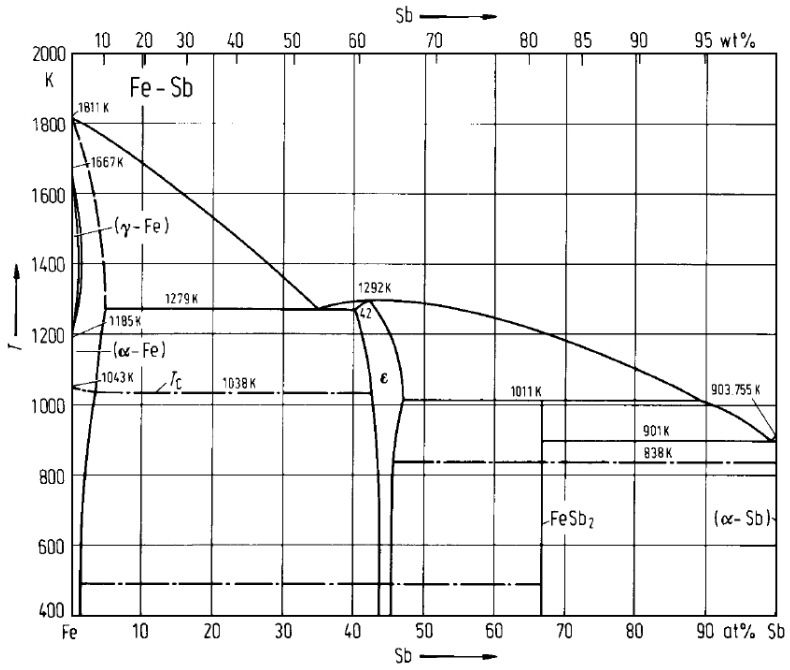

Figure 1.4: Fe-Sb phase diagram. Reproduced from Ref. [20].

(S^2/ρ) of approx. $2300\,\mu\mathrm{WK^{-2}cm^{-1}}$ at 12 K. However, the lattice thermal conductivity is too large and the dimensionless thermoelectric figure of merit is only 0.005 at 12 K.

Furthermore, the density of phonon states and thermoelectric properties of bulk $FeSb_2$ was previously characterized experimentally and by first principles calculations [22]. Comparison of the nanostructured materials with the bulk is therefore easily achievable.

The phase diagram of Ni with Sb (Figure 1.5 [23]) resembles the phase diagram of Fe with Sb on the Sb rich side, but on the Ni rich side it features a number of complex phases and solid state phase transition, including a peritectoid and two eutectics from melt, some phases which are only stable at lower temperatures and a number of solid state phases. But on the case of NiSb (space group $P6_3/mmc$ with $a = 3.934$ and $c = 5.138\,\text{Å}$), it is a rather simple and has stable stoichiometric compound with a sizable phase width and a rather high melting point.

Both, $FeSb_2$ and NiSb present not only interesting or potentially interesting thermoelectric properties, but also are potential anode materials in rechargeable lithium-ion batteries [24, 25, 26]. In this thesis, nanoparticles of $FeSb_2$ [27] and NiSb [28] prepared by collaborators with wet chemistry synthesis were analyzed.

All three antimonides decompose or melt at relatively low temperature and are therefore

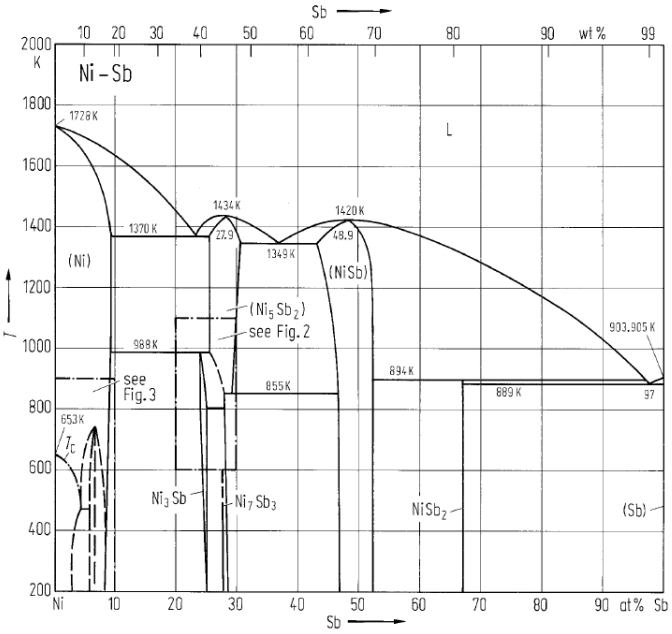

Figure 1.5: Ni-Sb phase diagram. Reproduced from Ref. [23].

not usable at high temperature. Furthermore, sintering parameters of the nanoparticles have to be carefully adjusted to avoid decomposition.

1.3 Measurement Techniques

All the samples were produced by collaborators and a study of their crystal structure or microstructure was done by means of X-Ray Diffraction (XRD) and Pair Distribution Function analysis (PDF). The lattice dynamics were studied both macroscopically by measurements of the heat capacity, the elastic constants with Resonant Ultrasound Spectroscopy (RUS) and the thermal conductivity; and microscopically with measurements of the total and partial Density of Phonon States (DPS) using Inelastic Neutron Scattering (INS) and Nuclear Inelastic Scattering (NIS), respectively.

In this section, these measurement techniques are described and a brief overview of the experimental method is given.

Further characterization methods which are presented in the articles such as Transmission Electron Microscopic (TEM), Prompt Gamma Ray Activation Analysis (PGAA) [29] and high temperature thermoelectric measurements were performed by collaborators and will not be described in this thesis.

1.3.1 Structural Analysis: X-Ray Diffraction (XRD) and Pair Distribution Function Analysis (PDF)

In 1913, Sir William Henry Bragg and Sir William Lawrence Bragg (father and son) established a relationship that explains the diffraction patterns observed when X-ray beams were scattered on a crystalline structure, for which they later were awarded the Nobel Prize (1915):

$$n\lambda = 2d_{hkl}\sin\theta \tag{1.4}$$

where n is an integer (order of diffraction), λ is the wavelength of the incident beam, d_{hkl} is the interplanar spacing, h k and l are the Miller indices of the Bragg plane and θ is the diffraction angle. This relationship describes why X-rays with a certain specific wavelength incident into a crystal in a certain angle produces intense peaks of reflected radiation (known as Bragg peaks).

Bragg's law was first used to explain the interference pattern of X-rays scattered by crystals, but since then, diffraction has been developed to study the structure of all states of matter with any beam type, *e.g.*, ions, electrons, neutrons and protons, as long as the wavelength is similar to the distance between the atomic or molecular structures of interest.

Nowadays, diffraction can be performed on powder and polycrystalline materials, single crystals, amorphous materials, thin films multilayers and others, and it is used not only to determine how the atoms are arranged in a crystal, but also further analysis of the diffraction pattern yields information about phase composition, preferred orientation, strain, nanocrystallite sizes, thin film thickness and periodicity, etc. Such analysis can be perform *e.g.* by doing a refinement of the XRD pattern using the Rietiveld method [30].

An estimation of the nanocrystallite sizes and strain on a sample can be obtain from the line broadening of the diffraction peaks. Although most fitting programs give the Full Width Half Maximum (FWHM), the width parameter used to obtain size and strain is the integral breadth located at 2θ (β) given in radians, which can be calculated from the FWHM (Γ) depending on the peak shape, $\beta = (\pi/2)\Gamma$ for Lorentzian and $\beta = \{\pi/(4\ln 2)\}^{1/2}\Gamma$ for Gaussian.

The nanocrystallite sizes can be obtain using the Scherrer formula [31], $D_V = \frac{K\lambda}{\beta_{size}\cos\theta}$ and the weighted average strain ε_{str} was obtained by Stokes and Wilson [32] as $\varepsilon_{str} = \beta_{strain}/\{4\tan\theta\}$, where D_V is the volume weighted crystallite size, K is the Scherrer constant (usually close to unity) and λ is the wavelength of the radiation. Since the size and the strain

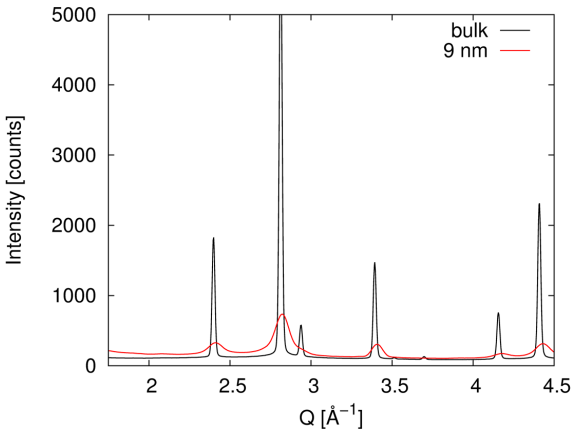

Figure 1.6: X-ray diffraction pattern for bulk magnetite and iron oxide nanoparticles. Reproduced from Ref. [35].

contribution to the broadening have a different θ dependence, it is possible to separate the two effects.

Now taking into consideration also the instrumental breadth (β_{inst}), the observed integral breadth (β_{obs}) becomes: $\beta_{obs} = \beta_{size} + \beta_{strain} + \beta_{inst}$ for Lorentzian and $\beta^2_{obs} = \beta^2_{size} + \beta^2_{strain} + \beta^2_{inst}$ for Gaussian. Therefore, by a substitution of the previous equations, the Williamson and Hall relationship [33] can be plotted with $x = 4\sin\theta$ and $y = \{\beta_{obs} - \beta_{int}\}\cos\theta$, where the crystallite size can be obtained from the y-intercept and the strain from the slope.

Furthermore, an in depth study of the reflection broadening and of the diffuse scattering, which is more prominent for amorphous and locally disordered materials, can give valuable information about about the local structure [34]. This is accomplished through a method called Pair Distribution Function analysis (PDF), which is based on a Fourier transformation of the total scattering intensity including not only the Bragg scattering, but also the diffuse contribution.

Figure 1.6 shows the Bragg scattering of bulk magnetite and a clear difference from the scattering by iron oxide nanoparticles, which presents a large Debye-Scherrer broadening.

The PDF thus gives real space information where the peak position correspond to the bond length as shown in Figure 1.7, *i.e.*, it reflects all pairs of interatomic distances within a material.

To achieve this description, first an analysis of the diffraction pattern has to be carried out taking into consideration the Bragg scattering as well as the diffuse scattering, which is achieved with the total scattering structure function, $S(Q)$:

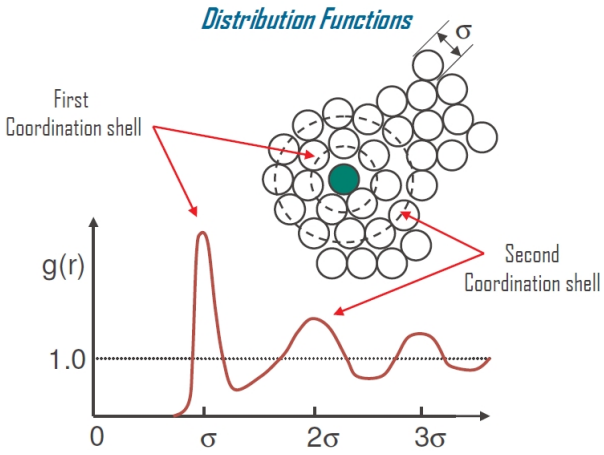

Figure 1.7: First nearest neighbor correlation. Reproduced from Ref. [36].

$$S(Q) = \frac{I^{coh}(Q) - \sum c_i |f_i(Q)|^2}{|\sum c_i f_i(Q)|^2} \tag{1.5}$$

where $I^{coh}(Q)$ is the corrected and normalized coherent scattering intensity; Q is the magnitude of the wave vector; c_i is the atomic concentration and $f_i(Q)$ is the atomic form factor.

The final PDF data is then obtained through a Fourier transform of the $S(Q)$:

$$G(r) = \frac{2}{\pi} \int_0^\infty Q[S(Q) - 1] \sin(Qr) \mathrm{d}Q \tag{1.6}$$

An example of the final PDF data of Ni powder, usually used as calibrant, is shown in Figure 1.8.

Such method is performed in the same experimental configuration as a XRD experiment with only few differences. Since it takes into consideration the diffuse scattering, "clean" high energy radiation is necessary, and it is therefore usually performed at a high energy station of a synchrotron facility. Furthermore, the detector is positioned much closer to the sample in order to obtain the largest possible Q range and consequently get information about the shortest possible distances, r(Å), when doing the Fourier transform.

In this thesis the PDF method was used to evaluate the presence of amorphous SiO_2 impurities in a Si sample, and could be performed due to the difference between the Si-Si and Si-O bond lengths (Figure 1.9). The results are presented in Chapter 2.

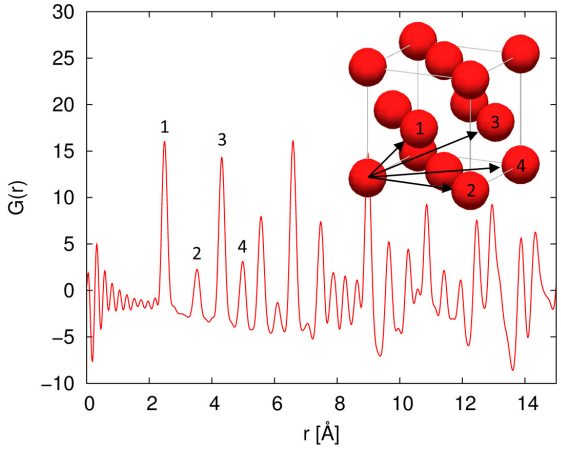

Figure 1.8: PDF obtained for Ni powder. First nearest neighbor correlations are indicated in the *fcc* crystal structure. Reproduced from Ref. [35].

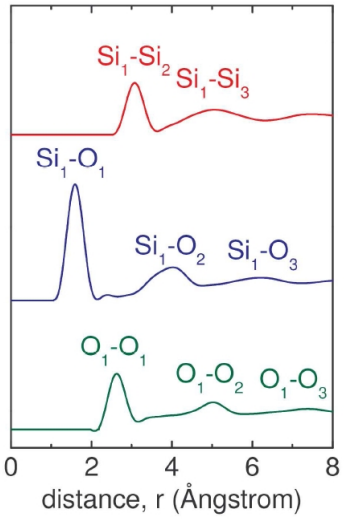

Figure 1.9: Differences on the first neighbor distances on the PDF of Si, SiO_2 and O. Reproduced from Ref. [36].

1.3.2 Lattice Dynamics

On a microscopic level, the lattice thermal conductivity can be understood as the transport of thermal energy through the lattice by considering wave packets of normal modes. In a crystal the normal modes of vibration are quantized as phonons, which provide the thermal transport. Phonons are bosons, *i.e.*, particles or quasiparticles that obey the Bose-Einstein statistics, which determines the statistical distribution of identical bosons over the energy states in thermal equilibrium. Therefore the expected population of phonons (f) in an energy state ($\hbar\omega$) is

$$f(\omega) = \frac{1}{e^{\beta\hbar\omega} - 1} \tag{1.7}$$

where $\beta = 1/k_B T$ and k_B is the Boltzmann's constant.

Lattice vibrations contain energy in the form of kinetic energy of the moving nuclei and elastic energy from the lattice distortion. A sound wave that travels through a crystal therefore transports energy. Lattice thermal conduction in solids can consequently be described as phonon transport.

A solid can be understood in the context of sound waves as a network of masses, m_i, the nuclei, that are connected by elastic springs, K_i, characterizing the interatomic bonds, potentials. In a first approximation, the so-called harmonic approximation, the restoring force between two adjacent atoms is assumed to be proportional to the relative displacement. The solution of the equations of motion of such a system yield the dispersion relation $\omega = \omega(k)$.

The motion of each individual atom is influenced by the position of it's neighbors and for shorter wavelengths, the angular velocity ω of the wave is not a linear function of the wave vector k anymore. A wave vector that is exactly half of the interatomic distance a is an interesting special case to illustrate this. In this case, every second atom has the same displacement. Longer wave vectors are then exactly equivalent to a corresponding shorter wave vector, until a wave vector $k = a$ describes a wave where all atoms have the same displacement, i.e. an infinite wavelength. The dispersion curve is therefore symmetrical around $k = a/2$.

In the simple case that all nuclei have same mass and all elastic constants are equal, the phonon dispersion is given by the Debye approximation: $\omega = v \cdot k$, where v is the phase velocity and $v_g(\omega) = \mathrm{d}\omega/\mathrm{d}k$ is the group velocity. This is known as the acoustic branch of

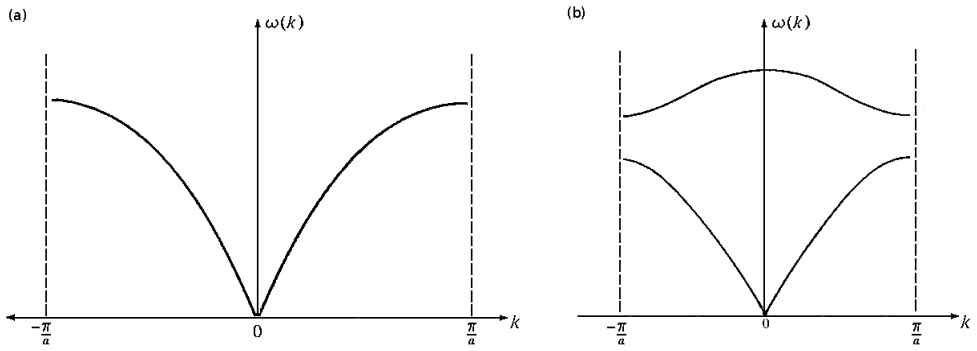

Figure 1.10: Solutions of the equations of motion for a monoatomic (a) and a diatomic chain (b). Modified from Ref. [37]

the dispersion relation. The solution of the equations of motion of such a system is shown in Figure 1.10 (a).

For the case of a diatomic chain, a second solution for the equations of motion is also valid, giving rise to the optical branch which, contrary to the acoustic branch starting from zero and increases with increasing k, starts at a high value of ω and decreases with increasing k (Figure 1.10 (b)).

Complicated vibrational spectra and dispersion relations emerge in particular for complex multiatomic crystal structures [9, 38]. The masses and the bonding environment of the different atoms are decisive for the vibrational properties of different solids.

As an example, Figure 1.11 [39] shows the phonon dispersion curves for Si (diamond structure) and the density of phonon states as a sum of the dispersion curves over all k's. Such a dispersion curve is accessible by momentum resolved inelastic scattering measurements on single crystals.

In this context, regions with locally different elastic properties (interatomic potentials) or atomic masses can act as scattering centers for phonons. Alloying can therefore significantly reduce the thermal conductivity of a material [40, 41]: It becomes opaque for phonons because they are frequently scattered. Materials with a complex unit cell, such as clathrates [6], which are composed by cages filled with rattling atoms, have a low thermal conductivity as well, both because the rattling atoms act as scattering centers for phonons, and because of the large unit cell the relative effective number of heat transport phonons is reduced.

The challenge for the design of thermoelectric materials is to increase the phonon scattering rate or decrease the phonon mean free path without increasing electron scattering at the

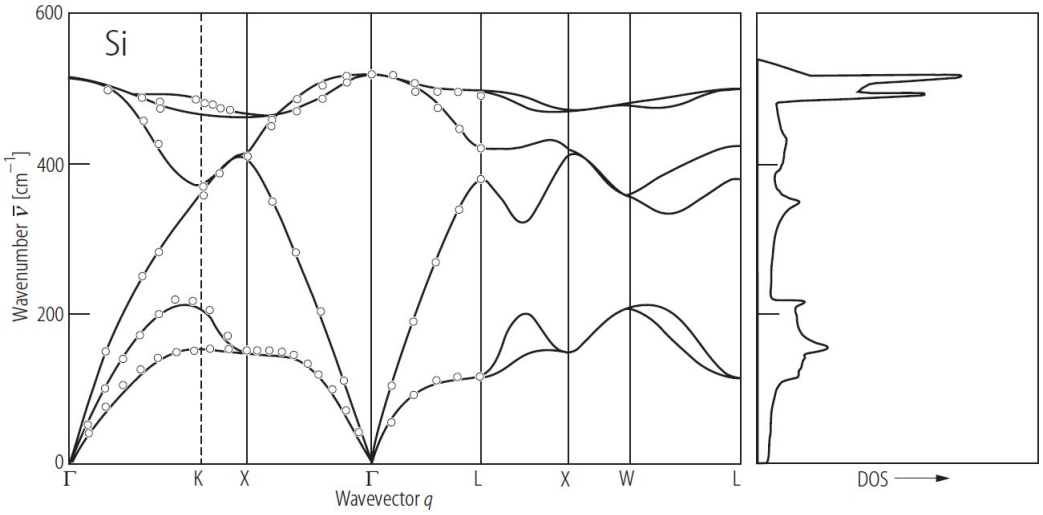

Figure 1.11: Si phonon dispersion curves (left) and density of phonon states (right) with experimental data points and ab-initio calculations. Reproduced from Ref. [39].

same time. An increased electron scattering would lead to a lower electronic conductivity leading to a decrease of the figure of merit (equation 1.2).

Nanostructuration can potentially cause a reduction on the thermal conductivity by altering the phonon dispersion relation leading to a reduction of the heat capacity and the average group velocity, and by increasing phonon scattering due to a large amount of grain boundaries leading to a reduction of the mean-free path [42]. In single crystalline silicon, *e.g.*, 90% of the heat is transported by phonons with mean free path larger than 100 nm [42]. Therefore, an average grain size of around 100 nm or slightly smaller is already effective in lowering the lattice thermal conductivity without affecting significantly the electronic conductivity which has a significantly smaller mean free path, in the order of ~ 10 nm.

The effects of nanostructuration on the lattice dynamics was already investigated with theoretical calculations [43, 44, 45, 46, 47, 48, 49, 50] and experimentally by methods such as inelastic neutron scattering [51, 52, 53, 54, 55, 56], Raman spectroscopy [57, 58], nuclear inelastic scattering (NIS) [55, 59] and measurements of the specific heat [60, 61].

Overall, these calculations and experiments reveals that an enhancement in the density of phonon states (DPS) at low energies and a broadening of the bands on the DPS is expected for nanocrystalline materials. These modifications in the vibrational modes are attributed to the vibrations of atoms located at the grain boundaries where the atomic structure is more open than within the crystalline grains, and result in a modified force field and softening of

the force constants.

Therefore an investigation of the effects of nanostructuration on the lattice dynamics of thermoelectric materials should yield a deeper understanding on the mechanisms behind the reduction of the speed of sound in solids, which results in a reduction in the lattice thermal conductivity.

In this thesis, such a study was carried out by the measurements described in the subsequent sections.

1.3.2.1 Heat Capacity

The internal energy of a solid is typically composed by three energetic contributions: vibrational, electronic and magnetic. We will concentrate on the vibrational energy, *i.e.*, taking into consideration the phonons energies and the number of phonons, the internal energy (E) can be calculated.

The energy of the phonons is linear in their frequency of vibration: $E_{ph} = \hbar\omega$ and the total vibration energy in a solid is therefore the sum of all phonons: $E = \sum n(\omega)\hbar\omega_{ph}$. Since the number of phonons in an energy state, $f(\omega)$, is given by the Bose-Einstein statistics (as mentioned previously), it is possible to apply the concept of the density of phonon states ($g(\omega)$) where $n(\omega) = f(\omega)g(\omega)$, and a normalization is obtained for $g(\omega)$ with $3N$ vibrational modes for a solid comprising N atoms: $\int g(\omega)\mathrm{d}\omega = 3N$. Expressing the sum over all vibrational modes as an integral, the total vibrational energy is:

$$E = \int_0^\infty g(\omega)\frac{\hbar\omega}{e^{\beta\hbar\omega} - 1}\mathrm{d}\omega \tag{1.8}$$

The heat capacity of a solid can be define as the quantity of heat that is required in order to increase its temperature by a unit value, i.e., it is the temperature derivative of its internal energy:

$$C = \left(\frac{\partial E}{\partial T}\right) = k_B \int_0^\infty g(\omega)\frac{(\beta\hbar\omega)^2 e^{\beta\hbar\omega}}{(e^{\beta\hbar\omega} - 1)^2}\mathrm{d}\omega \tag{1.9}$$

Classical approaches to the heat capacity: Theories and calculations around the heat capacity of a solid have been a topic of discussions since 1819, when Petit and Dulong [62] showed that around room temperature the specific heat of monoatomic solids was around 24.9 J/mol-K, i.e., three times the the ideal gas constant (fact which was latter explained by Boltzmann). But in 1875, Weber [63] verified that the heat capacity would go to zero with

decreasing temperatures and that at room temperature the heat capacity for substances such as silicon, boron, carbon and beryllium was much smaller that $3R$.

$$C_v = 3R = 3Nk_B \tag{1.10}$$

In 1907 Einstein [64] proposed the quantization of a simple harmonic oscillator model with energy levels $\left(i + \frac{1}{2}\right) h\nu$, $i = 1, 2, ...$ to obtain the specific heat as a function of temperature. With ν being the characteristic vibration frequency of the solid material:

$$C_v(T) = 3Nk_B \frac{e^{\Theta_E/T} \left(\frac{\Theta_E}{T}\right)^2}{(e^{\Theta_E/T} - 1)^2} \tag{1.11}$$

In this equation, the factor 3 takes into account oscillation in all three directions, $\Theta_E = h\nu/k_B$ is the Einstein temperature, N is the number of atoms in the solid and k_B is Boltzmann's constant. In the limits $T \to 0$, $C_v \to 0$ and $T \gg \Theta_E$, $C_v \to 3R$. But still in the intermediate temperature range, experimental results are significantly above Einstein's prediction.

Einstein's model treats each atom independently and assumes that all atoms vibrate at the same frequency. But in 1912, Max Born and Theodore von Kármán [65] proposed another model taking into account that bonding in a solid prevents independent vibrations. They have proposed a set of boundary conditions to the wave function so that it must be periodic on a certain Bravais lattice.

In the same year, Peter Debye [66] simplified the model assuming the sound velocity to be the same in all crystalline directions and for all frequencies. In this model, the specific heat is therefore:

$$C_v(T) = 9Nk_B \left(T/\Theta_D\right)^3 \int_0^{\Theta_D/T} \frac{e^x x^4}{\left(e^x - 1\right)^2} dx \tag{1.12}$$

$\Theta_D = \hbar\omega_D/k_B$ is the Debye temperature with ω_D being the maximum phonon frequency, and in the limit $T \to 0$, $C_v \to 0$:

$$C_v(T) = \frac{12\pi^4}{5} Nk_B \left(\frac{T}{\Theta_D}\right)^3 \tag{1.13}$$

With the values obtained in this limit for the Debye temperature, the speed of sound can be calculated:

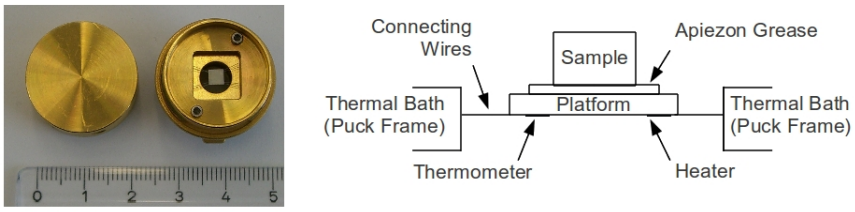

Figure 1.12: Right: heat capacity puck from PPMS-QD. Left: schematics of sample mounting on the HC puck.

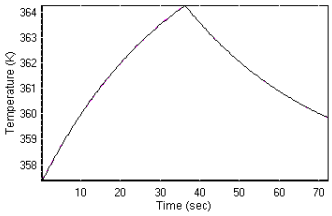

Figure 1.13: Heat pulse obtained during HC measurements with the PPMS-QD.

$$v_s = \frac{k_B \Theta_D}{\hbar (6\pi^2 N_V)^{1/3}} \tag{1.14}$$

where N_V is the number of atoms per unit volume.

During this thesis, measurements of the heat capacity were done between 2 and 400 K in a commercial instrument, the Physical Property Measurement System (PPMS) from Quantum Design using the normal heat capacity option and between 0.1 and 2 K using the dilution option. First a measurement of the addenda would be performed (thermal conducting grease + platform) and then the samples (mass usually around 5 mg with at least one very flat face) were placed on a platform as shown in Figure 1.12.

A hybrid adiabatic relaxation method was used to determine the heat capacity [67]. With this method a heat pulse is applied to the sample and temperature variation, both during and after the heat pulse, is recorded (Figure 1.13). The heat capacity is then calculated by fitting a model within the PPMS software.

1.3.2.2 Elastic Constants: Resonant Ultrasound Spectroscopy (RUS)

Resonant Ultrasound Spectroscopy (RUS) is a nondestructive technique which uses the information revealed by the natural modes of vibration to measure the elastic constant of materials (Figure 1.14).

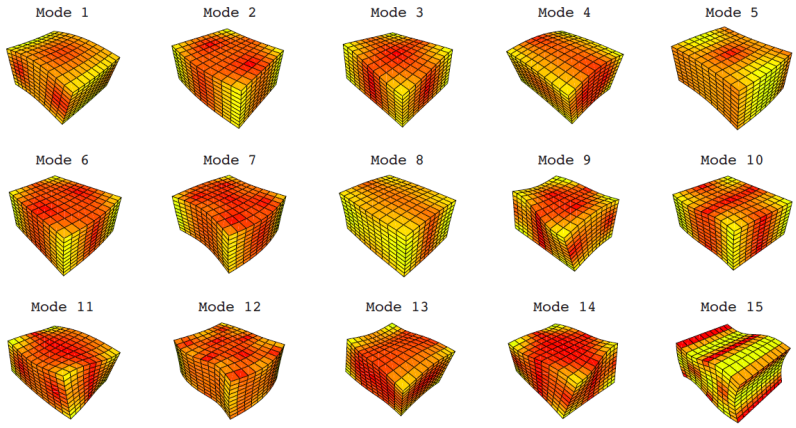

Figure 1.14: Normal modes of vibrations for a parallelepiped. Reproduced from Ref. [68].

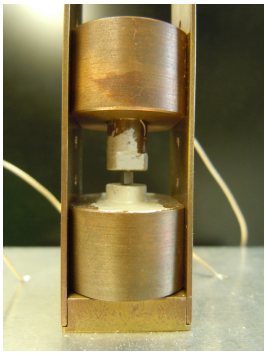

Figure 1.15: RUS apparatus with a Si sample mounted on it.

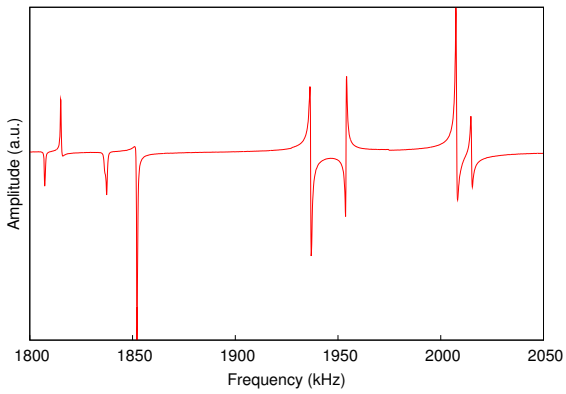

Figure 1.16: Sample RUS data obtained at room temperature for a SiGe sample.

This method employs two piezoelectric transducers: one will excite the sample (usually parallelepipeds carefully polished on all six sides) and the other will detect the resonant response of the sample. Figure 1.15 shows the RUS apparatus which was used, with a Si sample mounted between the two transducers, in order to obtain the resonance spectrum. An example of such a spectrum is shown in Figure 1.16.

The resonance frequencies obtained from the spectrum are used as input data, together with the dimensions and mass of the sample and some initially guessed elastic constants, for a program which calculates the vibrational frequencies using Hooke's law for a 3-D elastic solid:

$$\sigma_{ij} = \sum_{k=1}^{3} c_{ijkl}\epsilon_{kl} \tag{1.15}$$

and Newton's second law:

$$\rho\omega^2\varphi_i + \sum_{jkl} c_{ijkl}\frac{\partial^2\varphi_k}{\partial x_j \partial x_l} = 0 \tag{1.16}$$

where σ_{ij} and ϵ_{kl} are the stress and strain tensors, ρ is the density, ω are the eingenvalues, *i.e.*, the resonant frequencies, φ are the eingenfunctions which can be expanded using a set of basis and c_{ijkl} is the fourth-order elastic tensor, with i, j, k and $l = 1, 2, 3$ correspond to the three spacial dimensions, which applies the concept of a spring constant to a three-dimensional elastic media. Due to symmetry, the elastic tensor can be reduced to a second rank matrix $C_{\alpha\beta}$ using the Voigt convention. In a polycrystalline material with cubic crystal

```
Si198 RT
free moduli are c11, c44,
using 10 order polynomials    mass = 0.0193 g  rho =  2.257 g/cm3

  n    fex      fth    %err wt k i
  1 1.010708 1.004815 -0.58 1.00
  2 1.255874 1.260086  0.34 1.00
  3 1.351322 1.357383  0.45 1.00
  4 1.429758 1.433584  0.27 1.00
  5 1.462615 1.463404  0.05 1.00
  6 1.562136 1.564804  0.17 1.00
  7 1.579866 1.572533 -0.46 1.00
  8 1.605337 1.607122  0.11 1.00
  9 1.608076 1.612584  0.28 1.00
 10 1.647764 1.650994  0.20 1.00
 11 1.748772 1.750052  0.07 1.00
 12 1.757156 1.758032  0.05 1.00
 13 1.807250 1.813769  0.36 1.00
 14 1.829257 1.834239  0.27 1.00
 15 1.897793 1.900283  0.13 1.00
 16 1.937859 1.940555  0.14 1.00
 17 2.023812 2.021560 -0.11 1.00
 18 2.050574 2.043058 -0.37 1.00
 19 2.069421 2.068146 -0.06 1.00
 20 2.144250 2.143753 -0.02 1.00
 21 2.164087 2.170338  0.29 1.00
 22 2.173737 2.176553  0.13 1.00
 23 2.214795 2.199442 -0.69 1.00
 24 2.239055 2.233365 -0.25 1.00
 25 2.243249 2.235924 -0.33 1.00
 26 2.350932 2.352271  0.06 1.00
 27 2.357534 2.362447  0.21 1.00

Bulk modulus = 0.9402 (*** cubic!)
   c11    c22    c33    c23    c13    c12     c44    c55    c66
  1.716  1.716  1.716 0.5521 0.5521 0.5521  0.582  0.582  0.582
  d1     d2     d3
 0.2238 0.1831 0.2087
loop# 7   rms error = 0.2925 %, changed by 0.00938494 %
length of gradient vector = 0.000223794  blamb = 1
```

Figure 1.17: RUS output file of Si198 sample.

structure only two elastic constants are necessary to fully describe the elastic properties of the sample.

Figure 1.17 shows an example of an output file generated by the program [69]. The first column the ascending order of the resonance frequencies obtained experimentally shown in the second column (in MHz), whereas the theoretically calculated frequencies are shown in the third column. The relative error between experimental and theoretical frequencies is given in the forth column and the weighting factor is giving in the fifth column. The calculated bulk modulus, elastic constants (c) and refined dimensions of the samples (d) are shown in the end of the output file as well as the rms error, which should be around or smaller than 0.5% for a good fit, and 0.2% for an excellent fit.

For an isotropic material, only the components C_{11} and C_{44} of the material's elastic tensor are necessary to extract the speed of sound due to symmetry:

$$v_s = \left[\frac{1}{3} \left(\frac{1}{v_{long}} \right)^3 + \frac{2}{3} \left(\frac{1}{v_{trans}} \right)^3 \right]^{-\left(\frac{1}{3}\right)} \tag{1.17}$$

where $v_{long} = \sqrt{C_{11}/\rho}$ accounts for compressive (longitudinal) waves and $v_{trans} = \sqrt{C_{44}/\rho}$ accounts for shear (transverse) waves. C_{11} and C_{44} correspond to the bulk (B) and shear (G) modulus respectively. In an isotropic media, B and G are two independent elastic constants representing extreme types of deformation: B represents the volume change without shape change, *i.e.* resistance to compression; and G represents shape change without volume change, *i.e.* resistance to shear deformation.

In contrast for single crystals, $v_{trans} = \sqrt{G/\rho}$ and $v_{long} = \sqrt{\frac{B+\frac{4}{3}G}{\rho}}$. The average speed of sound is then obtained by considering the bulk modulus $B = \frac{C_{11}+2C_{12}}{3}$ and the shear modulus can be calculated with the Hershey-Kröner-Eshelby averaging method as described by Eshelby [70]:

$$G^3 + \alpha G^2 + \beta G + \gamma = 0 \tag{1.18}$$

where $\alpha = \frac{5C_{11}+4C_{12}}{8}$, $\beta = -\frac{C_{44}(7C_{11}-4C_{12})}{8}$, $\gamma = -\frac{C_{44}(C_{11}-C_{12})(C_{11}+2C_{12})}{8}$.

1.3.2.3 Thermal Conductivity

Thermal conductivity (κ) is an intrinsic property of a material which relates the rate of heat transfer ($\mathrm{d}Q/\mathrm{d}t$) per unit area (A), also known as heat current density ($\mathbf{J}$), to the rate of change in temperature ($-\nabla T$):

$$\mathbf{J} = \frac{\dot{Q}}{A} = -\kappa \nabla T \tag{1.19}$$

In metals the heat is usually transported by freely moving valence electrons. therefore a linear relationship between thermal conductivity (κ) and electrical conductivity (σ) can be quantified with the Wiedemann-Franz Law:

$$\frac{\kappa}{\sigma} = LT \tag{1.20}$$

where L is a proportionality constant called Lorentz number.

This relationship explains how in metals the thermal conductivity increases with raising temperature while the electrical conductivity decreases.

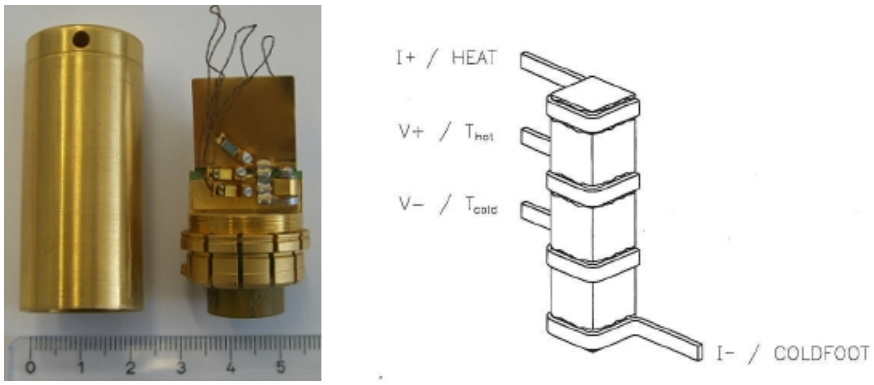

Figure 1.18: Left: thermal transport option puck with Si sample mounted on it. Right: Leads mounted in a four-probe configuration. Reproduced from Ref. [72].

However, for other materials such as semiconductors, heat is mostly transported by phonons. Therefore, as mentioned previously, the thermal conductivity of such materials can be evaluated in two parts: $\kappa = \kappa_{el} + \kappa_{lat}$, where κ_{el} is the electronic contribution and can be estimated using the Wiedemann-Franz Law ($\kappa_{el} = \sigma LT$). Although the value of the Lorentz number shows a few variations depending on temperature and material, it is generally stable for high temperatures. In this work we have performed the calculations with $L = 2.44 \times 10^{-8}\,\mathrm{W\,\Omega\,K^{-2}}$ independently of the temperature.

Lattice thermal conductivity is the transport of thermal energy through the lattice by phonons. Taking into consideration the equations previously mentioned for phonons (section 1.3.2.1), equation 1.19 can be expanded in terms of phonon energy, number of phonons and phonon velocity and combined with equation 1.9 a final lattice thermal conductivity in a simplified Debye model is given by:

$$\kappa_{lat} = \frac{1}{3} C_V < l >< v_s > \tag{1.21}$$

where C_V is the specific heat, $< l >$ is the average phonon mean free path and $< v_s >$ is the average speed of sound. A complete derivation of this equation can be found in ref. [71].

Thermal conductivity, as well as Seebeck coefficient and electronic resistivity measurements, were performed on a commercial Physical Property Measurement System (PPMS) from Quantum Design using a four-probe lead configuration between 2 and 400 K (Figure 1.18).

With this method, the two outer probes are used to apply a current through the sample and the two inner probes are used to measure the voltage / temperatures. The data obtained

is then combined with accurate measurements of sample dimensions (cross section area and distance between wires) to extract the thermoelectric values. This method is mainly used for bulk samples.

1.3.2.4 Inelastic Neutron Scattering (INS)

Neutrons are an important probe to investigate condensed matter due to its basic properties: the de Broglie wavelength which is derived from its mass value is of the order of interatomic distances; it is not charged and therefore interacts only with the nuclei and not electronic charges; has magnetic moment and can interact with unpaired electrons in magnetic atoms; and the energy of thermal neutrons is of the same order as many excitations in condensed matter.

The last characteristic of magnitude is the one of most interesting in this work since neutrons can be inelastic scattered by creation or annihilation of phonons (excitations) and can therefore provide important information about the lattice dynamics of a material.

Neutrons can be scattered by the sample coherently with determined phase relations for all scatterers, leading to interference effects and ultimately to Bragg peaks, or incoherently from the random distribution of isotopes and different spin of the nuclei, which yields information about single particle behavior. Both Si and Ge are highly coherent scatterers with coherent neutron cross sections of 2.1633(10) and 8.42(4) barn, respectively.

Elastic scattering occurs when the wave vector **k**, which describes the wave incident on the sample and the wave incident on the detector **k'** are equal ($|\mathbf{k}| = |\mathbf{k}'| = \frac{2\pi}{\lambda}$), and the scattering vector ($\mathbf{Q}$) is given by the difference $\mathbf{Q} = \mathbf{k} - \mathbf{k}'$, *i.e.*, $|\mathbf{Q}| = \sqrt{k^2 + k'^2 - 2kk'\cos 2\theta}$.

In contrast, inelastic occurs when the neutron loses or gain energy during the scattering process, *i.e.*, $|\mathbf{k}| \neq |\mathbf{k}'|$ and the modulus of the scattering vector becomes significantly more complicated since it energy transfer should also be consider. Figure 1.19 illustrates this process in a simple form.

In a Time of Flight (TOF) inelastic neutron spectrometer raw data is acquired in the form of intensity ($I(2\theta, t)$) as a function of angle 2Θ and time t and a set of equations are needed to transform it to $(\mathbf{Q}, \omega)$-space. The resulting intensity as a function of $S(\mathbf{Q}, \omega)$ can be calculated from the probability density of a neutron being scattered into a solid angle $d\omega$ with an energy transfer dE' given by the double differential cross-section:

$$\frac{d^2\sigma}{d\omega dE'} = N\frac{k}{k'}b^2 S(\mathbf{Q}, \omega) \tag{1.22}$$

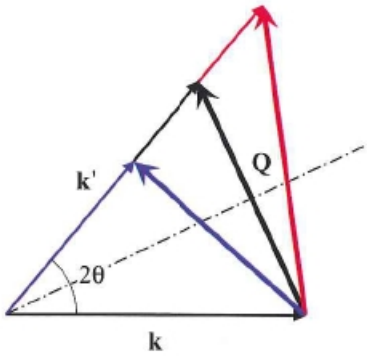

Figure 1.19: Scattering vector **Q** depending on incident and final wave vector **k** and **k'**: black corresponds to elastic scattering, blue and red corresponds to inelastic scattering with loss or gain of energy. Reproduced from Ref. [73].

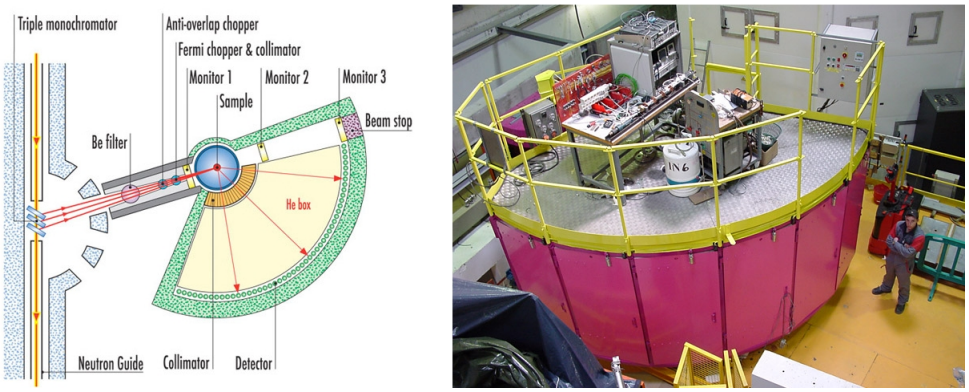

Figure 1.20: Time of Flight (TOF) spectrometer IN6-ILL (Grenoble, France)

And the relation between time and energy is

$$E(t) = \frac{m_n}{2} L^2 \frac{t^2 - t_0^2}{t^2 t_0^2} \tag{1.23}$$

where m_n is the mass of the neutron, L is the sample-detector distance and t and t_0 are the times when the inelastically and elastically scattered neutrons reach the detector, respectively.

A complete derivations of the above equations can be found in Ref. [74].

Inelastic neutron scattering experiments were performed on the Time of Flight (TOF) spectrometer IN6 at the cold source of the high-flux reactor at the Institute Laue-Langevin (Grenoble, France), shown in Figure 1.20. The neutron beam is directed to a triple monochromator and are diffracted to a Fermi chopper where the neutrons flight path starts. It then

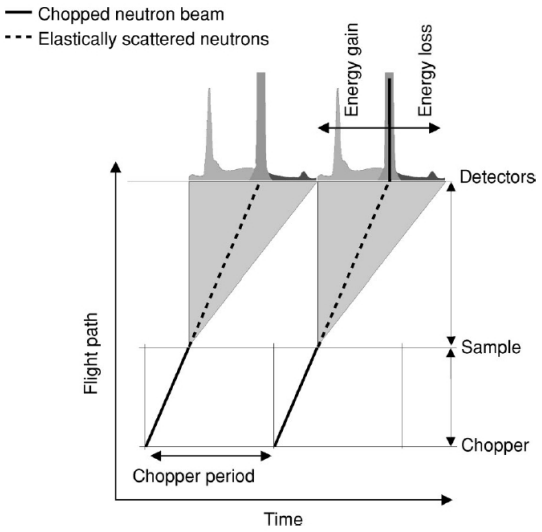

Figure 1.21: TOF experiment: the monochromated neutron beam is periodically chopped and, after a certain flight path, it reaches the sample where it will be scattered either elastically (dotted line) or inelastically by lost or gain of energy arriving before or after the elastically scattered neutrons. Reproduced from Ref. [71].

hits the sample and is scattered towards the detectors placed in a large Q range. If the neutrons gains or loses energy due to phonon annihilation or creation, it will reach the detectors before or after the elastically scattered neutrons (Figure 1.21). The density of phonon states is then calculated from the resulting spectrum summed over all Q range.

1.3.2.5 Nuclear Inelastic Scattering (NIS)

Nuclear inelastic scattering is a method which gives access to the element specific density of phonon states [75] of elements with specific Mössbauer energies. Since it has a resonance character, it yields high count rates and therefore can be performed with a small size of synchrotron radiation beam and in tiny samples such as thin films, nanoparticles and biological samples. It can also be used in any type of sample, including amorphous, disordered, polycrystalline and single crystalline.

In this method, a high brightness pulsed synchrotron radiation is necessary in order to excite the nuclei, which may then decay. This excitation is possible not only elastically, when the radiation energy is equal to the Mössbauer energy, but also inelastically through the creation or annihilation of phonons. The phonon assisted nuclear resonant absorption cross-section is thus measured. The nucleus then decays through emission of γ-fluorescence

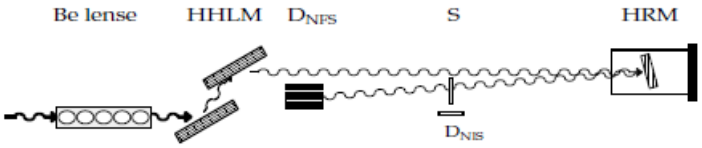

Figure 1.22: Experimental setup for NIS: Be lenses, double-crystal Si(111) high-heat-load monochromator (HHLM), temperature-controlled sapphire single crystal used as a high-resolution monochromator (HRM), sample (S), and Si APD X-ray detectors (D_{NIS} and D_{NFS}).

or X-rays, via internal conversion, and these decay products are counted as function of the incoming energy.

The experimental setup in Figure 1.22 shows an schematic of how the measurement at the nuclear resonance station [75] ID22N of the European Synchrotron Radiation Facility in Grenoble, France. The beam is collimated by a Be compound refractive lens and filtered by a double-crystal Si (111) high-heat-load monochromator. It then reaches a temperature-controlled high-resolution monochromator composed of a sapphire crystal inside a nitrogen gas flow cryostat mounted on a 2-circle goniometer and is backscattered towards the sample.

The sample is usually cooled down to approximately 20 K inside a vacuum chamber with Kapton windows for the incoming and scattered beams. The temperature of the sample is monitored by a temperature sensor in the vicinity of the sample, but the precise temperature is better determined through the Bose-Einstein statistics, comparing the signal on the Stokes and anti-Stokes sides as the phonon populations are different, and the temperature can be estimated from this difference, according to the Bose factor.

Avalanche photodiode X-ray detectors are placed in the beam after the sample to detect the nuclear forward scattering (D_{NFS}) and transverse near the sample to detect the inelastic nuclear scattering (D_{NIS}). Energy scans are performed by varying the monochromator temperature.

Several measurements are done on each sample for better statistics. The NIS spectra are then summed and the corresponding partial density of phonon states for are derived using a modification of the program DOS [76] taking into account the instrumental resolution by convoluting with a Gaussian function with the same FWHM as the measured instrumental function.

References

[1] International Energy Agency. *World Energy Outlook 2012*. Organization for Economic, 2012. 2

[2] Lon E. Bell. **Cooling, Heating, Generating Power, and Recovering Waste Heat with Thermoelectric Systems**. *Science*, **321**[5895]:1457–1461, 2008. 2, 3

[3] M. S. Dresselhaus, G. Chen, M. Y. Tang, R. G. Yang, H. Lee, D. Z. Wang, Z. F. Ren, J. P. Fleurial, and P. Gogna. **New Directions for Low-Dimensional Thermoelectric Materials**. *Adv. Mater.*, **19**[8]:1043–1053, 2007. 4, 6

[4] X. W. Wang, H. Lee, Y. C. Lan, G. H. Zhu, G. Joshi, D. Z. Wang, J. Yang, A. J. Muto, M. Y. Tang, J. Klatsky, S. Song, M. S. Dresselhaus, G. Chen, and Z. F. Ren. **Enhanced thermoelectric figure of merit in nanostructured n-type silicon germanium bulk alloy**. *Appl. Phys. Lett.*, **93**[19]:193121–3, November 2008. 4, 6

[5] B. Poudel, Q. Hao, Y. Ma, Y. Lan, A. Minnich, B. Yu, X. Yan, D. Wang, A. Muto, D. Vashaee, X. Chen, J. Liu, M. S. Dresselhaus, G. Chen, and Z. Ren. **High-Thermoelectric Performance of Nanostructured Bismuth Antimony Telluride Bulk Alloys**. *Science*, **320**[5876]:634–638, 2008. 4

[6] G. S. Nolas, G. A. Slack, and S. B. Schujman. % bf Chapter 6 Semiconductor clathrates: A phonon glass electron crystal material with potential for thermoelectric applications. In Terry M. Tritt, editor, *Recent Trends in Thermoelectric Materials Research I*, **69**, pages 255–300. Elsevier, 2001. 4, 15

[7] G. J. Snyder, M. Christensen, E. Nishibori, T. Caillat, and B. B. Iversen. **Disordered zinc in Zn_4Sb_3 with phonon-glass and electron-crystal thermoelectric properties**. *Nat. Mater.*, **3**[7]:458–463, July 2004. 4, 7

[8] G. Min and D.M. Rowe. **A serious limitation to the phonon glass electron crystal (PGEC) approach to improved thermoelectric materials**. *J. Mater. Sci. Lett.*, **18**[16]:1305–1306, 1999. 4

[9] G. J. Snyder and E. S. Toberer. **Complex thermoelectric materials**. *Nat. Mater.*, **7**[2]:105–114, February 2008. 4, 15

[10] **http://chemgroups.northwestern.edu/kanatzidis/greatthermo.html**. 4, 5

[11] C. J. Glassbrenner and G. A. Slack. **Thermal Conductivity of Silicon and Germanium from 3K to the Melting Point**. *Phys. Rev.*, **134**[4A]:A1058–A1069, May 1964. 6

[12] G. H. Zhu, H. Lee, Y. C. Lan, X. W. Wang, G. Joshi, D. Z. Wang, J. Yang, D. Vashaee, H. Guilbert, A. Pillitteri, M. S. Dresselhaus, G. Chen, and Z. F. Ren. **Increased Phonon Scattering by Nanograins and Point Defects in Nanostructured Silicon with a Low Concentration of Germanium**. *Phys. Rev. Lett.*, **102**[19]:196803, May 2009. 6

[13] A. I. Hochbaum, R. Chen, R. D. Delgado, W. Liang, E. C. Garnett, M. Najarian, A. Majumdar, and P. Yang. **Enhanced thermoelectric performance of rough silicon nanowires**. *Nature*, **451**[7175]:163–167, 2008. 6

[14] A. I. Boukai, Y. Bunimovich, J. Tahir-Kheli, J.-K. Yu, W. A. Goddard III, and J. R. Heath. **Silicon nanowires as efficient thermoelectric materials**. *Nature*, **451**[7175]:168–171, 2008. 6

[15] J. P. Dismukes, L. Ekstrom, E. F. Stigmeier, I. Kudman, and D. S. Beers. **Thermal and electrical properties of heavily doped Ge-Si alloys up to 1300 K**. *J. Appl. Phys.*, **35**[10]:2899–2907, 1964. 6

[16] A. Hrubý, J. Beránková, and V. Mísková. **Growth of ZnSb Single Crystals**. *Phys. Stat. Sol.*, **3**:289, 1963. 7

[17] S. Bhattacharya, R. P. Hermann, V. Keppens, T. M. Tritt, and G. J. Snyder. **Effect of disorder on the thermal transport and elastic properties in thermoelectric Zn_4Sb_3**. *Phys. Rev. B*, **74**[13]:134108–, October 2006. 7

[18] T. Caillat, J.-P. Fleurial, and A. Borshchevsky. % bf Preparation and thermoelectric properties of semiconducting Zn_4Sb_3. *J. Phys. Chem. Solids*, **58**[7]:1119–1125, July 1997. 7

[19] C. S. Birkel, E. Mugnaioli, T. Gorelik, U. Kolb, M. Panthöfer, and W. Tremel. **Solution Synthesis of a New Thermoelectric $Zn_{1+x}Sb$ Nanophase and Its Structure Determination Using Automated Electron Diffraction Tomography**. *J. Am. Chem. Soc.*, **132**[28]:9881–9889, June 2010. 7

[20] B. Predel. **Fe-Sb (Iron-Antimony)**. In *Landolt-Börnstein - Group IV Physical Chemistry*, **5e**, pages –. 7, 8

[21] A. Bentien, S. Johnsen, G. K. H. Madsen, B. B. Iversen, and F. Steglich. **Colossal Seebeck coefficient in strongly correlated semiconductor $FeSb_2$**. *EPL (Europhysics Letters)*, **80**[1]:17008, 2007. 7

[22] M. S. Diakhate, R. P. Hermann, A. Möchel, I. Sergueev, M. Søndergaard, M. Christensen, and M. J. Verstraete. **Thermodynamic, thermoelectric, and magnetic properties of $FeSb_2$: A combined first-principles and experimental study**. *Phys. Rev. B*, **84**[12]:125210, September 2011. 8

[23] B. Predel. **Ni-Sb (Nickel-Antimony)**. In *Landolt-Börnstein - Group IV Physical Chemistry*, **5I**, pages –. 8, 9

[24] J. Xie, X.B. Zhao, G.S. Cao, M.J. Zhao, Y.D. Zhong, and L.Z. Deng. % bf Electrochemical lithiation and delithiation of $FeSb_2$ anodes for lithium-ion batteries. *Mater. Lett.*, **57**[30]:4673–4677, 2003. 8

[25] J. Xie, X.B. Zhao, H.M. Yu, H. Qi, G.S. Cao, and J.P. Tu. % bf Low temperature solvothermal synthesis of nanosized NiSb as a Li-ion battery anode material. *J. Alloys Compd.*, **441**[1-2]:231–235, 2007. 8

[26] J. C. Bailer, H. J. Emelius, R. Nyholm, and A. F. Trotman-Dickenson. *Comprehensive in Organic Chemistry*, **2**. Pergamon Press: Oxford, UK, 1973. 8

[27] C. S. Birkel, Gr. Kieslich, D. Bessas, T. Claudio, R. Branscheid, U. Kolb, M. Panthöfer, R. P. Hermann, and W. Tremel. **Wet Chemical Synthesis and a Combined X-ray and Mössbauer Study of the Formation of $FeSb_2$ Nanoparticles**. *Inorg. Chem.*, **50**[22]:11807–11812, October 2011. 8

[28] G. Kieslich, C. S. Birkel, A. Stewart, U. Kolb, and W. Tremel. **Solution Synthesis of Nanoparticular Binary Transition Metal Antimonides**. *ChemInform*, **42**[39], 2011. 8

[29] L. Canella, P. Kudějová, R. Schulze, A. Türler, and J. Jolie. % bf Characterisation and optimisation of the new Prompt Gamma-ray Activation Analysis (PGAA) facility at FRM II. *Nucl. Instrum. Methods Phys. Res., Sect. A*, **636**[1]:108 – 113, 2011. 9

[30] R. A. Young. *The Rietveld Method*. Oxford University Press, USA, 1995. 10

[31] A. L. Patterson. **The Scherrer Formula for X-Ray Particle Size Determination**. *Phys. Rev.*, **56**[10]:978–982, November 1939. 10

[32] A. R. Stokes and A. J. C. Wilson. **The diffraction of X-rays by distorted crystal aggregates - I**. *Proc. Phys. Soc.*, **56**[3]:174, 1944. 10

[33] G. K. Williamson and W. H. Hall. **X-ray line broadening from filed aluminium and wolfram**. *Acta Metall.*, **1**[1]:22 – 31, 1953. 11

[34] T. Egami and S. J. L. Billinge. *Underneath the bragg peaks : structural analysis of complex materials*. Amsterdam : Pergamon, 2003. 11

[35] S. Disch. *43rd IFF Springschool 2012 - Scattering Methods for Condensed Matter Research: Towards Novel Applications at Future Sources - Lecture Notes*, chapter D05 - Atomic Pair Distribution Function: Local Structure Investigations, pages D5.1–D5.14. Forschungszentrum Jülich GmbH, 2012. 11, 13

[36] C. Benmore. **ORNL NXS2009 - Lecture Notes**. online, 2009. 12, 13

[37] Ashcroft and Mermin. *Solid State Physics*. Thomson Learning, Inc., 1976. 15

[38] A. Möchel, I. Sergueev, H.-C. Wille, J. Voigt, M. Prager, M. B. Stone, B. C. Sales, Z. Guguchia, A. Shengelaya, V. Keppens, and R. P. Hermann. **Lattice dynamics and anomalous softening in the $YbFe_4Sb_{12}$ skutterudite**. *Phys. Rev. B*, **84**[18]:184306, November 2011. 15

[39] O. Madelung, U. Rössler, and M. Schulz, editors. *Landolt-Börnstein - Group III Condensed Matter*, **41A1a**, chapter Silicon (Si) phonon dispersion relations. SpringerMaterials - The Landolt-Börnstein Database, 2011. 15, 16

[40] G. S. Nolas, J. Poon, and M. Kanatzidis. **Recent Developments in Bulk Thermoelectric Materials**. *MRS Bulletin*, **31**[03]:199–205, 2006. 15

[41] J. Garg, N. Bonini, B. Kozinsky, and N. Marzari. **Role of Disorder and Anharmonicity in the Thermal Conductivity of Silicon-Germanium Alloys: A First-principles Study**. *Phys. Rev. Lett.*, **106**[4]:045901–, January 2011. 15

[42] C. Dames and G. Chen. *Thermoelectrics Handbook: Macro to Nano*, **1**, chapter 42, pages 42–10–42–16. CRC/Taylor & Francis, Boca Raton, FL, 2006. 16

[43] D. Wolf, J. Wang, S.R. Phillpot, and H. Gleiter. **On the thermodynamic relationship between nanocrystalline materials and glasses**. *Phys. Lett. A*, **205**[4]:274–280, September 1995. 16

[44] S.R. Phillpot, J. Wang, D. Wolf, and H. Gleiter. **Computer simulation of the structure and dynamical properties of grain boundaries in a nanocrystalline model material**. In *Materials Science & Engineering A (Structural Materials: Properties, Microstructure and Processing)*, **A204**, pages 76–82, Div. of Mater. Sci., Argonne Nat. Lab., IL, USA, December 1995. Elsevier Office of Naval Res. Office of Naval Res. 16

[45] M.-S. Jeng, R. Yang, D. Song, and G. Chen. **Modeling the Thermal Conductivity and Phonon Transport in Nanoparticle Composites Using Monte Carlo Simulation**. *J. Heat Transfer*, **130**[4], April 2008. 16

[46] R. Singh and S. Prakash. **Vibrational properties of nanocrystalline fcc Ni_3Fe**. *Indian J. Phys.*, **77A**[3]:243–246, May 2003. 16

[47] R. Singh, S. Prakash, R. Meyer, and P. Entel. **Phonon density of states in nanocrystalline ^{57}Fe**. *Pramana J. Phys.*, **60**[3]:547–556, March 2003. 16

[48] A. I. Potapov, I. S. Pavlov, and S. A. Lisina. **Acoustic identification of nanocrystalline media**. *J. Sound Vib.*, **322**[3]:564–580, May 2009. 16

[49] J. Wang, D. Wolf, S. R. Phillpot, and H. Gleiter. **Phonon-induced anomalous specific heat of a model nanocrystal by computer simulation**. In *Nanostruct. Mater.*, **6**, pages 747–750, Div. of Mater. Sci., Argonne Nat. Lab., IL, USA, January 1995. 16

[50] S. Stankov, M. Miglierini, A. I. Chumakov, I. Sergueev, Y. Z. Yue, B. Sepiol, P. Svec, L. Hu, and R. Rüffer. **Vibrational thermodynamics of $Fe_{90}Zr_7B_3$ nanocrystalline alloy from nuclear inelastic scattering**. *Phys. Rev. B*, **82**[14]:144301–, October 2010. 16

[51] B. Fultz, C. C. Ahn, E. E. Alp, W. Sturhahn, and T. S. Toellner. **Phonons in Nanocrystalline ^{57}Fe**. *Phys. Rev. Lett.*, **79**[5]:937–940, August 1997. 16

[52] H. Frase, B. Fultz, and J. L. Robertson. **Phonons in nanocrystalline** Ni_3Fe. *Phys. Rev. B*, **57**[2]:898–905, Jan 1998. 16

[53] S. Mentese, J.-B. Suck, and A. J. Dianoux. **Atomic dynamics of amorphous and nanocrystalline $Ni_{80}P_{20}$**. In *Mater. Sci. Forum*, pages 671–676, Inst. fur Phys., Tech. Univ. Chemnitz, Germany, January 2000. Trans Tech Publications. 16

[54] S. Mentese, J.-B. Suck, and S. Janssen. **Atomic dynamics of rapidly quenched and annealed nanocrystalline $Ni_{89}Hf_{11}$**. In *Physica B*, **316-317**, pages 438–440, Inst. of Phys., Mater. Res. & Liquids, Technische Univ. Chemnitz, Germany, May 2002. Elsevier Nat. Sci. Found. 16

[55] A. I. Chumakov, A. Bosak, and R. Rüffer. **Contribution of acoustic modes to the density of vibrational states measured by inelastic scattering techniques**. *Phys. Rev. B*, **80**[9]:094303–, September 2009. 16

[56] L. Saviot, C. H. Netting, D. B. Murray, S. Rols, A. Mermet, A.-L. Papa, C. Pighini, D. Aymes, and N. Millot. **Inelastic neutron scattering due to acoustic vibrations confined in nanoparticles: Theory and experiment**. *Phys. Rev. B*, **78**[24]:245426–, December 2008. 16

[57] D. Bersani, P. P. Lottici, and X. Z. Ding. **Phonon confinement effects in the Raman scattering by TiO_2 nanocrystals**. *Appl. Phys. Lett.*, **72**[1]:73–75, January 1998. 16

[58] M. Maczka, M. Ptak, M. Kurnatowska, L. Kępiński, P. Tomaszewski, and J. Hanuza. % bf Phonon properties of nanosized $MnWO_4$ with different size and morphology. *J. Solid State Chem.*, **184**[9]:2446–2457, 2011. 16

[59] S. Stankov, Y. Z. Yue, M. Miglierini, B. Sepiol, I. Sergueev, A. I. Chumakov, L. Hu, P. Svec, and R. Rüffer. **Vibrational Properties of Nanograins and Interfaces in Nanocrystalline Materials**. *Phys. Rev. Lett.*, **100**[23]:235503–, June 2008. 16

[60] B. Haiyang, L. Jianlin, J. Duo, and S. Jirong. **Anomalous specific heat behavior of nanocrystalline Fe at low temperatures**. *Chinese Phys. Lett.*, **12**[9]:549–552, January 1995. OK. 16

[61] L. Wang, Z. Tan, S. Meng, A. Druzhinina, R. A. Varushchenko, and G. Li. % bf Heat capacity enhancement and thermodynamic properties of nanostructured amorphous SiO_2. *J. Non-Cryst. Solids*, **296**[12]:139–142, December 2001. 16

[62] A. T. Petit and P. L. Dulong. **Recherches sur quelques points importants de la Théorie de la Chaleur**. *Annales de Chimie et de Physique*, **10**:395–413, 1819. 17

[63] H. F. Weber. **Die specifischen Wärmen der Elemente Kohlenstoff, Bor und Silicium**. *Annalen der Physik*, **230**[3]:367–423, 1875. 17

[64] A. Einstein. **Berichtigung zu meiner Arbeit: "Die Plancksche Theorie der Strahlung etc."**. *Annalen der Physik*, **327**[4]:800, 1907. 18

[65] M. Born and T. von Karman. **On fluctuations in spatial grids**. *Physikalische Zeitschrift*, **13**:297–309, 1912. 18

[66] P. Debye. **Zur Theorie der spezifischen Wärmen**. *Annalen der Physik*, **344**[14]:789–839, 1912. 18

[67] LOT-Oriel. *Advanced heat capacity with helium-3 for PPMS*. Quantum Design, 2012. application note. 19

[68] J. R. Gladden, G. Li, R. Adebisi, S. Firdosy, T. Caillat, and V. Ravi. **High-temperature elastic moduli of bulk nanostructured n- and p-type silicon germanium**. *Phys. Rev. B*, **82**[4]:045209–, July 2010. 20

[69] A. Migliori and J. L. Sarrao. *Resonant Ultrasound Spectroscopy: Applications to Physics, Materials Measurements, and Nondestructive Evaluation*. Wiley-Interscience, 1 edition, 1997. 22

[70] J. D. Eshelby. *Progress in Solid Mechanics*, **2**, page 130. North Holland Publ. Co., Amsterdam, 1961. 23

[71] R. P. Hermann, F. Grandjean, and G. J. Long. **Einstein oscillators that impede thermal transport**. *Am. J. Phys.*, **73**[2]:110–118, February 2005. 24, 27

[72] *Physical Property Measurement System (PPMS) - Manual, Quantum Design*. 24

[73] R. Zorn. *Laboratory Course: Neutron Scattering (Lectures)*, **27**, chapter 11 - Inelastic Neutron Scattering, pages 11.01 – 11.27. Forschungszentrum Jülich GmbH, 2010. 26

[74] G. L. Squires. *Introduction to the theory of THERMAL NEUTRON SCATTERING*. Cambridge University Press, 1978. 26

[75] R. Rüffer and A. I. Chumakov. **Nuclear inelastic scattering**. *Hyperfine Interact.*, **128**:255–272, 2000. 10.1023/A:1012643918108. 27, 28

[76] V.G. Kohn and A.I. Chumakov. **DOS: Evaluation of phonon density of states from nuclear resonant inelastic absorption**. *Hyperfine Interact.*, **125**:205–221, 2000. 28

Chapter 2

Effects of Impurities on the Lattice Dynamics of Nanocrystalline Silicon for Thermoelectric Application

Effects of Impurities on the Lattice Dynamics of Nanocrystalline Silicon for Thermoelectric Application

Tania Claudio[1,2], Gabi Schierning[3], Ralf Theissmann[3], Hartmut Wiggers[3], Helmut Schober[4], Michael Marek Koza[4], Raphaël P. Hermann[1,2]

[1] *Jülich Centre for Neutron Science JCNS and Peter Grünberg Institut PGI, JARA-FIT, Forschungszentrum Jülich GmbH, D-52425 Jülich, Germany*

[2] *Faculté des Sciences, Université de Liège, B-4000 Liège, Belgium*

[3] *Faculty of Engineering and Center for NanoIntegration Duisburg-Essen (CeNIDE), University of Duisburg-Essen, D-47057, Duisburg, Germany*

[4] *Institut Laue Langevin, 6 rue Jules Horowitz B.P. 156, F-38042 Grenoble, France*

Abstract

Doped silicon nanoparticles were exposed to air and sintered to form nanocrystalline silicon. The composition, microstructure and structural defects, were investigated with TEM, XRD and PDF and the lattice dynamics was evaluated with measurements of the heat capacity, of the elastic constants with resonant ultrasound spectroscopy and of the density of phonon states with inelastic neutron scattering. The results were combined and reveal that the samples contain a large amount of silicon dioxide and exhibit properties that deviate from bulk silicon. Both in the reduced density of phonon states and in the heat capacity a Boson peak at low energies, characteristic of amorphous SiO_2, is observed. The thermal conductivity is strongly reduced due to nanostructuration and the incorporation of impurities.

Keywords: Lattice Dynamics, Silicon, Nanocrystalline Material, Density of Phonon States, Heat Capacity and Thermoelectric

PACS numbers: 63.22.m, 81.07.Wx, 29.30.Kve

2.1 Introduction

With increasing availability of tailored nanopowders and nanostructures, densified assemblies of engineered nanostructures are focussed upon for many possible applications, as for instance thermoelectricity. Thermoelectric devices provide cooling when an applied current pumps heat from the cold side towards the hot side through the Peltier effect, or enable waste heat recovery by converting a heat gradient to electrical power through the Seebeck effect. A good thermoelectric material should possess a large Seebeck coefficient, S, a high electrical conductivity σ, and low thermal conductivity κ in order to maximize the dimensionless figure of merit $ZT = S^2\sigma T/\kappa$ for the thermoelectric performance of a material [1, 2, 3]. Reducing the thermal conductivity is therefore a natural way to improve the performance of a thermoelectric material.

Silicon-based materials combine several desirable properties for thermoelectric applications: most are non-toxic in contrast to many other thermoelectric materials and the raw material is relatively inexpensive and available in industrial quantities. Alloys of Si-Ge have a competitive figure of merit at high temperatures [1, 2, 4]; and silicon nanowires with a rough surface present a drastic reduction in thermal conductivity resulting in a $ZT \approx 0.6$ to 1 at room temperature [5, 6]. Furthermore, the properties and technology around silicon are well established in the semiconductor industry, making it an ideal thermoelectric model material for which reference data from single crystals can be used as comparison.

Due to its exceptionally large thermal conductivity, 156 W/m-K [7] at room temperature, predominantly lattice thermal conductivity, silicon is the perfect model material to test the improvement of thermoelectric properties through nanostructuration, when the thermal conductivity is decreased due to the creation of scattering centres for phonons. This concept was already successfully applied to a number of thermoelectric materials [3, 4, 8, 9]. Nanocrystalline silicon was demonstrated to be a competitive thermoelectric material with best $ZT = 0.7$ at 1275 K [8]. Furthermore, the addition of impurities and/or defects was shown to result in a favorable decrease of the lattice thermal conductivity of silicon. Gibbons *et al.* [10] used first-principle methods to calculate the thermal conductivity of nanostructured Si which contained defects and/or impurities and concluded that there exist narrow ranges of impurity parameters (mass, bond strength, etc.) for which a reduction in the thermal conductivity was predicted. Such a decrease was previously observed [11] on bulk silicon as a function of carrier concentration. A 5% substitution of Ge on nanostructured Si

proved to efficiently scatter phonons with a wavelength shorter than 1 nm [4], resulting in a further reduction of the thermal conductivity.

Previous work by Schierning *et al.* [12] demonstrated that nanoparticles of Si produced by a gas phase synthesis and exposed to air before sintering, present a certain amount of impurities in the form of amorphous SiO_2.

Here, we report on the role of such impurities on the lattice dynamics of nanocrystalline Si produced by a bottom-up process with respect to thermoelectric applications.

2.2 Experimental

Silicon nanoparticles were synthesized by a plasma-assisted gas phase process, using a microwave reactor [13]. By variation of microwave power, chamber pressure, and concentration of the precursor gas silane (SiH_4) as well as the plasma gases Ar and H_2, almost spherically shaped particles were obtained. The conditions used were a precursor concentration of 100-200 vpm, pressures of 20-100 mbar, and microwave powers of 1200-2000 W. Two different batches of crystalline particles of predefined dimension (22 and 30 nm) in a narrow size distribution were obtained by controlling these parameters. N-type doping was achieved by adding phosphine (PH_3) to the precursor gas. The incorporation of electrically active phosphorus into the nanoparticles was demonstrated for similar batches of silicon nanoparticles by Electron Paramagnetic Resonance (EPR) earlier [14].

The compaction of the nanoparticles was done with a spark plasma sintering furnace from FCT Systeme GmbH. Several grams of the nanoparticles of the two different batches were pre-compacted and subsequently sintered to dense pellets with a diameter of 2 cm in a mbar Ar atmosphere. Heating and cooling rates were fixed to 100 K/min. The sintering temperature was 1050°C with a hold time of 3 minutes. A pressure of 35 MPa was applied during sintering. No special care was taken to prevent samples from contamination with oxygen.

Structural characterization of raw powder and sintered pellets was done by Transmission Electron Microscopy (TEM) with a 200 keV Philips, Tecnai F20 ST microscope. Sintered pellets were cut into pieces, mechanically thinned and subsequently polished by a precision ion polishing system with Ar-ions.

The average crystallite size of the nanoparticles and the nanocrystalline pellets was obtained by X-Ray Diffraction (XRD) and a subsequent Rietveld refinement based on the

measured data and taking into consideration the Debye Scherrer broadening of the diffraction peaks. For the X-ray diffraction, pieces of the sintered pellets were thoroughly ground to ensure good powder statistics and the powder was filled into glass capillaries. A Siemens D5000 powder diffraction machine was used in transmission geometry, equipped with a Germanium monochromator and a PSD-50 M detector (MBraun). The refinement of the structural parameters was done using the program FULLPROF [15]. Rietveld refinement was done using 5 parameters: Zero-shift, lattice parameter, and 3 parameters for the peak shape (the Lorentzian profile parameters X and Y, and Gaussian profile parameter G).

As the contribution from an amorphous phase can not be determined directly from XRD, data for an analysis of the Pair Distribution Function (PDF) were obtained with synchrotron radiation in transmission through a 1 mm sample at the high energy station 6-ID-D of the Advanced Photon Source (APS) at Argonne National Laboratory. The X-ray wavelength was 0.142013 Å and the 2D circular image plate (IP) camera Mar345 was positioned at a distance of 218.7 mm from the sample, as determined by a NIST SRM640c Si standard. No preferential orientation was observed. The data were reduced to diffraction patterns with the program FIT2D [16], corrected and processed to get the PDF with the PDFgetX2 program package [17] and refined over a range from 1.1 to 30 Å with the program PDFgui [18].

Inelastic neutron scattering experiments were performed on both samples on the Time of Flight (TOF) spectrometer IN6 at the cold source of the high-flux reactor at the Institute Laue-Langevin (Grenoble, France). The incident wavelength was 5.12 Å with an energy resolution of 0.13 meV, determined by the elastic neutron scattering on a vanadium sample. Although the resolution function broadens rapidly with increasing neutron energy, good and reliable data was obtained up to 140 meV. The IN6 spectrometer supplies a typical flux of 10^6 n/cm^{2}s on the sample, with a beam size of 25×45 mm^2.

The same measurements were additionally performed on a crushed monocrystalline silicon wafer which was also phosphorus doped, with a nominal resistivity of 0.3 Ωcm, for comparison with a polycrystalline sample.

Due to the presence of impurities in the samples, only an estimation of the Density of Phonons States (DPS) was extracted from the scattering function $S(\omega)$ in the inelastic scattering approximation and corrected for multiphonon scattering using the program LAMP [19]. The DPS of the polycrystalline Si was normalized to 1 between 0 and 73 meV and the DPS of the nanocrystalline Si samples were re-scaled according to the peaks at 20 and 60 meV, as additional contributions from hydrogen and oxides impede other means of normalization.

Measurements of the heat capacity were done on both sintered pellets between 0.1 and 400 K in a commercial Physical Property Measurement System (PPMS) from Quantum Design, using the dilution option for measurements between 0.1 and 2 K.

The elastic constants were obtained through resonant ultrasound spectroscopy (RUS), a nondestructive technique which records the frequencies of the natural modes of vibration by using two piezoelectric transducers: one which excites the sample and the other which detects the resonant response of the sample [20]. The C_{11} and C_{44} components of the elastic tensor were calculated from the first 30 resonant frequencies and fully characterize the elasticity in such an elastically isotropic sample. An in-house equipment was used with a parallelepiped-shaped sample geometry of $\sim 2.0 \,\mathrm{x} 1.5 \,\mathrm{x} 1.5\,\mathrm{mm}^3$. All measurements were performed at room temperature.

Macroscopic measurements of the resistivity, Seebeck coefficient and thermal conductivity were performed on both pellets between 2 and 300 K using the thermal transport option of the QD-PPMS.

2.3 Results and discussion

2.3.1 Microstructure of the nanocrystalline silicon

A typical TEM bright field image of the silicon nanocomposite is shown in Fig. 2.1(a). Characteristic features of the microstructure are nanocrystalline grains. Planar defects as seen in Fig. 2.1(a), marked with 1, originate from the gas phase synthesis: The silane precursor decomposes, which results in nucleation, coalescence and growth of nanoparticles. A fingerprint of the coalescence is a large twinning of the initial nanopowder and, as a consequence, of the nanocomposite. A porosity of ~ 2 to 3% is typical for silicon nanocomposites from this process [21]. A thin native oxide shell is the consequence of handling the silicon nanopowder under ambient conditions. This native oxide shell rearranges during the densification and forms oxidic precipitates within a three-dimensional interconnecting silicon network [12]. In Fig. 2.1(a), two pores and one oxidic precipitate are exemplary marked with 2 and 3 respectively. A high resolution image of a triple point between neighboring silicon grains shows that the silicon-silicon interfaces are free of oxygen (Fig. 2.1(b)).

Information about the average crystallite size of the initial nanopowder batches and of the compacted nanocomposites was obtained from X-ray diffraction and Rietveld refinement and it was found to be 22 nm and 30 nm for the nanopowder and 30 nm and 40 nm, respectively

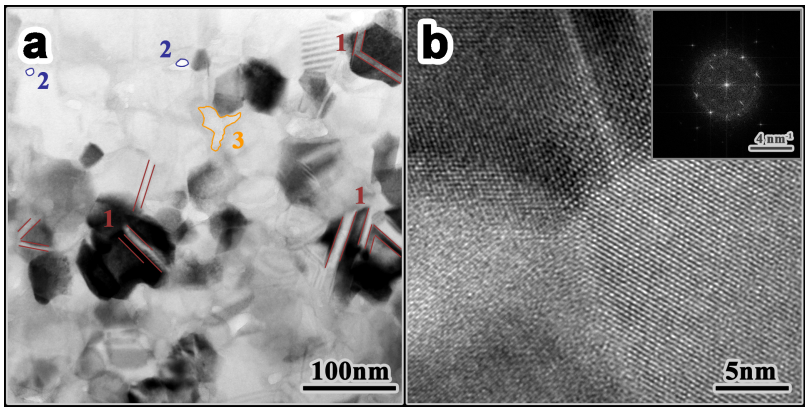

Figure 2.1: (a) TEM bright field image of a silicon nanocomposite with mean crystallite size of 40 nm. Characteristic microstructural features are twins (marked with 1), pores (marked with 2) and oxidic precipitates (marked with 3). (b) High resolution image of a triple point between silicon grains. Inset shows the Fourier transform of (b).

(Fig. 2.2), for the pellets, due to coarsening during the sintering process. For very similar samples (*i.e.* produced with comparable parameters of powder synthesis and sintering), a quantitative TEM analysis was done and compared with the microstructural model obtained by XRD [21]. This study revealed a good agreement between average crystallite size obtained from XRD and from quantitative TEM analysis, but showed that the size distribution of the crystallites broadens with mean crystallite size.

PDF analysis reveals the presence of amorphous SiO_2 in both nanocrystalline samples (Fig. 2.3). The first near neighbor distance of Si-Si is 2.35 Å, but an additional peak at 1.60 Å corresponds to the Si-O distance of crystalline alpha quartz. The data was modeled with a crystalline Si ($Fd3m$) phase and, since amorphous SiO_2 is expected to have the same short-range order as crystalline SiO_2, a crystalline alpha quartz ($P3_121$) phase with a strongly reduced particle size, refined to $\approx$ 9Å, in order to account only for the first peaks of quartz. Four peaks belonging to the amorphous SiO_2 are clearly visible bellow 3.5 Å and are indicated by arrows in Fig. 2.3. Refinement of the PDF data gave a quantity of 15(1)% of SiO_2 for the nanocrystalline sample with 30 nm and 9.6(5)% for the nanocrystalline with 40 nm. The different amount of oxide within both samples can be attributed to a higher surface-to-volume ratio of the raw powder with smaller initial particle size. Note that a 9.6(5)% content of oxide in the 40 nm sample is in excellent agreement with a TEM tomography study with 3-dimensional data reconstruction in which a very comparable sample had an oxide content of 9% [12].

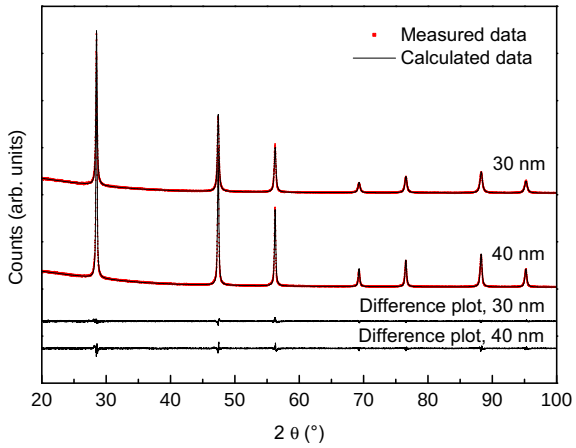

Figure 2.2: X-ray diffraction patterns of the sintered pellets, together with the calculated structure model obtained from a Rietveld refinement and difference plot between measured and calculated data. A good agreement between refined structure model and measured data can be seen. The microstructural model results in 30 nm and 40 nm average crystallite size of the two samples.

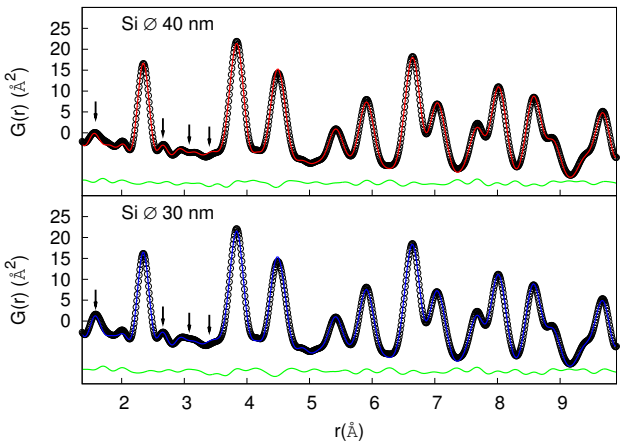

Figure 2.3: Pair Distribution Function (PDF) for both nanocrystalline Si samples. Arrows indicate the first four SiO_2 peaks, points are the data obtained while red and blue are the fit. The green line is the difference between data and fit.

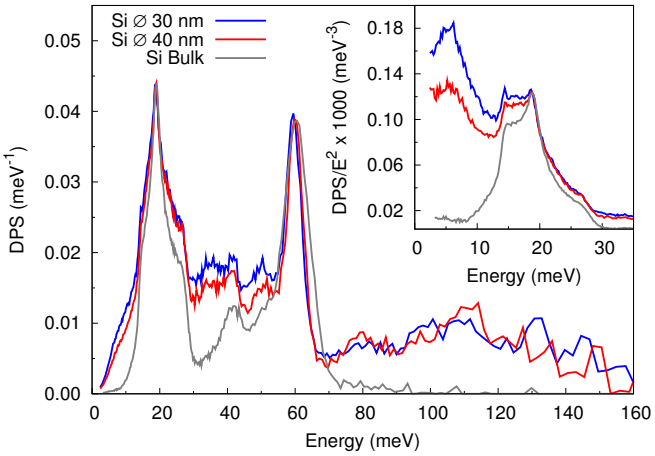

Figure 2.4: Density of Phonon States (DPS) for both nanocrystalline Si compared with reference polycrystalline Si. Inset: the reduced DPS, where the Boson peak around 6 meV is a clear indication of amorphous SiO_2.

2.3.2 Estimation for the Density of Phonon States (DPS)

An estimation for the Density of Phonon States (DPS) of the two nanocrystalline silicon samples obtained from inelastic neutron scattering, shown in Fig. 2.4, deviates significantly from the DPS of the reference polycrystalline silicon sample which presents a smooth E^2 dependence at the low energy region, better observed on the reduced DPS (inset Fig. 2.4) and has an cutoff energy of 73.4 meV. In contrast, the DPS of the nanocrystalline Si samples present a significant contribution at low energies corresponding to a pronounced peak between 2.5 and 13 meV in the reduced density of phonon states, $g(E)/E^2$, as well as additional peaks at around 30, 50 and 80 meV on the DPS ($g(E)$), and a broad feature at around 110 meV.

We interpret the specific features of the DPS as follows:

A pronounced peak observed between 2.5 and 13 meV in the reduced DPS, see inset to Fig. 2.4, is attributed to an amorphous phase, and corresponds to the Boson peak usually observed in glasses [22]. This peak originates from the amorphous SiO_2 present in the sample and is in good agreement with the Boson peak position previously observed on amorphous SiO_2 with Raman scattering ($51\,cm^{-1} = 6.3$ meV) [23] and with neutron scattering measurements (between 2 and 6 meV) [24].

The peak at around 30 meV is also associated to amorphous SiO_2, as previously observed by Fabiani *et al.* [24].

The mode with highest energy in the DPS of bulk Si is ~ 60 meV. The measured values of the DPS at higher energies and especially a broad feature at around 110 meV strongly suggest the presence of hydrogen in the nanocrystalline sample [25, 26]. A peak at 80 meV corresponds to the rocking mode of H atoms compensating a dangling Si-bond, while a prominent peak at 110 meV belongs to a bending mode of SiH_2 in which the bond angle H-Si-H is modulated [25, 26]. The Si-H modes observed in this experiment are in good agreement with previous measurements done with inelastic neutron scattering [25] and IR absorption spectrum on sputtered hydrogenated amorphous Si [26].

When the nanopowder is exposed to air, not only a shell of SiO_2 is formed around the nanoparticles due to silicon's strong affinity for oxygen, but also a significant amount of water is adsorbed which could lead to the thermal oxidation of silicon with H_2 and SiO_2 as reaction product:

$$Si + 2\,H_2O \longrightarrow SiO_2 + 2\,H_{2\,(g)}$$

which may explain the large amount of SiO_2 within the investigated samples. Furthermore, under the sintering conditions, the surplus molecular hydrogen may dissociate into H atoms being incorporated at interstitial sites of Si [27].

To conclude, the specific features found in the DPS of the investigated nanocrystalline silicon are due to contributions of SiO_2 impurities at lower energies, whereas contributions above 75 meV are attributed to H impurities.

As an additional analysis, the sound velocity was extracted from the DPS using the low energy limit of $g(E)/E^2$ [28]:

$$v_s^3 = \frac{E^2}{2\pi^2 N_V \hbar^3 g(E)} \tag{2.1}$$

where N_V is the number of atoms per unit volume ($N_V = \rho N_a/M_w$ with ρ being the density, N_a the Avogadro number and M_w the molecular weight).

Due to the presence of the Boson peak on the nanocrystalline Si samples, only a higher limit of $g(E)/E^2$ for $E \to 0$, *i.e.* lower limit of the sound velocity, can be calculated. The results are listed in Table 2.2. The value obtained for bulk Si by this method (6.73 km/s) is in good agreement with the value calculated from the elastic constants [29] (5.942 km/s).

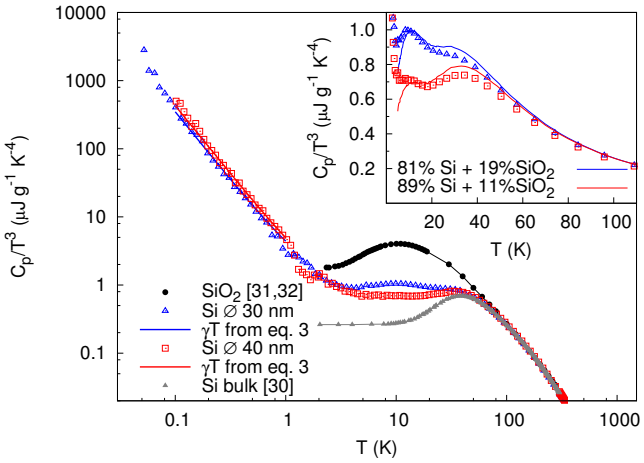

Figure 2.5: Heat capacity divided by T^3 for both nanocrystalline Si compared with crystalline Si [30] and amorphous SiO_2 [31, 32] in double logarithmic representation. Inset: interpolated fit considering the indicated mixture of Si and SiO_2 (errobars are smaller than the symbol size).

2.3.3 Influence of oxide impurities on heat capacity

The heat capacity of the nanocrystalline silicon samples was measured between 0.1 and 400 K and the data is shown in the C_p/T^3 *vs.* T representation in Fig. 2.5.

The Debye T^3 approximation valid at low temperatures for lattice specific heat is given by

$$C_V = \frac{12\pi^4}{5} N k_B \left(\frac{T}{\Theta_D}\right)^3 \tag{2.2}$$

Experimentally, the heat capacity is obtained at constant pressure (C_p). For a solid C_p and C_V differ by significantly less than a percent at low temperatures [33].

For bulk crystalline Si [30] C_p/T^3 reaches a constant value for $T \to 0$, whereas both nanocrystalline Si samples show a pronounced deviation from the Debye T^3 law.

In contrast, between 5 and 15 K, a characteristic maximum substitutes the plateau observed for the bulk Si sample in the case of the two nanocrystalline samples. The maxima can be attributed to a Boson peak characteristic for amorphous materials [34] which is more pronounced for the sample with smaller nanocrystallites. This feature can be related to the presence of amorphous SiO_2 [31] within the samples, in line with the previous statement about the larger content of SiO_2 of the sample which was produced from smaller nanoparticles.

Additionally, a steep increase in C_p/T^3 for $T \to 0$ is observed for both nanocrystalline samples, which indicates that at very low temperatures, below 2 K, an additional contribution proportional to T^α, $\alpha < 3$, is present. At a carrier concentration of $10^{20}\,\mathrm{cm}^{-3}$, there is no freeze-out of the carriers, and an electronic contribution is expected at low temperatures. Such contribution can be estimated with:

$$C_p = \gamma T + \beta T^3 \tag{2.3}$$

where γ accounts for the electronic contribution and β for the lattice contribution.

A fit with the above equation for the data below $T = 15\,\mathrm{K}$ yielded values of $\gamma = 0.097(2)\,\mathrm{mJ\,mol^{-1}\,K^{-2}}$ for the sample with smaller nanocrystallites and $\gamma = 0.120(2)\,\mathrm{mJ\,mol^{-1}\,K^{-2}}$ for the sample with larger nanocrystallites. These values are only one order of magnitude smaller than the values calculated and obtained for metals (0.6 - 2.5 $\mathrm{mJ\,mol^{-1}\,K^{-2}}$[35]).

Two approaches were used to model the T^3 contribution quantitatively. First a sum of the interpolated data of the bulk Si [30] and SiO_2 [31, 32] heat capacities using the weight percentages as free fitting parameter (inset Fig. 2.5) which resulted on a value of 11 and 19% of SiO_2 for the samples with smaller and larger nanocrystallite sizes, respectively, differing only slightly from the value extracted from the PDF refinement (9.6 and 15%). This deviation occurred because two contributions to the heat capacities at low temperatures were not considered in this fit: the electronic contribution due to a high concentration of dopants, and nanostructuration as previously observed for SiO_2 [36].

A second approach was to model the data above 2 K. While the Debye model for the heat capacity can correctly describe the high temperature (C_p), a second term has to be added to describe the excess C_p at $\sim 45\,\mathrm{K}$ caused by a flat acoustic mode in the dispersion curve, characteristic for any form of silicon [37, 38]. This term is better modelled with the Einstein model (C_E). A third term was necessary to account for the Boson peak caused by the amorphous SiO_2 contribution and can also be modelled with an Einstein term (C_{BP}):

$$C_p(T) = dC_D(T) + eC_E(T) + bC_{BP}(T) \tag{2.4}$$

$$C_D(T) = 9Nk_B\left(T/\Theta_D\right)^3 \int_0^{\Theta_D/T} \frac{e^x x^4}{\left(e^x-1\right)^2} dx \tag{2.5}$$

$$C_E(T) = 3Nk_B \frac{e^{\Theta_E/T}\left(\frac{\Theta_E}{T}\right)^2}{(e^{\Theta_E/T}-1)^2} \tag{2.6}$$

Table 2.1: Einstein temperatures and energies extracted from the heat capacity fit for the nanocrystalline Si samples and bulk reference.

	e	Θ_E		b	Θ_{BP}		d	Θ_D
	(J/g-K)	(K)	(meV)	(J/g-K)	(K)	(meV)	(J/g-K)	(K)
Bulk [30]	0.20(1)	202(3)	17.4(3)	-	-	-	0.69(1)	745(2)
∅ 40 nm	0.19(2)	194(5)	16.7(4)	0.006(1)	62(7)	5.3(6)	0.66(4)	663(65)
∅ 30 nm	0.18(2)	197(5)	16.9(4)	0.009(1)	63(8)	5.5(7)	0.65(5)	636(64)

where N is the number of atoms in the solid, k_B is Boltzmann's constant, d, e and b are the prefactors for the Debye, Einstein and Boson peak contributions and Θ_D, Θ_E and Θ_{BP} are the Debye, Einstein and Boson peak temperatures. More details about the Debye and Einstein models can be found in ref. [39].

The literature value for the bulk Debye temperature (625 K) was determined by fitting the observed C_p to the Debye formula at the point where $C_p = 3nk_B/2$ [33] and is the same as the one obtained from the Debye plateau at low temperatures. A fit with an Einstein and a Debye term for the entire range of temperatures gave a Debye temperature of 745(2) K and an Einstein temperature of 202 K resulting in an Einstein energy of 17.4 meV, which is in very good agreement with the same feature observed in this energy in the reduced DPS.

Further fittings of the data from the nanocrystalline samples showed values for the Einstein temperatures as summarized in Table 2.1 and Debye temperatures in Table 2.2. The values obtained for the Einstein temperatures were also converted to energy (1 K = 0.0862 meV). Note that the Einstein energies are in very good agreement with the features at smallest energy in the reduced DPS, see inset to Fig. 2.4.

A calculation of the sound velocity from the Debye temperature can be done using the equation [35]:

$$v_s = \frac{k_B \Theta_D}{\hbar (6\pi^2 N_V)^{1/3}} \tag{2.7}$$

which reveals a speed of sound for bulk Si of 5.71 km/s for the literature Debye temperature of 625 K [33] and 6.81 km/s for the Debye temperature of 745 K. The calculated values for speed of sound for the nanocrystalline samples are summarized in Table 2.2.

Table 2.2: Summary of the elastic constants and sound velocities in crystalline, polycrystalline and nanocrystalline Si obtained by different techniques (*The sound velocity of the nanocrystalline samples calculated from the DPS is only a lower limit value, since presence of the Boson peak prevents proper evaluation of $g(E)/E^2$ for $E \to 0$).

			v_s (km/s)		
	C_{11} (GPa)	C_{44} (GPa)	RUS	DPS	C_p, Θ_D
Bulk	160.1 [29]	80.0 [29]	5.94	6.73(5)	6.81(2)
40 nm	164(2)	59.7(6)	5.62(7)	3.49*	6.1(6)
30 nm	147(2)	52.7(5)	5.42(6)	3.30*	5.8(6)

2.3.4 Elastic constants

The values obtained for the elastic constants C_{11} and C_{44} with RUS are shown in Table 2.2 and the overall RMS errors between the calculated and measured frequencies were 0.784 and 0.586% (without excluding any resonance frequencies) for the samples with smaller and larger nanocrystallites, respectively. With those values, it was possible to extract the speed of sound using

$$\frac{3}{v_s^3} = \frac{1}{v_{long}^3} + \frac{2}{v_{trans}^3} \tag{2.8}$$

where $v_{long} = \sqrt{C_{11}/\rho}$ and $v_{trans} = \sqrt{C_{44}/\rho}$ for the polycrystals.

In contrast for single crystals, $v_{long} = \sqrt{G/\rho}$ and $v_{trans} = \sqrt{\frac{B+\frac{4}{3}G}{\rho}}$ [1]. The average speed of sound is then obtained by considering the bulk modulus $B = \frac{C_{11}+2C_{12}}{3} = 93.4\,\text{GPa}$, $C_{12} = 57.8\,\text{GPa}$ for Si [29], and the shear modulus $G = 66.9\,\text{GPa}$ calculated with the Hershey-Kröner-Eshelby averaging method [2].

The calculated sound velocities are reported in Table 2.2.

C_{11} is 164(2) and 147(2) GPa and C_{44} is 59.7(6) and 52.7(5) GPa for the samples with 40 and 30 nm nanocrystallites, respectively. Compared to the values of single crystalline silicon

[1] Corrected from published version.

[2] Hershey-Kröner-Eshelby described by Eshelby [40]:
$G^3 + \alpha G^2 + \beta G + \gamma = 0$, where
$\alpha = \frac{5C_{11}+4C_{12}}{8}$, $\beta = -\frac{C_{44}(7C_{11}-4C_{12})}{8}$, $\gamma = -\frac{C_{44}(C_{11}-C_{12})(C_{11}+2C_{12})}{8}$.

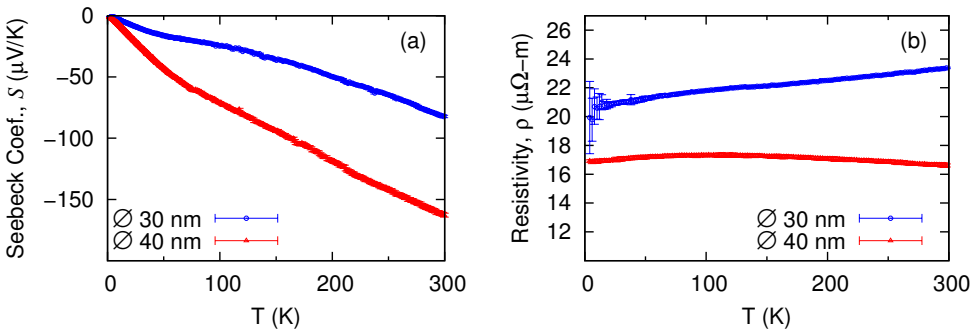

Figure 2.6: Seebeck coefficient (a) and Resistivity (b) for both nanocrystalline Si samples.

[29], the C_{11} is 3% larger for the sample with 40 nm nanocrystallites and 8% smaller for the sample with 30 nm nanocrystallites, whereas C_{44} is 25 and 34% smaller for the samples with 40 and 30 nm nanocrystallites, respectively. Furthermore, a decrease of up to 16% of the speed of sound calculated from the elastic constants was obtained upon nanostructuration and the presence of impurities.

Shintani *et al.* [41] suggested a link between the Boson peak for glasses (observed in the reduced DPS and in the C_p/T^3) and the Ioffe-Regel frequency limit for transverse phonons, above which transverse modes no longer propagate. Therefore the presence of a significant amount of amorphous SiO_2 on the sample and a substantial decrease of C_{44} when compared to single crystal bulk Si [29] further reinforce the idea that the presence of an amorphous phase disturbs mainly the propagation of transverse, shear, waves.

2.3.5 Low temperature transport properties

Macroscopic measurements of the Seebeck coefficient and resistivity are shown in Fig. 2.6 (a) and (b) whereas thermal conductivity is shown in Fig. 2.7. An increase of the absolute values of the Seebeck coefficients with temperature is observed, whereas the resistivity is relatively constant with varying temperature as expected for a highly doped semiconductor, in agreement with the electronic contribution observed on the heat capacity at low temperatures.

Room temperature values of the resistivity, Seebeck coefficient and thermal conductivity for both pellets are summarized in Table 2.3, as well as the calculated values of power factor ($S^2\rho^{-1}$) and dimensionless figure of merit (ZT), and are compared with previously

reported values on nanostructured bulk Si by Bux *et al.* [8] and with heavily doped n-type polycrystalline Si [14].

The power factor ($S^2\rho^{-1}$) at 295 K is larger for the sample with less oxides since the absolute value of the Seebeck coefficient is twice as large and the resistivity is two thirds of the values for the sample with more oxides content. When compared with heavily doped n-type polycrystalline Si [14], the sample with 40 nm nanocrystallites presents similar values of the Seebeck coefficient while the sample with 30 nm nanocrystallites presents similar values of the resistivity. The absolute value of the Seebeck coefficient of both samples were better than the values obtained for other nanostructured bulk Si prepared by a different approach [8], although the resistivity presented worse values.

Two effects can influence the value of the Seebeck coefficient in nanostructured materials: it can be reduced due to a a thermal boundary resistance between the grains leading to a temperature drop over the interfaces, or it can be enhanced due to electron-filtering effects at the interfaces [42]. Amorphous SiO_2 present in small quantities can significantly enhance the Seebeck coefficient – either because the second interface effect is more prominent than the first, or the phosphorus dopant could be incorporated preferentially within the oxide phase and is therefore partially lost for the Si.

Although the sample with more oxides (smaller nanocrystallites) presented a larger decrease in the thermal conductivity, the significantly larger power factor of the samples with less oxides (larger nanocrystallites) gives rise to an improved figure of merit at room temperature, which is comparable to the room temperature ZT previously obtained by Bux *et al.* [8].

Wang *et al.* [43] have previously measured the thermal conductivity of nanocrystalline Si with similar preparation methods and densities as the samples presented here but with a considerably lower content of oxidic precipitates. Some of their results are compared with the values obtained in this work in Fig. 2.7. They observed a T^2 dependence at low temperatures which cannot be explained by a traditional model with frequency independent grain boundary scattering, so called "gray", and proposed a new frequency-dependent model for the thermal conductivity suggesting that the mean free path for grain boundary scattering is inversely proportional to the phonon frequency. The data presented in this work features the same T^2 dependence as plotted in Fig. 2.7.

Furthermore, a calculation of the phononic contribution to the thermal conductivity (κ_{lat}) was obtained by subtracting the electronic contribution (κ_{el}) from the total thermal conductivity, which can be obtained with the Wiedemann-Franz-law:

Table 2.3: Room temperature thermoelectric properties of both nanostructured samples compared with nanostructured bulk Si previously reported by Bux *et al.* [8] and with heavily doped n-type polycrystalline Si [14].

	∅ 30 nm	∅ 40 nm	Nano-structured [8]	Poly-crystalline [14]
Seebeck coeff. (μV/K)	-81.2(9)	-161(2)	-70	-152
Resistivity (μΩ-m)	23.7(3)	16.5(9)	9.1	27.3
Thermal cond. (W/K-m)	14.8(3)	24.4(4)	7.0	64.9
Power factor (μW/K^2-m)	0.2	1.6	0.5	0.8
Figure of merit (ZT)	0.0055(2)	0.019(1)	0.023	0.004

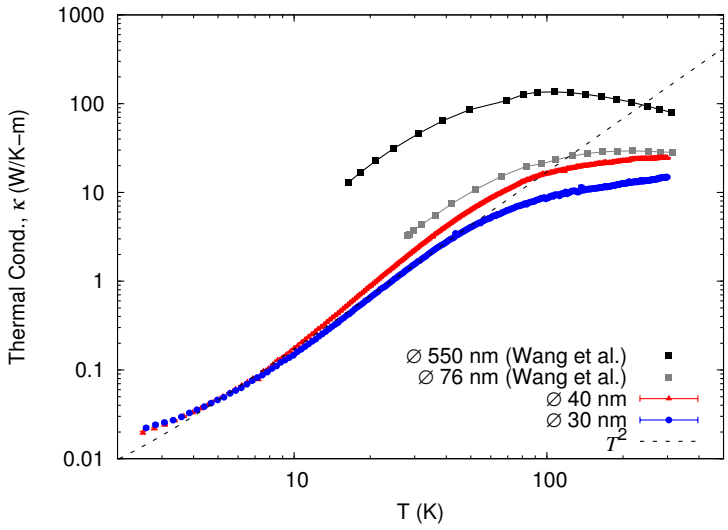

Figure 2.7: Thermal conductivity for both nanocrystalline Si samples compared with Wang *et al.* [43].

$$\kappa_{el} = \frac{LT}{\rho} \tag{2.9}$$

where $L = 2.44 \times 10^{-8}\,\mathrm{W\,\Omega\,K^{-2}}$ is the Lorenz number, T is the temperature and ρ is the resistivity.

With the measured resistivity, the electronic contribution to the thermal conductivity was very low ($\kappa_{el} = 0.3$ - $0.5\,\mathrm{W/K\text{-}m}$ at $295\,\mathrm{K}$), and therefore the phononic contribution accounts for 98% of the total thermal conductivity of both samples at room temperature.

The thermal conductivity at room temperature is $156\,\mathrm{W/K\text{-}m}$ for undoped single crystal Si [7] and decreases to $64.9\,\mathrm{W/K\text{-}m}$ in heavily doped polycrystalline Si [44]. The nanocrystalline Si samples that we produced were also highly doped with phosphorus and present an even larger decrease of the thermal conductivity ($15\,\mathrm{W/K\text{-}m}$), corresponding to 90% reduction when compared to single crystal Si and to 73% when compared to the doped sample. As expected, the sample which was produced with smaller nanoparticle size has a larger decrease on the thermal conductivity, since the surface area is larger and therefore it presents more oxide impurities.

On one hand, a large decrease of the thermal conductivity was observed upon nanostructuration not only due to grain boundaries but also due to the large amount of amorphous SiO_2. On the other hand, such impurities also had an important impact on the thermopower factor ($S^2\rho^{-1}$), resulting in a figure of merit much larger for the the sample with larger nanocrystallites (0.02) than for the sample with higher impurities concentration (0.006).

Further information on the high temperature thermoelectric properties of samples prepared with the same process as in the present paper can be found in ref. [21].

2.3.6 Phonon mean free path (λ)

The phonon mean free path at room temperature could be calculated using the values obtained for the heat capacity (C_p), sound velocity extracted with RUS (v_s) and lattice thermal conductivity (κ_{lat}):

$$\kappa_{lat} = \frac{N_V v_s \lambda C_V}{3N_a} \tag{2.10}$$

and it was found to be 8.3 and 5.4 nm for the samples and larger and smaller nanocrystallites respectively.

Previous calculation of the phonon mean free path of Si was done as in the present paper and showed a strong dependence on the temperature and impurity concentration [45].

The phonon mean free path was larger in weakly P-doped Si, decreasing with increasing temperature and reaching a value of 35 nm at room temperature, whereas in heavily As-doped Si it was temperature independent with a value around 15 nm. The values for phonon mean free path for the heavily P-doped samples containing impurities are even lower than the ones reported for weakly P-doped Si and also for the heavily As-doped Si.

2.4 Summary

Two batches of phosphorus doped silicon nanopowder with different nanoparticles sizes were produced by a gas phase synthesis and pressed into a pellet by spark plasma sintering after being exposed to air. Structural and chemical analysis of the samples by means of TEM, XRD and PDF analysis shows a 9.6 and 15% concentration of impurities in the form of amorphous SiO_2 agglomerated at the grain boundaries. The presence of additional peaks on the Density of Phonon States (DPS) obtained with inelastic neutron scattering when compared with a Si bulk reference suggests the presence of hydrogen in interstitial lattice sites in silicon and the reduced DPS showed a Boson peak at low energies due to the presence of amorphous SiO_2 in the material, which was also observed on the heat capacity (C_p) divided by T^3. The C_p was modelled with a Debye term and two Einstein terms: one describing the excess C_p at ~ 45 K due to a flat acoustic mode in the dispersion curve which is characteristic for any form of Si and the other describing the Boson contribution. The Einstein temperatures obtained with this fit are in very good agreement with the position of the same peak in the DPS. Measurement of the elastic constants with resonant ultrasound spectroscopy (RUS) showed a larger deviation of the constant C_{44} when compared to bulk Si, *i.e.*, nanostructuration and the presence of impurities disturbs mainly the propagation of transverse (shear) waves, possibly related to the link between boson peak in glasses and the propagation of transverse phonons previously suggested by Shintani *et al.*. Measurements of the thermoelectric properties of the materials reveal a large decrease of the thermal conductivity which was more significant for the sample with smaller nanocrystallites (and larger amounts of impurities) but also a significant decrease on the power factor, resulting in a thermoelectric figure of merit enhanced by a factor of three compared to bulk silicon.

2.5 Acknowledgements

The Institute Laue-Langevin (ILL - Grenoble, France) and the Advanced Photon Source (APS) at Argonne National Laboratory are acknowledged for neutron and synchrotron radiation beam time respectively. The Helmholtz Gemeinschaft Deutscher Forschungszentren is acknowledged for funding VH NG-407 “Lattice dynamics in emerging functional materials”. Z. Wang and J.E. Alaniz from UC Riverside are kindly acknowledged for sharing their data on thermal conductivity of nanocrystalline Si. D. Weber is acknowledged for scientific input and programming and S. Disch is acknowledged for helpful input for the PDF data analysis.

References

[1] M. S. Dresselhaus, G. Chen, M. Y. Tang, R. G. Yang, H. Lee, D. Z. Wang, Z. F. Ren, J. P. Fleurial, and P. Gogna. **New Directions for Low-Dimensional Thermoelectric Materials**. *Adv. Mater.*, **19**[8]:1043–1053, 2007. 37

[2] X. W. Wang, H. Lee, Y. C. Lan, G. H. Zhu, G. Joshi, D. Z. Wang, J. Yang, A. J. Muto, M. Y. Tang, J. Klatsky, S. Song, M. S. Dresselhaus, G. Chen, and Z. F. Ren. **Enhanced thermoelectric figure of merit in nanostructured n-type silicon germanium bulk alloy**. *Appl. Phys. Lett.*, **93**[19]:193121–3, November 2008. 37

[3] B. Poudel, Q. Hao, Y. Ma, Y. Lan, A. Minnich, B. Yu, X. Yan, D. Wang, A. Muto, D. Vashaee, X. Chen, J. Liu, M. S. Dresselhaus, G. Chen, and Z. Ren. **High-Thermoelectric Performance of Nanostructured Bismuth Antimony Telluride Bulk Alloys**. *Science*, **320**[5876]:634–638, 2008. 37

[4] G. H. Zhu, H. Lee, Y. C. Lan, X. W. Wang, G. Joshi, D. Z. Wang, J. Yang, D. Vashaee, H. Guilbert, A. Pillitteri, M. S. Dresselhaus, G. Chen, and Z. F. Ren. **Increased Phonon Scattering by Nanograins and Point Defects in Nanostructured Silicon with a Low Concentration of Germanium**. *Phys. Rev. Lett.*, **102**[19]:196803, May 2009. 37, 38

[5] A. I. Hochbaum, R. Chen, R. D. Delgado, W. Liang, E. C. Garnett, M. Najarian, A. Majumdar, and P. Yang. **Enhanced thermoelectric performance of rough silicon nanowires**. *Nature*, **451**[7175]:163–167, 2008. 37

[6] A. I. Boukai, Y. Bunimovich, J. Tahir-Kheli, J.-K. Yu, W. A. Goddard III, and J. R. Heath. **Silicon nanowires as efficient thermoelectric materials**. *Nature*, **451**[7175]:168–171, 2008. 37

[7] C. J. Glassbrenner and G. A. Slack. **Thermal Conductivity of Silicon and Germanium from 3K to the Melting Point**. *Phys. Rev.*, **134**[4A]:A1058–A1069, May 1964. 37, 52

[8] S. K. Bux, R. G. Blair, P .K. Gogna, H. Lee, G. Chen, M. S. Dresselhaus, R. B. Kaner, and J.-P. Fleurial. **Nanostructured bulk silicon as an effective thermoelectric material**. *Adv. Funct. Mater.*, **19**[15]:2445–2452, August 2009. 37, 50, 51

[9] Y. Lan, A. J. Minnich, G. Chen, and Z. Ren. **Enhancement of Thermoelectric Figure-of-Merit by a Bulk Nanostructuring Approach**. *Adv. Funct. Mater.*, **20**:357–376, 2010. 37

[10] T. M. Gibbons, B. Kang, S. K. Estreicher, and C. Carbogno. **Thermal conductivity of Si nanostructures containing defects: Methodology, isotope effects, and phonon trapping**. *Phys. Rev. B*, **84**[3]:035317–, July 2011. 37

[11] J. C. Thompson and B. A. Younglove. **Thermal conductivity of silicon at low temperatures**. *J. Phys. Chem. Solids*, **20**[12]:146–149, June 1961. 37

[12] G. Schierning, R. Theissmann, N. Stein, N. Petermann, A. Becker, M. Engenhorst, V. Kessler, M. Geller, A. Beckel, H. Wiggers, and R. Schmechel. **Role of oxygen on microstructure and thermoelectric properties of silicon nanocomposites**. *J. Appl. Phys.*, **110**[11]:113515–, December 2011. 38, 40, 41

[13] J. Knipping, H. Wiggers, B. Rellinghaus, P. Roth, D. Konjhodzic, and C. Meier. **Synthesis of High Purity Silicon Nanoparticles in a Low Pressure Microwave Reactor**. *J. Nanosci. Nanotech.*, **4**[8]:1039–1044, November 2004. 38

[14] A. R. Stegner, R. N. Pereira, K. Klein, H. Wiggers, M. S. Brandt, and M. Stutzmann. **Phosphorus doping of Si nanocrystals: Interface defects and charge compensation**. *Physica B*, **401-402**:541–545, 2007. Proceedings of the 24th International Conference on Defects in Semiconductors. 38, 50, 51

[15] J. Rodriguez-Carvajal. **FULLPROF V (2009)**. Technical report, Laboratoire Leon Brillouin (CEA-CNRS), France, 2009. 39

[16] A. P. Hammersley. **FIT2D: An Introduction and Overview**. ESRF Internal Report ESRF97HA02T, ESRF, 1997. 39

[17] X. Qiu, J. W. Thompson, and S. J. L. Billinge. **PDFgetX2: a GUI-driven program to obtain the pair distribution function from X-ray powder diffraction data**. *J. Appl. Crystallogr.*, **37**[4]:678, 2004. 39

[18] C. L. Farrow, P. Juhas, J. W. Liu, D. Bryndin, E. S. Božin, J. Bloch, T. Proffen, and S. J. L. Billinge. **PDFfit2 and PDFgui: computer programs for studying nanostructure in crystals**. *J. Phys.: Condens. Matter*, **19**[33]:335219, 2007. 39

[19] *LAMP, the Large Array Manipulation Program.* 39

[20] A. Migliori and J. L. Sarrao. *Resonant Ultrasound Spectroscopy: Applications to Physics, Materials Measurements, and Nondestructive Evaluation.* Wiley-Interscience, 1 edition, 1997. 40

[21] G. Schierning, T. Claudio, R. Theissmann, N. Stein, N. Petermann, A. Becker, J. Denker, H. Wiggers, R. Hermann, and R. Schmechel. **Nanocrystalline silicon compacted by spark-plasma sintering: Microstructure and thermoelectric properties.** In *MRS Proceedings*, **1267**, pages DD01–09, 2010. 40, 41, 52

[22] A. I. Chumakov, G. Monaco, A. Monaco, W. A. Crichton, A. Bosak, R. Rüffer, A. Meyer, F. Kargl, L. Comez, D. Fioretto, H. Giefers, S. Roitsch, G. Wortmann, M. H. Manghnani, A. Hushur, Q. Williams, J. Balogh, K. Parliński, P. Jochym, and P. Piekarz. **Equivalence of the Boson Peak in Glasses to the Transverse Acoustic vanHove Singularity in Crystals**. *Phys. Rev. Lett.*, **106**[22]:225501–, May 2011. 43

[23] V. Malinovsky, V. Novikov, N. Surovtsev, and A. Shebanin. **Investigation of amorphous states of SiO_2 by Raman scattering spectroscopy**. *Phys. Solid State*, **42**:65–71, 2000. 43

[24] E. Fabiani, A. Fontana, and U. Buchenau. **Neutron scattering study of the vibrations in vitreous silica and germania**. *J. Chem. Phys.*, **128**[24]:244507–1–12, June 2008. 43

[25] A. C. Wright, A. C. Hannon, R. N. Sinclair, T. M. Brunier, C. A. Guy, R. J. Stewart, M. B. Strobel, and F. Jansen. **Neutron scattering studies of hydrogenated, deuterated and fluorinated amorphous silicon**. *J. Phys.: Condens. Matter*, **19**[41]:415109, 2007. 44

[26] W. A. Kamitakahara, H. R. Shanks, J. F. McClelland, U. Buchenau, F. Gompf, and L. Pintschovius. **Measurement of Phonon Densities of States for Pure and Hydrogenated Amorphous Silicon**. *Phys. Rev. Lett.*, **52**[8]:644–647, February 1984. 44

[27] M. Stavola. **Hydrogen in Silicon and Germanium**. In *The 5th International Symposium on Advanced Science and Technology of Silicon Materials (JSPS Si Symposium)*, Nov. 2008. 44

[28] A. I. Chumakov, A. Bosak, and R. Rüffer. **Contribution of acoustic modes to the density of vibrational states measured by inelastic scattering techniques**. *Phys. Rev. B*, **80**[9]:094303–, September 2009. 44

[29] O. Madelung, U. Rössler, and M. Schulz, editors. *Landolt-Börnstein - Group III Condensed Matter*, **41A1a**, chapter Silicon (Si) elastic moduli of Si-I. SpringerMaterials - The Landolt-Börnstein Database, 2011. 44, 48, 49

[30] P. Flubacher, A. J. Leadbetter, and J. A. Morrison. **The heat capacity of pure silicon and germanium and properties of their vibrational frequency spectra**. *Philos. Mag.*, **4**[39]:273–294, 1959. 45, 46, 47

[31] P. Flubacher, A.J. Leadbetter, J.A. Morrison, and B.P. Stoicheff. **The low-temperature heat capacity and the Raman and Brillouin spectra of vitreous silica**. *J. Phys. Chem. Solids*, **12**[1]:53–65, December 1959. 45, 46

[32] Y. S. Touloukian and E. H. Buyco. *Thermophysical Properties of Matter*, **5**. IFI/Plenum, New York, 1970. 45, 46

[33] Ashcroft and Mermin. *Solid State Physics*. Thomson Learning, Inc., 1976. 45, 47

[34] V. Lubchenko and P. G. Wolynes. **The origin of the boson peak and thermal conductivity plateau in low-temperature glasses**. *Proc. Nat. Acad. Sci. U.S.A.*, **100**[4]:1515–1518, February 2003. 45

[35] C. Kittel. *Introduction to Solid State Physics*. Wiley, New York, 7th edition, 1995. 46, 47

[36] L. Wang, Z. Tan, S. Meng, A. Druzhinina, R. A. Varushchenko, and G. Li. % bf Heat capacity enhancement and thermodynamic properties of nanostructured amorphous SiO_2. *J. Non-Cryst. Solids*, **296**[12]:139–142, December 2001. 46

[37] M. Mertig, G. Pompe, and E. Hegenbarth. **Specific heat of amorphous silicon at low temperatures**. *Solid State Commun.*, **49**[4]:369–372, January 1984. 46

[38] A. D. Zdetsis and C. S. Wang. **Lattice dynamics of Ge and Si using the Born-von Karman model**. *Phys. Rev. B*, **19**[6]:2999–3003, March 1979. 46

[39] R. P. Hermann, F. Grandjean, and G. J. Long. **Einstein oscillators that impede thermal transport**. *Am. J. Phys.*, **73**[2]:110–118, February 2005. 47

[40] J. D. Eshelby. *Progress in Solid Mechanics*, **2**, page 130. North Holland Publ. Co., Amsterdam, 1961. 48

[41] H. Shintani and H. Tanaka. **Universal link between the boson peak and transverse phonons in glass**. *Nat. Mater.*, **7**[11]:870–877, November 2008. 49

[42] J. M. O. Zide, D. Vashaee, Z. X. Bian, G. Zeng, J. E. Bowers, A. Shakouri, and A. C. Gossard. **Demonstration of electron filtering to increase the Seebeck coefficient in $In_{0.53}Ga_{0.47}As/In_{0.53}Ga_{0.28}Al_{0.19}As$ superlattices**. *Phys. Rev. B*, **74**[20]:205335–, November 2006. 50

[43] Z. Wang, J. E. Alaniz, W. Jang, J. E. Garay, and C. Dames. **Thermal Conductivity of Nanocrystalline Silicon: Importance of Grain Size and Frequency-Dependent Mean Free Paths**. *Nano Lett.*, **11**[6]:2206–2213, May 2011. 50, 51

[44] T. H. T. Oaidry. **Thermal Conductivity, Seebeck Coefficient and Electrical Resistivity of Heavily Phosphorus-Doped Silicon from 313K to 673K**. Technical Report 23, South Dakota School of Mines and Technology, 1967. 52

[45] L. Weber and E. Gmelin. **Transport properties of silicon**. *Appl. Phys. A: Mater.*, **53**:136–140, 1991. 52

Chapter 3

Nanocrystalline Silicon: Lattice Dynamics and Enhanced Thermoelectric Properties

Nanocrystalline Silicon: Lattice Dynamics and Enhanced Thermoelectric Properties

Tania Claudio[1,2], Niklas Stein[3], Daniel G. Stroppa[4], Benedikt Klobes[1], Michael Marek Koza[5], Petra Kudejova[6], Nils Petermann[3], Hartmut Wiggers[3], Gabi Schierning[3], Raphaël P. Hermann[1,2]

[1] *Jülich Centre for Neutron Science JCNS and Peter Grünberg Institut PGI, JARA-FIT, Forschungszentrum Jülich GmbH, D-52425 Jülich, Germany*

[2] *Faculté des Sciences, Université de Liège, B-4000 Liège, Belgium*

[3] *Faculty of Engineering and Center for NanoIntegration Duisburg-Essen (CeNIDE), University of Duisburg-Essen, D-47057, Duisburg, Germany*

[4] *Peter Grünberg Institut PGI-5, Forschungszentrum Jülich GmbH, D-52425 Jülich, Germany*

[5] *Institut Laue Langevin, 6 rue Jules Horowitz B.P. 156, F-38042 Grenoble, France*

[6] *Technische Universitt München, Forschungsneutronenquelle Heinz Maier-Leibnitz (FRM II), Lichtenbergstr. 1, D-85747 Garching, Germany*

Abstract

Silicon has several advantages when compared to other thermoelectric materials, but until recently it was not used for thermoelectric applications due to its high thermal conductivity, 156 W/K-m at room temperature. Nanostructuration as means to decrease thermal transport through enhanced phonon scattering has been a subject of many studies. In this work we have evaluated the effects of nanostructuration on the lattice dynamics of bulk nanocrystalline doped silicon. The samples were prepared by gas phase synthesis, followed by current and pressure assisted sintering. The heat capacity, density of phonons states, and elastic constants were measured which all reveal a significant, $\approx 25\%$, reduction in the speed of sound. The samples present a significantly decreased lattice thermal conductivity, $\approx$ 25 W/K-m, which combined with a very high carrier mobility results in a dimensionless figure of merit with a competitive value that peaks at $ZT \approx 0.57$ at 973°C. Due to its easily scalable and extremely low-cost production process, nanocrystalline Si prepared by gas phase synthesis followed by sintering could become the material of choice for high temperature thermoelectric generators.

3.1 Introduction

Silicon is the second-most abundant element in the Earth's crust after oxygen. Due to its abundance and widespread usage in the semiconductor industry, the material itself and also precursors for gas phase synthesis are available in industrial quantities, at exceptional purity and quality for a comparatively low price. Si is non-toxic and unproblematic from a safety, scarcity and environmental perspective, unlike other lead or tellurium bearing thermoelectric materials. Further, the entire technology around silicon – synthesis, machining, etching, doping – is well-established and it is one of the most studied and simplest model materials in solid state physics, for which reference data is widely available [1]. Si is therefore a material of choice to study the effects of nanostructuration on the lattice dynamics and the thermal transport, which must be mastered in order to achieve good thermoelectric properties.

Single-crystalline and undoped silicon has a very high lattice thermal conductivity, 156 W/K-m at room temperature [2], related to its low density and high Young's modulus. As a direct result of its lattice structure with stiff tetrahedral covalent bonds connecting the atoms, it is a hard but brittle material.

Nanostructuration as means to improve the thermoelectric properties of a material has been intensively studied [3], since such processing decreases the lattice thermal conductivity by creating additional scattering centers for phonons at grain boundaries. By influencing mostly the lattice contribution to the thermal conductivity without also decreasing the electronic contribution, which is directly related to the electrical conductivity, an improvement in the dimensionless thermoelectric figure of merit (ZT) – and ultimately the efficiency of a thermoelectric generator – can be achieved, since $ZT = S^2\sigma T/\kappa$, where S is the Seebeck coefficient, σ the electrical conductivity, κ the thermal conductivity and T the temperature. Such approach is viable because phonons have usually a mean free path significantly larger than electrons, and the transport of the former can be disrupted without dramatically hindering the latter.

The effects of nanostructuration on the lattice dynamics were investigated by means of theoretical calculations [4, 5, 6, 7, 8, 9, 10, 11] and experimentally observed by methods such as inelastic neutron scattering [12, 13, 14, 15, 16, 17], Raman spectroscopy [18, 19], nuclear inelastic scattering (NIS) [16, 20] and measurements of the specific heat [21, 22]. Overall, these calculations and experiments reveal that an enhancement in the density of phonon states (DPS) at low energies and a broadening of the bands on the DPS is expected for nanocrystalline materials. These modifications in the vibrational modes are attributed to

the vibrations of atoms located at the grain boundaries where the atomic structure is more open than within the crystalline grains, and result in a modified force field and softening of the force constants.

Here we present a detailed experimental study about the effects of nanostructuration on the lattice dynamics and thermoelectric properties of nanocrystalline silicon which, except for the intentional doping, is virtually free of other impurities.

3.2 Experimental

3.2.1 Sample preparation

Silicon nanoparticles were synthesized by a plasma-assisted gas phase process, using a microwave reactor as described previously [23]. 1% of n-type doping was achieved by adding phosphine (PH_3) to the precursor gas. Two batches of powder were obtained by controlling the synthesis parameters: one with a nominal initial grain size of 14 nm and another with a nominal initial grain size of 52 nm confirmed by BET[1]. The nanopowder is functionalized at the surface by hydrogen during the synthesis, so that no oxygen impurities can attach at the surface of freshly synthesized powder. The nanopowder was bottled under inert conditions and kept within an inert atmosphere to prevent contamination with oxygen during further processing. Sintering was carried out immediately after synthesis, with an absolute minimum time for filling the crucible and starting the sintering process. This effort is necessary, as a contamination of the nanopowder with oxygen can significantly influence the physical properties of the samples as reported previously [24].

The nanopowder was compacted into 2 cm diameter dense pellets with a spark plasma sintering furnace from FCT Systeme GmbH in a 1 mbar Ar atmosphere. For the first batch (14 nm) sintering was carried out during 3 min (sample A). The second batch (52 nm) was divided into two parts. One part was sintered for 3 min (sample B) and the other for 30 min (sample C). Heating and cooling rates for all samples were fixed to 100 K/min. The sintering temperature was 1150°C and a 35 MPa pressure was applied during sintering.

[1]BET (Brunauer, Emmett, Teller): surface area analysis

3.2.2 Microstructural characterization and composition

Transmission Electron Microscopy (TEM) was used for structural characterization of the sintered pellets in a FEI-Tecnai microscope with a field-emission electron gun operating at 200 kV. TEM samples were prepared from the sintered pellets by a precision Focused Ion Beam (FIB) system using gallium ions.

In order to verify the average crystallite size of the nanocrystalline pellets, X-Ray diffraction (XRD) was performed using synchrotron radiation at the high energy station 6-ID-D of the Advanced Photon Source (APS) at Argonne National Laboratory. The sample was 1 mm thick and the experiment was performed in transmission geometry in order to probe the bulk of the pellets. The X-ray wavelength was 0.124659 Å and a General Electric amorphous silicon detector was positioned at a distance of 1849 mm from the sample, a distance determined by a NIST640c Si standard. The data were reduced to diffraction patterns with the program FIT2D [25] and no preferential orientation was observed. Rietveld refinement were carried out using the program FULLPROF [26], taking into consideration the Debye-Scherrer broadening of the diffraction peaks.

The average crystallite size was also investigated by Small Angle Neutron Scattering (SANS) measurements carried out using instrument KWS1 operated by the Jülich Centre for Neutron Science (JCNS) at the FRM II (Garching, Germany) [27]. In the present work only the essential results concerning characteristic crystallite sizes will be presented, while further analysis based on Gaussian random fields [28] will be published elsewhere.

The elemental analysis was performed at the Prompt Gamma Ray Activation Analysis (PGAA) instrument positioned at the neutron guide NL4b of the Forschungs-neutronenquelle Heinz Maier-Leibnitz (FRM II - Garching, Germany) [29]. The cold neutron flux used for the measurement was $6.1\text{x}10^{10}$ n.cm^{-2}s^{-1}. A high-purity germanium (HPGe) detector was used to detect the gamma rays produced in the sample by neutron capture reactions. The emitted gamma rays have a characteristic energy which depends on the element or isotope which absorbs the neutrons. The peak-area is proportional to the concentration of the element in the sample. This method is therefore a non-invasive way to chemically characterize the sample which gives precise information about the impurities and its amount in percentages, and it is a method of choice which can give nondestructively information about elements such as hydrogen and boron.

3.2.3 Lattice dynamics

Resonant Ultrasound Spectroscopy (RUS) is a nondestructive technique which gives access to the elastic tensor by recording the frequencies of the natural modes of mechanical vibrations. Parallelepiped samples are positioned between two piezoelectric transducers, one driving and the other recording the response [30] in order to obtain the elastic constants C_{11} and C_{44} that fully characterize the elasticity in an elastically isotropic samples. The first 30 resonance frequencies were measured on samples with ∼2.0x1.5x1.5 mm^3 dimensions. The RMS errors between the calculated and measured frequencies were 0.29% and 0.21% for the samples with smaller and larger nanocrystallites, respectively.

The Density of Phonon States (DPS) of all samples was obtained by inelastic neutron scattering measurements performed on the Time of Flight (TOF) spectrometer IN6 at the cold source of the Institute Laue-Langevin (Grenoble, France). The incident wavelength was 5.12 Å with an elastic energy resolution of 0.13 meV, as determined by the elastic neutron scattering on a vanadium sample.

The specific heat, C_p, was obtained in a commercial Physical Property Measurement System (PPMS) from Quantum Design for all sintered pellets between 4 and 400 K. The specific heat of a polycrystalline Si sample was also measured for comparison.

3.2.4 Thermoelectric transport measurements

Thermoelectric transport characterization was carried out between room temperature and 1000 °C. The Seebeck coefficient S and the specific electrical conductivity σ were measured on a bar-shaped sample by a direct measurement technique, using a commercial system (ZEM3 by Ulvac Technologies, Inc.). The thermal diffusivity λ_θ was measured by a laser flash method on a sample of 10x10x1 mm^3 size, using a commercial system (LFA 457 MicroFlash by Netzsch Thermal Analysis GmbH). The thermal conductivity was then calculated with $\kappa = \lambda_\Theta \cdot C_p \cdot \rho$, using a value for the density of the pellets (ρ) obtained by the Archimedes method at room temperature. The bulk values of heat capacity were used for this calculation, since typically in this temperature range the heat capacity of bulk and nanocrystalline Si does not differ, as confirmed from the C_p results.

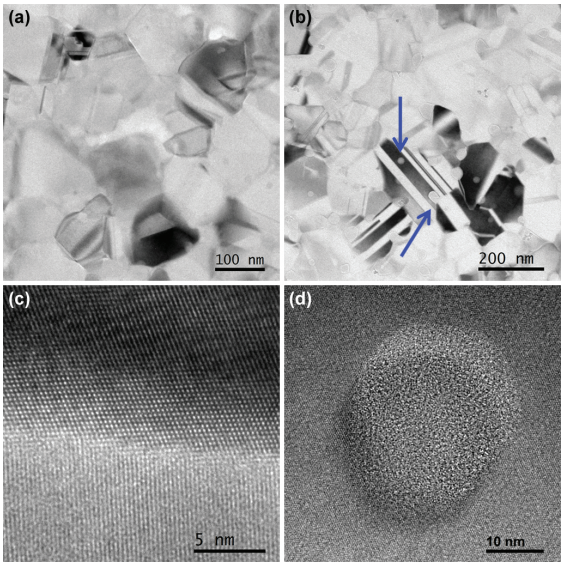

Figure 3.1: TEM bright-field images of sample A (a) and sample C (b) and high resolution TEM of grain boundary between two nanocrystals of sample A (c) and of an amorphous precipitates on sample C (d). Arrows indicate amorphous precipitates.

3.3 Results and Discussion

3.3.1 Microstructural and chemical characterization

The average nanocrystallite diameters, D, as well as the strain in the sintered pellets was estimated by refinement of the X-ray diffraction pattern and the results were compared with images obtained from TEM, see Fig. 3.1 (a) and (b), and with the results from a Kratky plot analysis of the SANS data, shown in Fig. 3.2. The Kratky plot exhibits a maximum at q_{max}, which can be used to estimate the average crystallite diameter D using the pseudo-Guinier radius $R_{pg} = D/2 = \sqrt{3}/q_{max}$ [31]. The values obtained by these three methods are summarized in Table 3.1.

Sample A had an average crystallite size of 40(2) nm from XRD and 41.6 nm from SANS whereas TEM reveals grains ranging between 48 and 264 nm with mean average of 114 nm. The sample C had a grain size distribution between 47 and 246 nm with mean size of 112 nm, and also showed amorphous precipitates with average size of 29 nm. The differences seen between TEM, SANS and XRD analysis have their origin in sensitivity of TEM to the grain size whereas XRD is sensitive to the crystallite size, which can be smaller than the grain size due to the existence of planar defects and intra grain boundaries. Furthermore, SANS

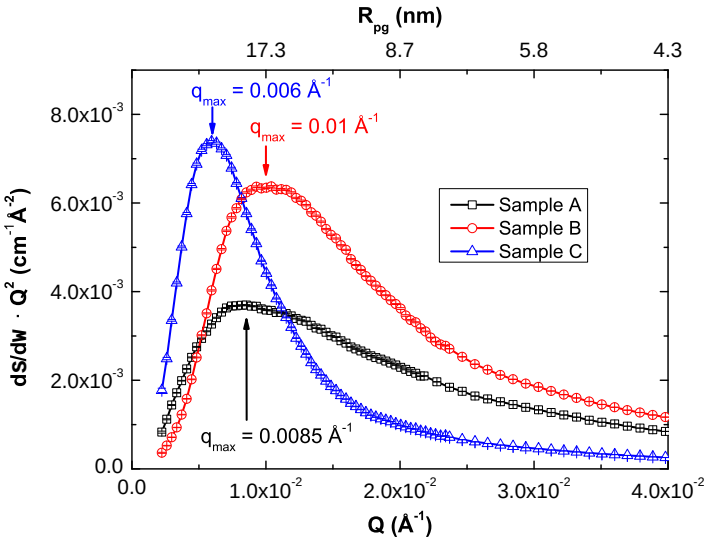

Figure 3.2: Kratky plot of the SANS curves. Each curve exhibits a broad maximum, which yields the *pseudo*-Guinier radius R_{pg}.

Table 3.1: Summary of nanocrystallite sizes (D) and strain (ε) obtained by TEM analysis, XRD refinement and SANS.

	TEM			XRD		SANS
	D_{min} (nm)	D_{max} (nm)	D_{av} (nm)	D (nm)	ε (%)	D (nm)
Sample A	48	264	114	40(2)	0.00138	42
Sample B	-	-	-	42(2)	0.00133	58
Sample C	47	246	112	33(1)	0.00150	34

curves strongly depend on the size distribution of the scattering entities and may also be affected by inter-particle effects in the present case, though it still represents a measure of characteristic length scales [31]. Besides, XRD and SANS are methods averaging over a larger volume, whereas TEM only gives an impression of a very small sample volume, not necessarily fully representative for the complete pellet.

The samples which were processed with the same sintering parameters, but with initially different nanoparticles sizes (14 and 52 nm for samples C and A, respectively), present only a small different average nanocrystallite sizes after sintering. Sample C presented not only grain growth during sintering, but also a larger amount of defects such as twins and a certain amount of amorphous precipitates, which are both visible in Fig. 3.1 (b), resulting

Table 3.2: Summary of the elastic constants and sound velocities in nanocrystalline Si compared with bulk Si obtained by different techniques.

			v_s (km/s)		
	C_{11} (GPa)	C_{44} (GPa)	RUS	DPS	C_p, Θ_D^{LT}
Bulk	160.1 [32]	80.0 [32]	5.94	6.73(5)	5.70(5)
Sample A	173(3)	59.0(8)	5.0(1)	5.0(3)	4.44(9)
Sample C	172(3)	58.2(7)	4.9(1)	4.3(3)	4.2(1)

in an increased strain as obtained from XRD refinement. A grain boundary between two nanocrystals in sample A with different relative orientation without any amorphous layer is shown in Fig. 3.1 (c) and a high resolution image of an amorphous precipitates on sample C in Fig. 3.1 (d). Those precipitates are rather spherical and are found on all images acquired on this sample, indicated by blue arrows in Fig. 3.1 (b).

Overall, although the three different measurements yielded different values of nanocrystallite sizes, the same trend in sizes is observed, ranging from the smallest being sample C and the largest being sample B.

Samples B and C were investigated exemplarily by PGAA. The spectra reveal that the samples were 99.0(1)% Si with 1.0(7)% of P dopant as expected. A small amount of H (0.20(1)%) was detect on the sample with smaller initial nanopowder size (sample C). Furthermore, in both samples, a very small ppm contribution of boron was detected. This impurity could originate from a contamination of the precursor silane, which is prepared by fractional distillation, as it is not easy to completely separate silane from diborane.

3.3.2 Lattice dynamics

Samples A and B had the same properties in all measurements within their experimental errors: density of phonon states (DPS), specific heat (C_p) and resonant ultrasound spectroscopy (RUS). Therefore only the results for sample A are being discussed here.

The values obtained for the elastic constants C_{11} and C_{44} with RUS are summarized in Table 3.2. The speed of sound was then calculated: $3/v_s^3 = 1/v_{long}^3 + 2/v_{trans}^3$, where $v_{long} = \sqrt{C_{11}/\rho}$ and $v_{trans} = \sqrt{C_{44}/\rho}$ for the polycrystals, are the long and transversal speed of sound, respectively. The values of speed of sound for single-crystalline Si were calculated previously (Ref. [24]) using the Hershey-Kröner-Eshelby average.

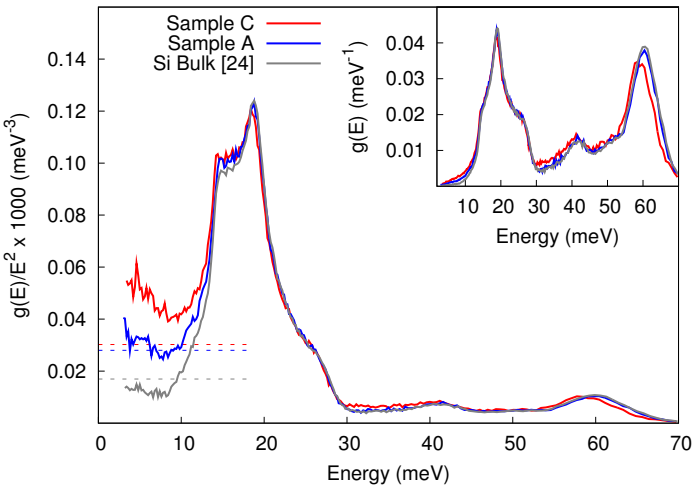

Figure 3.3: Reduced Density of Phonon States (DPS) for two samples of nanocrystalline Si compared to previously reported results on polycrystalline Si, doted lines indicate the asymptotic limits from RUS. Inset: DPS.

The elastic constant $C_{11} = 172(3)$ and $173(3)$ GPa for the samples with smaller and larger nanocrystallites sizes, respectively, corresponding to the bulk modulus (B) is $\approx 8\%$ larger than in single crystalline Si. The shear modulus, $G = C_{44} = 58.2(7)$ and $59.0(8)$ GPa, is $\sim 25\%$ smaller than in single crystalline Si. Such a decrease in the resistance to shear deformation (G) combined with an increase of the resistance to dilation (B) shows that the mechanical properties of a material with as many grain boundaries and defects are significantly modified when compared with the single-crystalline material, leading to a softening of the material. This is also confirmed by the decrease of the speed of sound calculated from the elastic constants. Such a decrease relates to a decrease in thermal conductivity.

The DPS of two samples of nanocrystalline Si obtained from inelastic neutron scattering are shown in Fig. 3.3 and is compared with polycrystalline Si [24]. Note that the area under the DPS curve of all samples was normalized to 1 between 0 and 70 meV.

In the incoherent scattering approximation, and because the sample essentially contains only one chemical element, the speed of sound can be obtained from the low energy limit of $g(E)/E^2$ with $1/v_s^3 = 2\pi^2 N_V \hbar^3 g(E)/E^2$ where N_V is the number of atoms per unit volume [16]. In the case of the nanocrystalline Si samples an increase on the Debye level, $\lim_{E\to 0} g(E)/E^2$, in the reduced DPS is observed. Note that the incoherent scattering approximation is not perfectly suitable for silicon which is a strong coherent scatterer. Therefore, the speed of sound is obtained by a second approach using RUS measurements, and the data

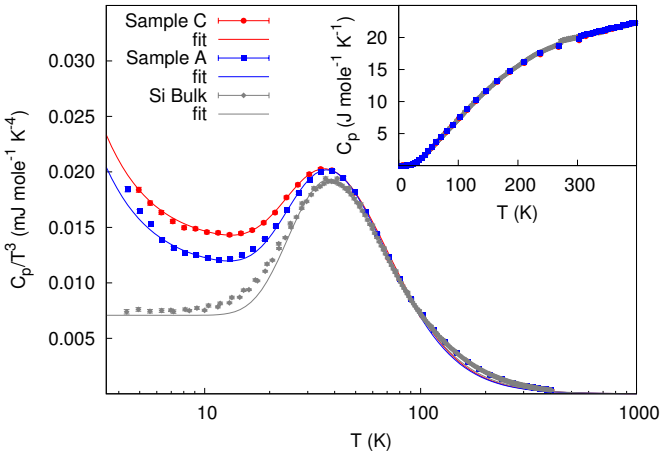

Figure 3.4: Specific heat divided by T^3 for both nanocrystalline Si compared with polycrystalline Si. Inset: Specific heat (error bars are smaller than the symbol size).

is compared. An extrapolation using the asymptotic limit from RUS, considering the speed of sound summarized in Table 3.2, shown as dotted lines in Fig. 3.3, reveals a fair agreement of both methods.

On one hand, the sample containing a small amount of grain boundaries (sample A) presented the same results of speed of sound calculated from the reduced DPS and obtained with RUS, with only a small part of the reduced DPS data being above the asymptotic limit from RUS. On the other hand, the reduced DPS of the sample with larger amount of grain boundaries, defects and amorphous contribution (sample C) is significantly above the asymptotic limit from RUS and has a pronounced increase for $E \to 0$. We therefore conclude that the excess states in the reduced DPS, which is probed only above 3 meV, that are above the asymptotic limit can be considered as contribution due to the larger amount of grain boundaries, defects and amorphous inclusions.

The specific heat, represented as C_p/T^3 *vs.* T, of the nanocrystalline silicon samples measured between 4 and 400 K compared to bulk Si, is shown in Fig. 3.4. The nanocrystalline samples have the same C_p at high temperatures as bulk Si. Below 30 K an increased lattice contribution, related to the increase Debye level and decreased speed of sound, is observed. Further, an electronic contribution, linear in temperature, and thus $\propto 1/T^2$ in C_p/T^3, is observed at the lowest temperatures, because with such high carrier concentrations, in the % range, there is no freeze-out of the charge carriers as would be expected in semiconductors.

At the lowest temperatures, a simple model of the heat capacity can be designed by considering an electronic contribution (γT) and a lattice contribution that can be described

Table 3.3: Values of the electronic contribution (γ), Einstein and Debye temperatures as well as heat capacity prefactors (e and d) obtained with a fit of the equation 4.1 for low temperatures (below 90 K).

	γ	e	Θ_E		d	Θ_D^{HT}	
	(mJ/mol-K^2)	(J/mol-K)	(K)	(meV)	(J/mol-K)	(K)	(meV)
Bulk	-	3.8(3)	188(2)	16.2(2)	11.4(3)	501(17)	43(2)
Sample A	0.114(5)	2.76(7)	186(1)	16.0(1)	9.8(1)	410(5)	35.3(5)
Sample C	0.12(2)	2.02(3)	184(1)	15.9(1)	11.2(9)	402(11)	34.6(9)

using the Debye model and an Einstein term to describe the excess C_p at approximately 45 K [24]:

$$C_p(T) = \gamma T + dC_D(T) + eC_E(T) \tag{3.1}$$

where d and e are prefactors for the Debye and Einstein contributions, $C_D(T)$ and $C_E(T)$ respectively. More details about the Debye and Einstein models can be found in Ref. [33, 34, 35]. A fit to the data up to 90 K yields parameters as summarized in Table 3.3. The electronic contribution ($\gamma \approx 0.1\,\mathrm{mJ\,mol^{-1}\,K^{-2}}$) is close to that obtained on the specific heat of metals (0.6 - 2.5 $\mathrm{mJ\,mol^{-1}\,K^{-2}}$)[34], and shows a significant presence of electronic contribution in the samples. The values obtained for the Einstein and Debye temperatures were also converted to energy (1 K = 0.0862 meV) and the Einstein energies are in very good agreement with the feature observed at this energy ($\approx$ 16 meV) in the reduced DPS (Fig. 3.3). The Debye temperature obtained with this fit in this temperature range (Θ_D^{HT}) differs from the temperature obtained considered only the low temperature Debye plateau (Θ_D^{LT}), as it probes higher energies phonon modes. For the calculations of the speed of sound from the specif heat, $v_s = k_B\Theta_D^{LT}/\hbar(6\pi^2 N_V)^{1/3}$, only the Debye plateau was considered, and yields values as summarized in Table 3.2.

3.3.3 Thermoelectric and transport measurements

The general trend of the electrical conductivity (σ) of all samples between room temperature and 750°C demonstrates a decrease with temperature as expected for degeneratedly doped semiconductors (Fig. 3.5 (a)). This occurs due to the increase of the lattice vibrations in

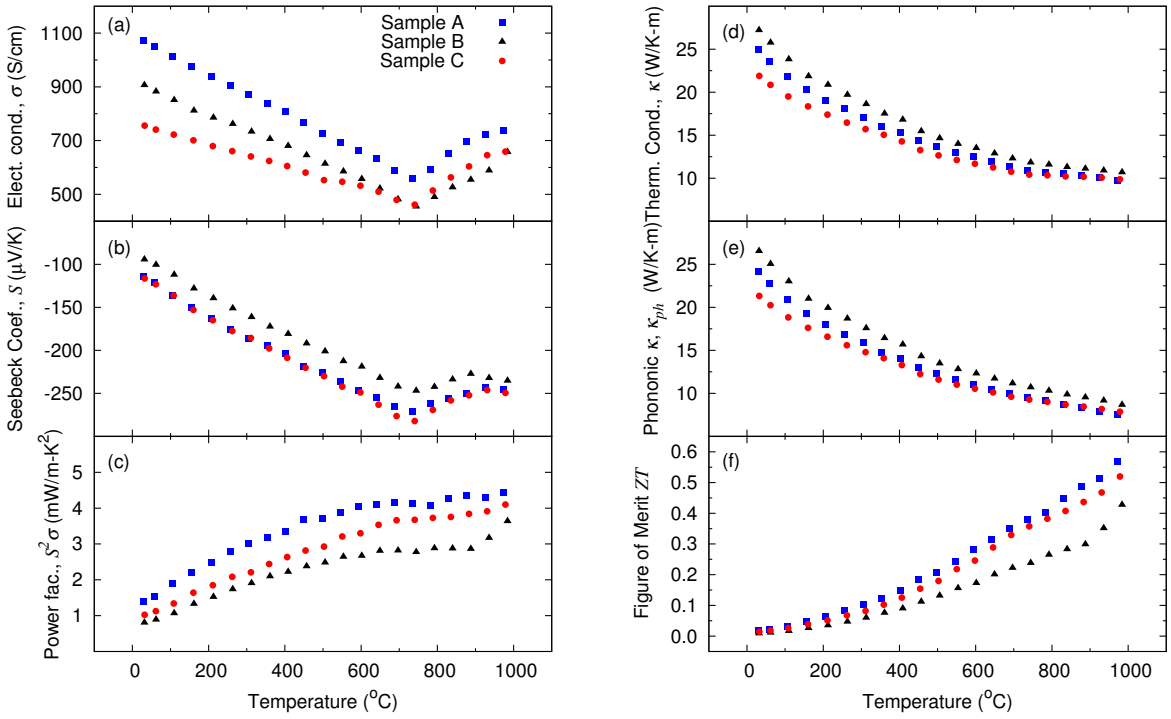

Figure 3.5: Thermoelectric characterization of the 3 nanocrystalline Si samples: (a) electrical conductivity; (b) Seebeck coefficient; (c) calculated power factor; (d) thermal conductivity; (e) calculated lattice contribution to the thermal conductivity and (f) calculated dimensionless figure of merit.

this range of temperature, *i.e.* electron scattering by phonons dominates the observed temperature trend, as in metals. Above this temperature an additional contribution is observed leading to a kink in σ which increases with temperature above temperatures of 750°C. Such a kink in a n-type semiconductor might be due to a bipolar contribution [36], when additional p-type charge carriers are thermally activated over the band gap of the semiconductor. An alternative explanation for a similar kink previously observed on nanocrystalline Si by Bux *et. al.* [37], is the kinetics of dopant precipitation related to the retrograde solid solubility of phosphorus in silicon [38]. As the temperature rises, additional phosphorus atoms are being incorporated at substitutional lattice sites and become electrically activated. This leads to a rapid increase in carrier concentration and consequently an increase of the electrical conductivity as well as a decrease of the Seebeck coefficient. This is possible because at low temperature less phosphorus atoms are electrically activated than chemically incorporated. Both effects – bipolar contribution and dopant migration – are difficult to distinguish since they occur within a very similar temperature range, but a tendency towards hysteresis effects within heating and cooling cycles points towards a complicated dopant kinetic as an explanation of this kink rather than the bipolar effect.

The Si sample with smaller nanocrystallite sizes presents a lower electrical conductivity between room temperature and 750°C when compared with the two other samples. The sample which was sintered for a longer period of time has lower σ than the sample with large nanocrystallites sintered for a short time. Both samples which were sintered for a short period of time presented similar values of the Seebeck coefficient, *i.e.*, a very similar charge carrier concentration (Fig. 3.5 (b)). The sample with smaller nanocrystallites presented a lower σ than the sample with larger crystallites, due to a large amount of grain boundaries, defects and amorphous contribution leading to a more pronounced scattering of electrons. This results in a better power factor for the sample with large nanocrystallites, but sintered for a short period of time (Fig. 3.5 (c)).

Although the sample which was sintered for a longer period of time (sample B) had a slightly higher density when compared with the other samples (only 1.1% higher , see in Table 3.4), its electronic properties were not better. During the long sintering period (30 minutes) at high temperatures (1150°C), diffusion processes occur. Those do not only lead to a healing of defects, which rather improve the crystalline quality of the sample as seen by higher values of thermal conductivity (Fig. 3.5 (d)) and by the higher density, but also to diffusion of the impurities (dopants). The latter have a tendency to aggregate on grain boundaries. This agglomeration of dopants can be seen in the weak increase in σ

for $T > 750$°C. Overall, the power factor of this sample is lower than for the two samples sintered within only 3 minutes (samples A and C), see Fig. 3.5 (c).

The charge carrier concentration (n) can be estimated from the slope of the Seebeck coefficient (for $T < 750$°C) [36]:

$$S = \frac{8\pi^2 k_B^2}{3eh^2} m^* T \left(\frac{\pi}{3n}\right)^{2/3} \tag{3.2}$$

where k_B is the Boltzmann constant, h is the Planck constant, e is the elementary charge and $m^* = 1.13 m_{e,0}$ [39] is the reduced band effective mass of electrons in silicon. Band transport in one parabolic band as well as an energy independent scattering time were assumed to derive this relatively simple transport model from the Mott equation [40], strictly valid only in metals but useful also for the analysis of degenerated doped semiconductors. A comparison between Hall data and an evaluation of the Seebeck coefficient for nanocrystalline silicon showed a decent agreement for electron mobility and charge carrier concentration [41], so that this simple approximation is used here to compare nano silicon transport data. From the combined measurement of the Seebeck coefficient and the electrical conductivity, we estimated the mobility of the charge carriers, μ, with $\sigma = ne\mu$. The values obtained are summarized in Table 3.4 and compared with literature data.

Table 3.4: Summary of room temperature properties for all nanocrystalline Si samples, compared with previously published results on spark plasma sintered bulk nanocrystalline Si and single-crystal Si.

	Single-cryst. [37]	Nanocryst. [37]	Nanocryst. [24]	Sample A	Sample B	Sample C
Nanoparticles production	-	Ball-milling	Gas phase synthesis	Gas phase synthesis		
SPS temperature (°C)	-	-	1050	1150	1150	1150
SPS hold time (min)	-	-	3	3	30	3
Additives / Impurities	-	(from ball-mill)	P, SiO_2, H	P	P	P
Av. nanocryst. size (nm)	-	50-100	30	42	58	33
Density (g/cm^3)	2.329	-	2.189	2.259	2.284	2.257
S (µV/K)	-86	-70	-81.2	-94.3	-116	-114
ρ (µΩ-m)	27.3	9.1	23.7	9.3	11.0	13.2
n ($\times 10^{26}$ m^{-3})	4.5	4.6	-	1.3	1.6	1.3
μ ($\times 10^{-4}$m^2/V-s)	42.8	15.1	-	51.8	36.2	37.5
κ (W/K-m)	101.6	7.0	14.8	25.0	27.2	21.9
$S^2\sigma$ (mW/K^2-m)	0.3	0.5	0.2	1.4	0.8	1.0
ZT at RT	0.008	0.023	0.0055	0.017	0.009	0.014
ZT_{max} at 980°C	-	0.68	-	0.57	0.43	0.52

Comparing the samples produced from different nanoparticle batches (14 nm vs. 52 nm), but sintered for the same short period of time (3 minutes), no significant decrease of the thermal conductivity was observed, since sample C showed a more pronounced grain coarsening during sintering. The sample with initially smaller nanocrystallite size has a thermal conductivity κ which is 12% lower at room temperature than the sample with initially larger nanocrystallite size, but at high temperatures the thermal conductivity data of both samples converges. The lattice contribution to the thermal conductivity accounts for up to 97% of the total thermal conductivity at room temperature and decreases to around 77% at the highest measured temperature. In single crystalline silicon, 90% of the heat is transported by phonons with mean free path larger than 100 nm [42]. Therefore, an average grain size around 100 nm or slightly smaller is already effective in lowering the lattice thermal conductivity as can be seen from the investigated samples.

The thermal conductivity of the pure nanocrystalline samples studied in this paper is still large when compared with previously reported results on nanocrystalline Si [24, 37, 41], but in those samples, several impurities were present either from exposing the nanopowder to air before sintering [24, 41] or due to additives used for nanopowder preparation with ball-milling [37]. These impurities may significantly affect the mobility of charge carriers (μ), leading to a smaller power factor than for the here reported samples, see Table 3.4.

Therefore, despite of a large thermal conductivity, the dimensionless figure of merit of the silicon nanocomposites investigated herein, still reaches competitive values due to a very high carrier mobility resulting in comparatively high power factors. With a ZT of 0.57 at 973°C, the sample produced with 52 nm nanoparticles and sintered for 3 minutes can compete with other results published so far [37], with the advantage of a more easily scalable production process.

3.4 Conclusions

The three different nanocrystalline Si samples which were analyzed in this work showed interesting lattice dynamics and thermoelectric properties depending on its synthesis parameters. Both samples which were prepared with the same nanoparticle size, but were sintered for different periods of time presented same results on the study of its lattice dynamics: a decrease in the speed of sound when compared to single-crystalline Si. But the sample which was sintered for a longer period (30 min), showed also a decrease in the thermoelectric properties with a lower power factor and an elevated thermal conductivity due to improved crystallinity.

The sample with small initial nanoparticle size showed a significant grain growth during sintering as analyzed by XRD refinement and TEM, and also a larger amount of defects and a certain amount of amorphous precipitates, leading to a further decrease on the speed of sound and to an excess of vibration modes at low energies. It also presented slightly worse electronic properties which compensates the lower thermal conductivity and leads to a similar dimensionless figure of merit as the sample prepared with larger nanoparticles and same sintering parameters.

A systematic trend in the decrease of the speed of sound obtained from the density of phonon states, resonant ultrasound spectroscopy and specific heat combined with the large amount of grain boundaries in nanostructured Si materials resulted in a thermal conductivity four times lower than for a single-crystal.

When compared with previously reported results on nanocrystalline Si, the samples still present a somewhat large thermal conductivity which is compensated by a very high power factor and results in competitive values of the dimensionless figure of merit with a peak ZT of 0.57 at 973°C. When compared to other materials which are used in this temperature range such as nanocrystalline SiGe, Si has a ZT which is approximately half of the results reported so far (1.3 at 900°C [43]), with the advantage of being approximately 14 times cheaper than SiGe.

Since the thermal conductivity of the nanocrystalline Si samples presented in this work is still large when compared to other thermoelectric materials, further optimization of the parameters leading to the reduction of the thermal conductivity could lead to an even better ZT value.

Furthermore, studies have shown that the energy cost of Si nanopowder production through gas phase synthesis is drastically reduced with increasing production amount [44]. Therefore, when compared with other methods such as ball-milling, gas phase synthesis has the great advantage of being a continuous and a more easily scalable method.

3.5 Acknowledgments

The Institute Laue-Langevin (ILL - Grenoble, France) and the Advanced Photon Source (APS) at Argonne National Laboratory are acknowledged for neutron and synchrotron radiation beam time respectively. The Helmholtz Gemeinschaft Deutscher Forschungszentren is acknowledged for funding VH NG-407 “Lattice dynamics in emerging functional materials”. We would like to thank Dr. Z. Di (JCNS, Forschungszentrum Jülich, outstation at FRM

II) for support during beam time. Dr. D. Bessas is kindly acknowledged for collecting the PGAA data, D. Meertens for TEM sample preparation, D. Weber for scientific input and Dr. K. Friese for input on XRD refinement.

References

[1] O. Madelung, U. Rössler, and M. Schulz, editors. *Landolt-Börnstein - Group III Condensed Matter*, **41**, chapter Silicon (Si). SpringerMaterials - The Landolt-Börnstein Database, 2011. 61

[2] C. J. Glassbrenner and G. A. Slack. **Thermal Conductivity of Silicon and Germanium from 3K to the Melting Point**. *Phys. Rev.*, **134**[4A]:A1058–A1069, May 1964. 61

[3] M. S. Dresselhaus, G. Chen, M. Y. Tang, R. G. Yang, H. Lee, D. Z. Wang, Z. F. Ren, J. P. Fleurial, and P. Gogna. **New Directions for Low-Dimensional Thermoelectric Materials**. *Adv. Mater.*, **19**[8]:1043–1053, 2007. 61

[4] D. Wolf, J. Wang, S.R. Phillpot, and H. Gleiter. **On the thermodynamic relationship between nanocrystalline materials and glasses**. *Phys. Lett. A*, **205**[4]:274–280, September 1995. 61

[5] S.R. Phillpot, J. Wang, D. Wolf, and H. Gleiter. **Computer simulation of the structure and dynamical properties of grain boundaries in a nanocrystalline model material**. In *Materials Science & Engineering A (Structural Materials: Properties, Microstructure and Processing)*, **A204**, pages 76–82, Div. of Mater. Sci., Argonne Nat. Lab., IL, USA, December 1995. Elsevier Office of Naval Res. Office of Naval Res. 61

[6] M.-S. Jeng, R. Yang, D. Song, and G. Chen. **Modeling the Thermal Conductivity and Phonon Transport in Nanoparticle Composites Using Monte Carlo Simulation**. *J. Heat Transfer*, **130**[4], April 2008. 61

[7] R. Singh and S. Prakash. **Vibrational properties of nanocrystalline fcc Ni_3Fe**. *Indian J. Phys.*, **77A**[3]:243–246, May 2003. 61

[8] R. Singh, S. Prakash, R. Meyer, and P. Entel. **Phonon density of states in nanocrystalline ^{57}Fe**. *Pramana J. Phys.*, **60**[3]:547–556, March 2003. 61

[9] A. I. Potapov, I. S. Pavlov, and S. A. Lisina. **Acoustic identification of nanocrystalline media**. *J. Sound Vib.*, **322**[3]:564–580, May 2009. 61

[10] J. Wang, D. Wolf, S. R. Phillpot, and H. Gleiter. **Phonon-induced anomalous specific heat of a model nanocrystal by computer simulation**. In *Nanostruct. Mater.*, **6**, pages 747–750, Div. of Mater. Sci., Argonne Nat. Lab., IL, USA, January 1995. 61

[11] S. Stankov, M. Miglierini, A. I. Chumakov, I. Sergueev, Y. Z. Yue, B. Sepiol, P. Svec, L. Hu, and R. Rüffer. **Vibrational thermodynamics of $Fe_{90}Zr_7B_3$ nanocrystalline alloy from nuclear inelastic scattering**. *Phys. Rev. B*, **82**[14]:144301–, October 2010. 61

[12] B. Fultz, C. C. Ahn, E. E. Alp, W. Sturhahn, and T. S. Toellner. **Phonons in Nanocrystalline ^{57}Fe**. *Phys. Rev. Lett.*, **79**[5]:937–940, August 1997. 61

[13] H. Frase, B. Fultz, and J. L. Robertson. **Phonons in nanocrystalline** Ni_3Fe. *Phys. Rev. B*, **57**[2]:898–905, Jan 1998. 61

[14] S. Mentese, J.-B. Suck, and A. J. Dianoux. **Atomic dynamics of amorphous and nanocrystalline $Ni_{80}P_{20}$**. In *Mater. Sci. Forum*, pages 671–676, Inst. fur Phys., Tech. Univ. Chemnitz, Germany, January 2000. Trans Tech Publications. 61

[15] S. Mentese, J.-B. Suck, and S. Janssen. **Atomic dynamics of rapidly quenched and annealed nanocrystalline $Ni_{89}Hf_{11}$**. In *Physica B*, **316-317**, pages 438–440, Inst. of Phys., Mater. Res. & Liquids, Technische Univ. Chemnitz, Germany, May 2002. Elsevier Nat. Sci. Found. 61

[16] A. I. Chumakov, A. Bosak, and R. Rüffer. **Contribution of acoustic modes to the density of vibrational states measured by inelastic scattering techniques**. *Phys. Rev. B*, **80**[9]:094303–, September 2009. 61, 68

[17] L. Saviot, C. H. Netting, D. B. Murray, S. Rols, A. Mermet, A.-L. Papa, C. Pighini, D. Aymes, and N. Millot. **Inelastic neutron scattering due to acoustic vibrations confined in nanoparticles: Theory and experiment**. *Phys. Rev. B*, **78**[24]:245426–, December 2008. 61

[18] D. Bersani, P. P. Lottici, and X. Z. Ding. **Phonon confinement effects in the Raman scattering by TiO_2 nanocrystals**. *Appl. Phys. Lett.*, **72**[1]:73–75, January 1998. 61

[19] M. Maczka, M. Ptak, M. Kurnatowska, L. Kępiński, P. Tomaszewski, and J. Hanuza. % bf Phonon properties of nanosized $MnWO_4$ with different size and morphology. *J. Solid State Chem.*, **184**[9]:2446–2457, 2011. 61

[20] S. Stankov, Y. Z. Yue, M. Miglierini, B. Sepiol, I. Sergueev, A. I. Chumakov, L. Hu, P. Svec, and R. Rüffer. **Vibrational Properties of Nanograins and Interfaces in Nanocrystalline Materials**. *Phys. Rev. Lett.*, **100**[23]:235503–, June 2008. 61

[21] B. Haiyang, L. Jianlin, J. Duo, and S. Jirong. **Anomalous specific heat behavior of nanocrystalline Fe at low temperatures**. *Chinese Phys. Lett.*, **12**[9]:549–552, January 1995. OK. 61

[22] L. Wang, Z. Tan, S. Meng, A. Druzhinina, R. A. Varushchenko, and G. Li. % bf Heat capacity enhancement and thermodynamic properties of nanostructured amorphous SiO_2. *J. Non-Cryst. Solids*, **296**[12]:139–142, December 2001. 61

[23] N. Petermann, N. Stein, G. Schierning, R. Theissmann, B. Stoib, M. S. Brandt, C. Hecht, C. Schulz, and H. Wiggers. **Plasma synthesis of nanostructures for improved thermoelectric properties**. *J. Phys. D: Appl. Phys.*, **44**[17]:174034, 2011. 62

[24] T. Claudio, G. Schierning, R. Theissmann, H. Wiggers, H. Schober, M. M. Koza, and R. P. Hermann. **Effects of impurities on the lattice dynamics of nanocrystalline silicon for thermoelectric application**. pages 1–10–, 2012. 62, 67, 68, 70, 74, 75

[25] A. P. Hammersley. **FIT2D: An Introduction and Overview**. ESRF Internal Report ESRF97HA02T, ESRF, 1997. 63

[26] J. Rodriguez-Carvajal. **FULLPROF V (2009)**. Technical report, Laboratoire Leon Brillouin (CEA-CNRS), France, 2009. 63

[27] A. Radulescu and A. Ioffe. % bf Neutron guide system for small-angle neutron scattering instruments of the Jlich Centre for Neutron Science at the FRM-II. *Nuclear Instruments and Methods in Physics Research Section A: Accelerators, Spectrometers, Detectors and Associated Equipment*, **586**[1]:55–58, February 2008. 63

[28] J. A. Quintanilla and W. M. Jones. **Using convex quadratic programming to model random media with Gaussian random fields**. *Phys. Rev. E*, **75**[4]:046709, Apr 2007. 63

[29] L. Canella, P. Kudějová, R. Schulze, A. Türler, and J. Jolie. % bf Characterisation and optimisation of the new Prompt Gamma-ray Activation Analysis (PGAA) facility at FRM II. *Nucl. Instrum. Methods Phys. Res., Sect. A*, **636**[1]:108 – 113, 2011. 63

[30] A. Migliori and J. L. Sarrao. *Resonant Ultrasound Spectroscopy: Applications to Physics, Materials Measurements, and Nondestructive Evaluation*. Wiley-Interscience, 1 edition, 1997. 64

[31] A. Deschamps and F. De Geuser. **On the validity of simple precipitate size measurements by small-angle scattering in metallic systems**. *J. Appl. Cryst.*, **44**:343–352, 2011. 65, 66

[32] O. Madelung, U. Rössler, and M. Schulz, editors. *Landolt-Börnstein - Group III Condensed Matter*, **41A1a**, chapter Silicon (Si) elastic moduli of Si-I. SpringerMaterials - The Landolt-Börnstein Database, 2011. 67

[33] R. P. Hermann, F. Grandjean, and G. J. Long. **Einstein oscillators that impede thermal transport**. *Am. J. Phys.*, **73**[2]:110–118, February 2005. 70

[34] C. Kittel. *Introduction to Solid State Physics*. Wiley, New York, 7th edition, 1995. 70

[35] Ashcroft and Mermin. *Solid State Physics*. Thomson Learning, Inc., 1976. 70

[36] A. J. Minnich, M. S. Dresselhaus, Z. F. Ren, and G. Chen. **Bulk nanostructured thermoelectric materials: current research and future prospects**. *Energy Environ. Sci.*, **2**:466–479, 2009. 72, 73

[37] S. K. Bux, R. G. Blair, P .K. Gogna, H. Lee, G. Chen, M. S. Dresselhaus, R. B. Kaner, and J.-P. Fleurial. **Nanostructured bulk silicon as an effective thermoelectric material**. *Adv. Funct. Mater.*, **19**[15]:2445–2452, August 2009. 72, 74, 75

[38] B. Predel. **P-Si (Phosphorus-Silicon)**. In *Landolt-Börnstein - Group IV Physical Chemistry*, **5I**, pages –. 72

[39] M. A. Green. **Intrinsic concentration, effective densities of states, and effective mass in silicon**. *J. Appl. Phys.*, **67**[6]:2944–2954, 1990. 73

[40] G. J. Snyder and E. S. Toberer. **Complex thermoelectric materials**. *Nat. Mater.*, **7**[2]:105–114, February 2008. 73

[41] G. Schierning, R. Theissmann, N. Stein, N. Petermann, A. Becker, M. Engenhorst, V. Kessler, M. Geller, A. Beckel, H. Wiggers, and R. Schmechel. **Role of oxygen on microstructure and thermoelectric properties of silicon nanocomposites**. *J. Appl. Phys.*, **110**[11]:113515–, December 2011. 73, 75

[42] C. Dames and G. Chen. *Thermoelectrics Handbook: Macro to Nano*, **1**, chapter 42, pages 42–10–42–16. CRC/Taylor & Francis, Boca Raton, FL, 2006. 75

[43] X. W. Wang, H. Lee, Y. C. Lan, G. H. Zhu, G. Joshi, D. Z. Wang, J. Yang, A. J. Muto, M. Y. Tang, J. Klatsky, S. Song, M. S. Dresselhaus, G. Chen, and Z. F. Ren. **Enhanced thermoelectric figure of merit in nanostructured n-type silicon germanium bulk alloy**. *Appl. Phys. Lett.*, **93**[19]:193121–3, November 2008. 76

[44] T.-P. Hü, S. M. Schnurre, H. Wiggers, and C. Schulz. **Gas-Phase Synthesis of Nanoscale Silicon as an Econimical Route Towards Sustainable Energy Technology**. *KONA Powder and Particle Journal*, **29**:191–207, 2011. 76

Chapter 4

Lattice Dynamics and Thermoelectric Properties of Nanocrystalline $Si_{80}Ge_{20}$

Lattice Dynamics and Thermoelectric Properties of Nanocrystalline $Si_{80}Ge_{20}$

Tania Claudio[1,2], Niklas Stein[3], Daniel G. Stroppa[4], Michael Marek Koza[5], Nils Petermann[3], Hartmut Wiggers[3], Gabi Schierning[3], Raphaël P. Hermann[1,2]

[1] *Jülich Centre for Neutron Science JCNS and Peter Grünberg Institut PGI, JARA-FIT, Forschungszentrum Jülich GmbH, D-52425 Jülich, Germany*

[2] *Faculté des Sciences, Université de Liège, B-4000 Liège, Belgium*

[3] *Faculty of Engineering and Center for NanoIntegration Duisburg-Essen (CeNIDE), University of Duisburg-Essen, D-47057, Duisburg, Germany*

[4] *Peter Grünberg Institut PGI-5, Forschungszentrum Jülich GmbH, D-52425 Jülich, Germany*

[5] *Technische Universitt München, Forschungsneutronenquelle Heinz Maier-Leibnitz (FRM II), Lichtenbergstr. 1, D-85747 Garching, Germany*

Abstract

The lattice dynamics and thermoelectric properties of sintered phosphorus-doped nanostructured silicon-germanium alloys obtained by gas-phase synthesis were studied. Measurements of the density of phonon states by inelastic neutron scattering were combined with measurements of the low-temperature heat capacity and the elastic constants. A strong influence of nanostructuration and alloying on the lattice dynamics is observed. Thermal transport measurements confirm a strong decrease of the lattice thermal conductivity. The thermoelectric figure of merit ZT with a maximum of 0.88 at 900°C 35% larger than previous measurements on similar nanostructured samples of pure silicon.

4.1 Introduction

Nanostructuration as means to improve thermoelectric materials has been the topic of many studies specially since Dresselhaus's review on the subject in 2007 [1]. An improvement of the efficiency of thermoelectric materials was predicted owing to a decrease in the thermal conductivity due to the creation of additional scattering centers for phonons at grain boundaries, leading to an increase of the dimensionless figure of merit, $ZT = S^2\sigma/\kappa$, where S is the Seebeck coefficient, σ the electrical conductivity and κ the thermal conductivity. The holy grail of thermoelectricity is a material which behaves both as a phonon-glass and an electron-crystal [2, 3, 4], i.e., a material where phonons are effectively scattered without negatively affecting the electric conductivity.

Nanocrystalline materials have significant differences in their vibrational spectra when compared with their bulk counterpart due to the large amount of grain boundaries, which gives rise to additional low energy modes. These modes are attributed to the vibrations of atoms located in the grain boundaries where the atomic structure is less defined than in the crystalline core of the material resulting in a change of the force field and softening of the force constants [5, 6, 7, 8, 9, 10, 11, 12, 13, 14, 15, 16]. The exact mechanism behind a decrease on the lattice thermal conductivity upon nanostructuration is still not fully understood. Therefore a study about the effects of nanostructuration on the lattice dynamics of thermoelectric materials is of fundamental importance.

Interesting candidates for such a study are silicon-based materials since silicon is non-toxic, inexpensive, available in industrial quantities and the know-how to process it is well established in the semiconductor industry. An addition of 12% Ge to Si is sufficient to reduce the thermal conductivity to the minimum value achievable through alloying since mass disorder is found to increase the anharmonic scattering of phonons [17]. Further reduction of the lattice thermal conductivity is expected to be achieved by nanostructuration. Top-down approaches for nanostructuration of Si-Ge alloys via mechanical alloying and milling followed by sintering resulted in samples with a competitive figure of merit at high temperatures [18, 19, 20] reaching a peak value of $ZT = 1.3$ at 900°C [18]. Moreover, nanostructured SiGe can also be produced by a bottom-up approach through a gas phase synthesis production of nanopowder followed by sintering [21].

In this work we present a detailed study of the lattice dynamics of nanostructured SiGe produced by a bottom-up process and the consequences on the thermoelectric figure of merit.

4.2 Experiments

4.2.1 Sample preparation

Nanocrystalline $Si_{80}Ge_{20}$ alloys were fabricated by a bottom-up process. Raw nanopowder was prepared by a gas phase process. The precursor gases silane (SiH_4), germane (GeH_4) and phosphine (PH_3) were decomposed quantitatively in a microwave induced plasma. Upon cooling of the gas stream in the furnace, nucleation takes place and particles grow by coalescence and sintering. The powder was collected in a filter system and sealed under inert conditions. Two powder batches with a composition of $Si_{80}Ge_{20}$ and either 1 % P or 2 % P were produced. More details about the powder synthesis can be found in Ref. [21, 22].

The powder was further processed to nanocrystalline bulk by a current assisted and pressure activated sintering technique, known as spark plasma sintering (SPS). For this, the powder was filled into a graphite crucible of 20 mm diameter and pre-compacted. A temperature-controlled SPS machine HP D 40/2 from FCT Systeme GmbH, Rauenstein, Germany, was used. The heating and cooling rate was 100 K/min and the target-temperature was either 1000 °C or 1150 °C with a hold time of 3 min at the target temperature. The applied pressure was 35 MPa in an atmosphere in the order of mbar Ar.

A total of 4 samples were produced with different nominal dopant concentration (1 % P vs. 2 % P) and sintering temperature (1000 °C vs. 1150 °C). Thermoelectric characterization was carried on all 4 samples, whereas microstructural characterization and the investigation of the lattice dynamics were carried out in detail only for the sample with 1 % P and sintered at 1150 °C.

4.2.2 Microstructural characterization

Transmission Electron Microscopy (TEM) was performed on one of the samples in a FEI-Tecnai microscope with a field-emission electron gun operating at 200 kV. TEM samples were prepared from the sintered pellet by a precision Focused Ion Beam (FIB) system using gallium ions.

X-Ray Diffraction (XRD) on a piece of the sintered pellet was measured using synchrotron radiation from the high energy station 6-ID-D of the Advanced Photon Source (APS) at Argonne National Laboratory. The X-ray wavelength was 0.124659 Å and a General Electric amorphous silicon detector was positioned at a distance of 1849 mm from the sample, a distance refined using a NIST640c Si standard. Rietveld refinement was done using the program

FULLPROF [23], and information about the average crystallite size of the nanocrystalline pellets through the Debye-Scherrer broadening of the diffraction peaks was also obtained.

4.2.3 Lattice dynamics

Time of Flight (TOF) inelastic neutron scattering was recorded on the IN6 spectrometer at the cold source of the high-flux reactor at the Institute Laue-Langevin (Grenoble, France) with an incident wavelength of 5.12 Å and an elastic energy resolution of 0.13 meV, as determined by the elastic neutron scattering on a vanadium sample. This measurements were also performed on a nanostructured Ge sample.

The Density of Phonons States (DPS) was extracted from the scattering function $S(\omega)$ in the inelastic scattering approximation and corrected for multiphonon scattering using the program LAMP [24] and was normalized to 1 between 0 and 70 meV.

The specific heat (C_p) was obtained between 2 and 300 K using the heat capacity option of a commercial Physical Property Measurement System (PPMS) from Quantum Design.

Resonant Ultrasound Spectroscopy (RUS) was applied to obtain the elastic constants C_{11} and C_{44} of the elastic tensor, which fully characterizes the elasticity in an elastically isotropic sample. A $2.5 \times 2.2 \times 1.8\,\mathrm{mm}^3$ parallelepiped-shaped sample was placed between two piezoelectric transducers used to excite the natural modes of vibration of the sample and detect its resonant response [25]. The elastic constants were then calculated from the first 30 recorded resonant frequencies.

4.2.4 Thermoelectric transport measurements

Thermoelectric transport was characterized in the temperature range from room temperature up to 1000 °C. Seebeck coefficient S and specific electrical conductivity σ were measured on a bar-shaped sample by a direct measurement technique, using a commercial system (ZEM3 by Ulvac Technologies, Inc.). The thermal diffusivity λ was measured by a laser flash method on a sample of $10\text{x}10\text{x}1\,\mathrm{mm}^3$ size, using a commercial system (LFA 457 MicroFlash by Netzsch Thermal Analysis GmbH) and the heat capacity C_p in this temperature range was obtained with the same system by employing a reference sample. The thermal conductivity was then calculated with $\kappa = \lambda \cdot C_p \cdot \rho$, using a value for the density of the pellets (ρ) obtained by the Archimedes method at room temperature.

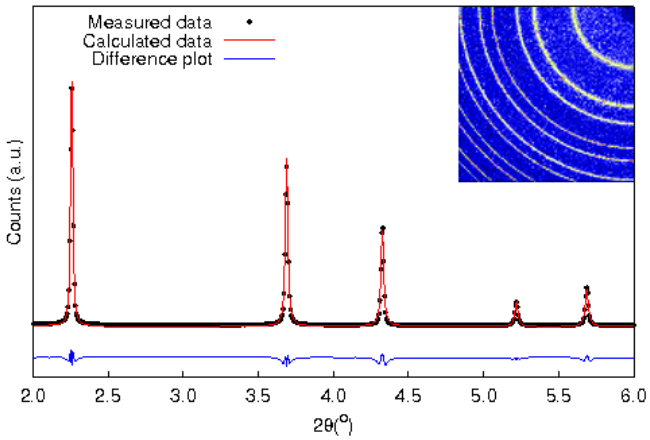

Figure 4.1: X-ray diffraction pattern of $Si_{80}Ge_{20}$ obtained at 295 K using synchrotron radiation (black dots), the refinement using Fullprof (red line), the difference plot (blue line) and a quarter of the corresponding detector image (inset).

4.3 Results and discussion

Microstructural characterization and the investigation of the lattice dynamics were carried out only for the sample with 1% P and sintered at 1150 °C, whereas thermoelectric characterization was carried on all 4 samples.

4.3.1 Microstructural characterization

The X-ray diffraction pattern reveals a perfectly alloyed sample and its refinement yielded a lattice constant of 5.4761 Å, *i.e.*, 0.83% larger than Si, corresponding precisely to the Vegard's law for solid solutions, $a_{Si_{80}Ge_{20}} = 0.8a_{Si} + 0.2a_{Ge}$, where $a_{Si} = 5.431$ Å and $a_{Ge} = 5.6512$ Å. It also yielded a strain of 0.0005% and an average crystallite size of 33 nm which is comparable only with the smallest nanocrystallite sizes observed from the TEM images. The increase in the lattice constant with respect to Si is due to the chemical disorder caused by alloying resulting in a softening of the Si structure. The strain on the material could be due to the compressibility seen by the Ge atoms or due to the defects as twins seen on the TEM images (Fig. 4.2 (b)). Furthermore, a small amount some amorphous precipitates was also observed with TEM (Fig. 4.2 (a) and (b)) and although TEM is not the method of choice to evaluate light elements, still energy-dispersive X-ray spectroscopy (EDX) of those precipitates showed a tendency for an oxide contribution.

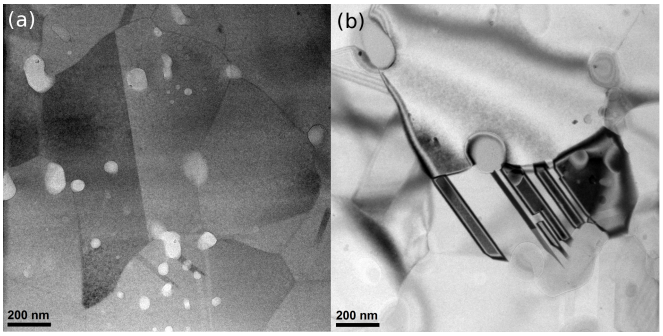

Figure 4.2: (a) TEM image of SiGe sample showing large grains (dark) and amorphous spherical precipitates (light). (b) TEM bright-field image showing defects as twins on a nanocrystal and amorphous spherical precipitates.

4.3.2 Lattice dynamics

The Density of Phonon States (DPS) of nanocrystalline $Si_{80}Ge_{20}$ obtained from inelastic neutron scattering is shown in Fig. 4.3, top. The middle plot shows the DPS of nanocrystalline Si [26] and Ge. A simple sum of the DPS of nanocrystalline Si [26] and Ge is also shown in the top plot of Fig. 4.3. This weighted sum was calculated considering weight percentage of those elements on the sample and their coherent neutron cross section (2.1633(10) and 8.42(4) barn for Si and Ge, respectively): $g_n(E) = \sum_i N_i g_i(E)\sigma_{c_i}/M_{w_i}$, where N_i is the number of atoms, g_i is the element DPS, σ_{c_i} is the coherent neutron cross section and M_{w_i} is the molecular weight. Comparison of this sum with experimental data reveals that both spectra have the same cut-off energy, but many modes of the $Si_{80}Ge_{20}$ sample are not reproduced in this simple approach, since the Si-Ge bonds are not being considered. This is particularly seen in an excess contribution at 50 meV which is due only to Si-Ge vibrations as previously observed with Raman spectroscopy for a 20% of Ge content on Si [27].

Another less simplistic approach to model the data is to consider the acoustic and optical part separately. The acoustic part was modeled by scaling both spectra (n-Si and n-Ge) to an effective elastic medium average of $Si_{80}Ge_{20}$, whereas the optical part was modeled by considering the same electronic structure and applying a homology relation [28] with which the mode energy difference can be calculated as $E_{Si_{80}Ge_{20}}/E_{Si} = \sqrt{(M_{Si}a_{Si}^2)/(M_{Si_{80}Ge_{20}}a_{Si_{80}Ge_{20}}^2)}$. The same relation was used for Ge and the resulting scale factors are $E_{Si_{80}Ge_{20}}/E_{Si} = 0.87$ and $E_{Si_{80}Ge_{20}}/E_{Ge} = 1.45$.

From the results of this calculated spectra, a significant broadening on the acoustic part of the $Si_{80}Ge_{20}$ is observed when compared to the modeled data, which reflects the chemical

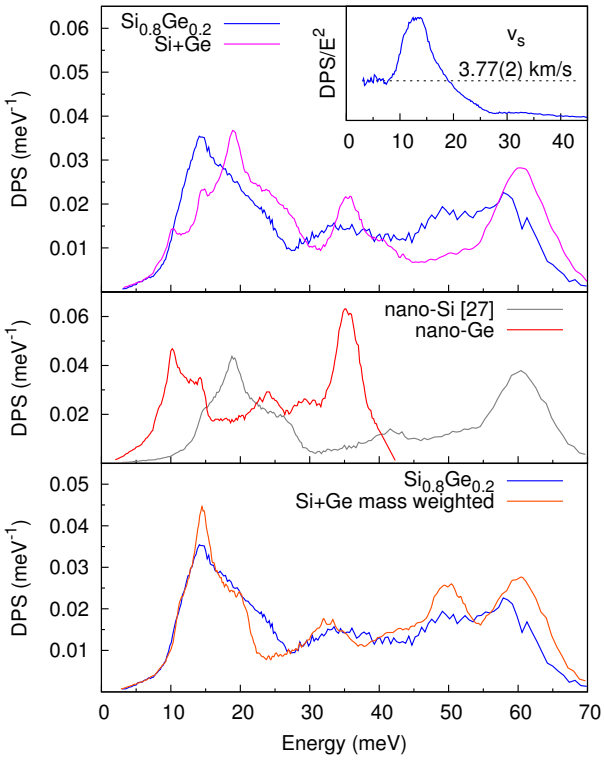

Figure 4.3: Top: In blue, the measured Density of Phonon States (DPS) for nanocrystalline $Si_{80}Ge_{20}$, in pink, a sum of the neutron and percentage weighted DPS of nanocrystalline Si and Ge, shown separately in the middle plot. Bottom: mass weighted sum of nanocrystalline Si and Ge is compared with the DPS of nanocrystalline $Si_{80}Ge_{20}$. Inset: reduced DPS where which the speed of sound was obtained from the Debye level in the low energy limit of $g(E)/E^2$.

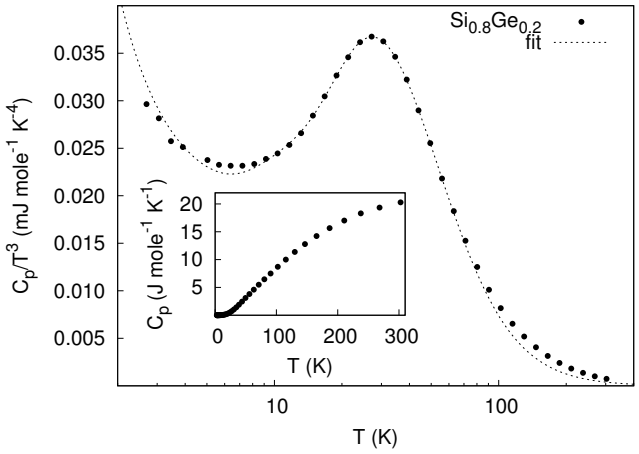

Figure 4.4: Specific heat divided by T^3 for nanocrystalline $Si_{80}Ge_{20}$ obtained with the PPMS and fit of Eq. 4.1 . Inset: specific heat. (error bars are smaller than the symbol size)

disorder caused by alloying as, also seen in the increase of the lattice constant measured by XRD. In the same way, this expansion of the lattice will also be reflected on the optical modes, causing a softening of Si modes, whereas Ge modes stiffens.

The speed of sound was extracted from the reduced DPS (inset fig. 4.3) using the low energy limit of $g(E)/E^2$ [9] with $v_s^3 = \frac{E^2}{2\pi^2 N_V \hbar^3 g(E)}$, where N_V is the number of atoms per unit volume ($N_V = \rho N_a/M_w$ with ρ being the density, N_a the Avogadro number and M_w the molecular weight). The speed of sound obtained by this method is 3.77(2) km/s, *i.e.* nanostructuration combined with a 20% substitution of Si atoms by Ge atoms causes a decrease of $\approx$44% in the speed of sound of bulk Si (6.73(5) km/s) obtained with the same method [26].

The specific heat divided by T^3 of the nanocrystalline $Si_{80}Ge_{20}$ measured between 2 and 300 K is shown in Fig. 4.4 and the C_p is shown on the inset. An increase in C_p/T^3 for $T \to 0$ is due to an electronic contribution from the high carrier concentration, as there is no freeze-out of the charge carriers.

C_p was then modeled at low temperature by considering this electronic contribution (γT) and a lattice contribution (βT^3): $C_p(T) = \gamma T + \beta T^3$. For a more precise analysis of the T^3 lattice contribution β was expanded using the Debye model and two Einstein terms to describe the excess C_p at approximately 45 K [26]:

$$C_p(T) = \gamma T + dC_D(T) + e_1 C_{E_1}(T) + e_2 C_{E_2}(T) \tag{4.1}$$

$$C_D(T) = 9Nk_B \left(T/\Theta_D\right)^3 \int_0^{\Theta_D/T} \frac{e^x x^4}{\left(e^x - 1\right)^2} \mathrm{d}x \tag{4.2}$$

$$C_E(T) = 3Nk_B \frac{e^{\Theta_E/T} \left(\frac{\Theta_E}{T}\right)^2}{(e^{\Theta_E/T} - 1)^2} \tag{4.3}$$

The fit was carried out below 90 K, and the values obtained for Debye and Einstein temperatures, as well as their prefactors are summarized in table 4.1. The Debye temperature (Θ_D^{HT}) obtained with the fit on this temperature range deviates slightly from the one obtained from the low temperature Debye plateau (Θ_D^{LT}), and therefore only the last one was used for the calculation of the speed of sound [29]: $v_s = \frac{k_B \Theta_D^{LT}}{\hbar (6\pi^2 N_V)^{1/3}}$.

Table 4.1: Einstein and Debye temperatures and pre-factors obtained from the heat capacity fit for the nanocrystalline $Si_{80}Ge_{20}$ compared with previously obtained values for Si and Ge.

	d (J/mol-K)	$\Theta_{D^{HT}}$ (K)	e_1 (J/mol-K)	Θ_{E_1} (K)	C_{11} (GPa)	C_{12} (GPa)	C_{44} (GPa)	v_s (km/s) RUS	DPS	C_p, Θ_D^{LT}
$Si_{80}Ge_{20}$	8.8(2)	329(10)	2.2(3)	146(5)	151.4		55.3	4.80	3.77(2)	4.2(2)
Bulk Si	11.4(3)	501(17)	3.8(3)	188(2)	160.1	57.8	80.0 [30]	5.92	6.73	5.70(5)
Bulk Ge	10.3(3)	271(8)	4.0(2)	104(1)	129.8	48.8	67.3 [31]	3.55	-	3.47(8)

The electronic contribution was $\gamma = 0.09(1)\,\mathrm{mJ\,mol^{-1}\,K^{-2}}$, whereas the values obtained on the specific heat of metals range between 0.6 and $2.5\,\mathrm{mJ\,mol^{-1}\,K^{-2}}$[29]. Therefore, although γ is not in the range of metals, it still reveals a significant presence of electronic contribution.

The second Einstein term was added to the model because of a broadening of the excess C_p at approximately 45 K as the broadening observed on the DPS at the acoustic region peaking at 15 meV due to the acoustic contribution of Si and Ge. It corresponds to a small contribution, with prefactor $e_2 = 0.08(6)$ J/mol-K and an Einstein temperature $\Theta_{E_2} = 68(12)$ K.

The elastic constants C_{11} and C_{44} were obtained with RUS. In an isotropic medium those two elastic constants fully characterize the elasticity, where the bulk modulus $B = C_{11}$ and the shear modulus $G = C_{44}$, but in a single-crystal $B = \frac{C_{11}+2C_{12}}{3}$ and G can be calculated with the Hershey-Kröner-Eshelby averaging method [1]. The speed of sound was then calculated: $\frac{3}{v_s^3} = \frac{1}{v_{long}^3} + \frac{2}{v_{trans}^3}$, where $v_{trans} = \sqrt{G/\rho}$, $v_{long} = \sqrt{B/\rho}$ for the polycrystals, and $v_{long} = \sqrt{\frac{B+\frac{4}{3}G}{\rho}}$ for single-crystals, and the values obtained are summarized in Table 4.1. The values of speed of sound obtained by this method are in good agreement with the values obtained from the low temperature Debye plateau of the heat capacity, and shows that nanostructuration combined with alloying of Si with 20% of Ge atoms results in a decrease between 21 and 26% in the speed of sound of bulk Si. Although this value differs from the values obtained from the DPS, both show such a decrease.

Furthermore, from all three materials, the $Si_{80}Ge_{20}$ presented the smallest C_{44}, contrary to the theory that the elastic constants of the $Si_{80}Ge_{20}$ alloy should be in between the elastic constants from Si and Ge, $C_{Si_{80}Ge_{20}} = C_{Si} - 0.2C_{Ge}$ [33]. This indicates that nanostructuration has a strong influence on the resistance to shear deformation of the material.

4.3.3 Thermoelectric transport measurements

The thermoelectric transport characterization of the four $Si_{80}Ge_{20}$ samples (dopant concentration 1%P vs. 2%P and sintering temperature 1000°C vs. 1150°C) is shown in Fig. 4.5. Accordingly, the higher sintering temperature leads to significantly higher electrical conductivity (800 S/cm and 1000 S/cm at room temperature) than the lower sintering temperature

[1] Hershey-Kröner-Eshelby described by Eshelby [32]:
$G^3 + \alpha G^2 + \beta G + \gamma = 0$, where
$\alpha = \frac{5C_{11}+4C_{12}}{8}$, $\beta = -\frac{C_{44}(7C_{11}-4C_{12})}{8}$, $\gamma = -\frac{C_{44}(C_{11}-C_{12})(C_{11}+2C_{12})}{8}$.

(150 S/cm and 300 S/cm at room temperature), regardless of the nominal doping concentration, due to a better electrical activation of the dopant atoms resulting in a higher charge carrier concentration, better crystallinity as a consequence of larger crystallite sizes, and better healing of defects when compared to a lower sintering temperature. All this factors combined lead to a higher electrical mobility. Consequently, the power factor of samples sintered at higher temperatures is best and as high as 3 mW/m-K^2 at elevated temperatures.

The improved crystalline quality of the samples sintered at higher temperatures reflects in a higher thermal conductivity than compared to the samples sintered at lower temperature. The thermal conductivity is only a function of the sintering temperature, whereas the dopant concentration does not play a role in thermal conductivity lowering. Sintering at 1150°C results in a thermal conductivity of around 3.5 W/K-m, whereas 1000°C sintering produces pellets with around 2 W/K-m.

The phononic contribution to the thermal conductivity (κ_{ph}) was obtained by subtracting the electronic contribution ($\kappa_{el} = \sigma LT$) from the total thermal conductivity, where $L = 2.44 \times 10^{-8}\,\mathrm{W\,\Omega\,K^{-2}}$ is the Lorenz number, T is the temperature and σ is the electronic conductivity. In this case all samples presented different values of phononic contribution, due to the difference in σ, where the lower value was for the sample prepared with 1%P at 1000°C and the higher value was for the sample prepared with 2%P at 1150°C.

As a consequence of the opposing trends in electronic and phononic properties, the overall figure of merit of the four samples is largely unaffected by the variations of raw powder composition and sintering conditions. The best ZT achieved was 0.88 at 900°C, and the variations between the different samples are marginal.

In order to emphasis the influence of the sintering temperature on the crystalline quality of the lattice, the electrical conductivity of the samples is represented versus the thermal conductivity in order to gain information about the lattice thermal conductivity, whereas the literature value of the Lorenz number was taken as slope, see Fig. 4.6. The sets of samples mainly differ in their lattice contribution to the thermal conductivity, whereas the additional dopant atoms do not further reduce the lattice thermal conductivity.

Furthermore, a comparison of the obtained thermoelectric transport data with literature values of samples exhibiting a comparable chemical composition is shown in table 4.2. The samples studied by Wang *et. al.* [18] had slightly smaller nanocrystallite sizes (22 nm compared to 33 nm for this work), and the thermal conductivity was also slightly smaller for the samples studied during this work. The charge carrier concentration and mobility is double of the value achieved in this work for Wang *et. al.* [18], leading to a very high

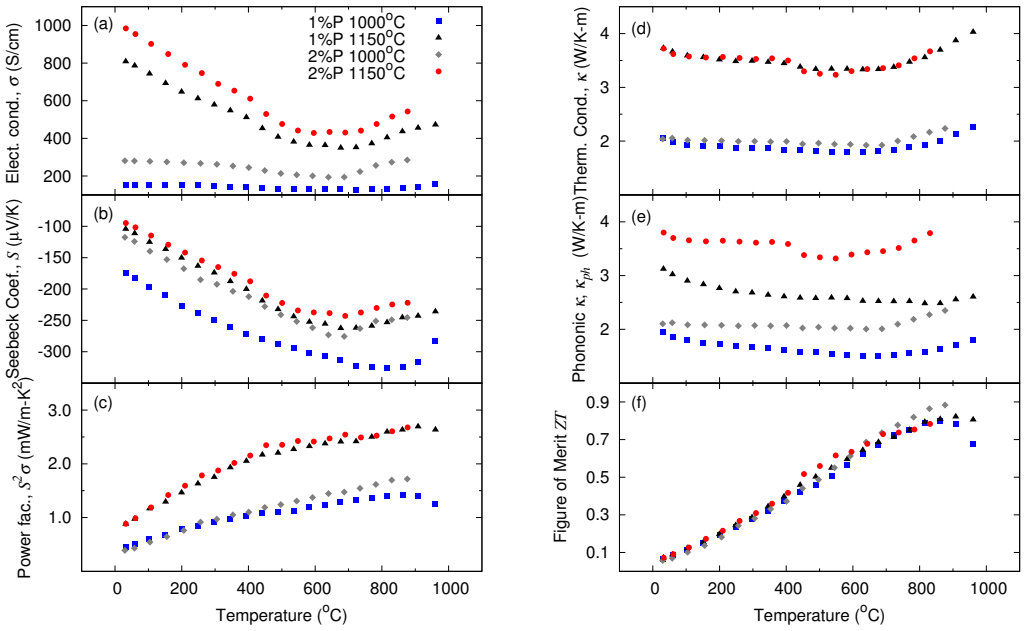

Figure 4.5: Thermoelectric characterization of 4 $Si_{80}Ge_{20}$ samples differing in dopant concentration (1% P vs. 2% P) and sintering temperature (1000°C vs. 1150°C). While higher sintering temperature leads to a significantly better electrical conductivity and therewith power factor, also thermal conductivity increases accordingly. Overall, the figure of merit is quite insensitive towards a variation of sintering temperature and doping concentration, with best $ZT = 0.88$ at 900°C.

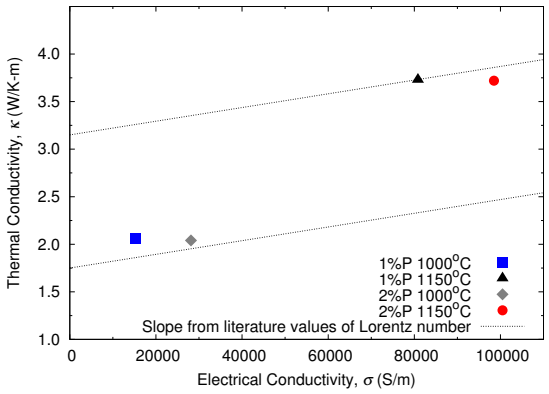

Figure 4.6: Thermal conductivity *vs.* electrical conductivity values for all for samples at room temperature and the slope from literature values of the Lorentz number.

electrical conductivity. Since the density of the present samples is not very high, the mobility is not as high as it could be, resulting in not ideal values for the electrical conductivity and the carrier mobility is also not optimal, resulting in a slightly lower Seebeck coefficient. This reflects the main difference in the ZT values. Overall, a reduction of up to 50% compared to bulk samples [34] was achieved but it was followed by a decrease in the carrier mobility leading to a lower electrical conductivity.

Table 4.2: Physical properties of the $Si_{80}Ge_{20}$ samples compared with previously published values.

	Dismukes 1964 [34]	Vining 1991 [35]	Wang 2008 [18]	this work
Stoichiometry	$Si_{80}Ge_{20}$	$Si_{80}Ge_{20}$	$Si_{80}Ge_{20}$	$Si_{80}Ge_{20}$
Density (g/cm^3)	3.01 (100%)	2.96 (98.3 %)	no information	2.88 (95.7%)
Nanocrystallite size (nm)	no information	1800	22	≈ 33
Carrier density (10^{20} cm^{-3})	1.4	1.25	2.2	1.2
Carrier mobitiy @ RT (cm^2/Vs)	55	43.8	23	15
Seebeck coeff. @ RT ($\mu V/K$)	-130	-116	-120	-118
Electrical cond. @ RT (S/cm)	850	870	1000	285
Thermal cond. @ RT (W/mK)	4-5	3.97	2.5	2.23
ZT Maximum	0.7 @ 1000 K	1.04 @ 1200 K	1.3 @ 1200 K	0.88 @ 1150 K

4.4 Conclusions

Measurements of the density of phonon states with inelastic neutron scattering, of the heat capacity and of the elastic constants with resonant ultrasound spectroscopy offer a deep understanding of the effects of nanostructuration and alloying on the lattice dynamics of nanocrystalline $Si_{80}Ge_{20}$, showing nanostructuration combined with a 20% substitution of Si atoms by Ge atoms causes a significant reduction on the speed of sound, resulting in a 50% reduction of the thermal conductivity when compared with the bulk material.

Furthermore, nanostructuration and alloying also have a strong positive impact on the thermoelectric properties. The peak ZT of 0.88 is higher than results on similar samples of pure silicon with a ZT of 0.57 at 973°C [36]. The reported maximum ZT of 1.3 for nanostructured Si-Ge alloys was not achieved. A better control of the impurities [26, 36] as well as optimized doping level and sintering conditions promise to give better results in the future.

4.5 Acknowledgments

The Institute Laue-Langevin (ILL - Grenoble, France) and the Advanced Photon Source (APS) at Argonne National Laboratory are acknowledged for neutron and synchrotron radiation beam time respectively. The Helmholtz Gemeinschaft Deutscher Forschungszentren is acknowledged for funding VH NG-407 “Lattice dynamics in emerging functional materials”. D. Meertens is kindly acknowledged for TEM sample preparation, D. Weber for scientific input and K. Friese for input on XRD refinement.

References

[1] M. S. Dresselhaus, G. Chen, M. Y. Tang, R. G. Yang, H. Lee, D. Z. Wang, Z. F. Ren, J. P. Fleurial, and P. Gogna. **New Directions for Low-Dimensional Thermoelectric Materials**. *Adv. Mater.*, **19**[8]:1043–1053, 2007. 84

[2] G. S. Nolas, G. A. Slack, and S. B. Schujman. % bf Chapter 6 Semiconductor clathrates: A phonon glass electron crystal material with potential for thermoelectric applications. In Terry M. Tritt, editor, *Recent Trends in Thermoelectric Materials Research I*, **69**, pages 255–300. Elsevier, 2001. 84

[3] G. J. Snyder, M. Christensen, E. Nishibori, T. Caillat, and B. B. Iversen. **Disordered zinc in Zn_4Sb_3 with phonon-glass and electron-crystal thermoelectric properties**. *Nat. Mater.*, **3**[7]:458–463, July 2004. 84

[4] G. Min and D.M. Rowe. **A serious limitation to the phonon glass electron crystal (PGEC) approach to improved thermoelectric materials**. *J. Mater. Sci. Lett.*, **18**[16]:1305–1306, 1999. 84

[5] B. Fultz, C. C. Ahn, E. E. Alp, W. Sturhahn, and T. S. Toellner. **Phonons in Nanocrystalline ^{57}Fe**. *Phys. Rev. Lett.*, **79**[5]:937–940, August 1997. 84

[6] H. Frase, B. Fultz, and J. L. Robertson. **Phonons in nanocrystalline** Ni_3Fe. *Phys. Rev. B*, **57**[2]:898–905, Jan 1998. 84

[7] S. Mentese, J.-B. Suck, and S. Janssen. **Atomic dynamics of rapidly quenched and annealed nanocrystalline $Ni_{89}Hf_{11}$**. In *Physica B*, **316-317**, pages 438–440, Inst. of Phys., Mater. Res. & Liquids, Technische Univ. Chemnitz, Germany, May 2002. Elsevier Nat. Sci. Found. 84

[8] S. Stankov, Y. Z. Yue, M. Miglierini, B. Sepiol, I. Sergueev, A. I. Chumakov, L. Hu, P. Svec, and R. Rüffer. **Vibrational Properties of Nanograins and Interfaces in Nanocrystalline Materials**. *Phys. Rev. Lett.*, **100**[23]:235503–, June 2008. 84

[9] A. I. Chumakov, A. Bosak, and R. Rüffer. **Contribution of acoustic modes to the density of vibrational states measured by inelastic scattering techniques**. *Phys. Rev. B*, **80**[9]:094303–, September 2009. 84, 90

[10] S.R. Phillpot, J. Wang, D. Wolf, and H. Gleiter. **Computer simulation of the structure and dynamical properties of grain boundaries in a nanocrystalline model material**. In *Materials Science & Engineering A (Structural Materials: Properties, Microstructure and Processing)*, **A204**, pages 76–82, Div. of Mater. Sci., Argonne Nat. Lab., IL, USA, December 1995. Elsevier Office of Naval Res. Office of Naval Res. 84

[11] D. Wolf, J. Wang, S.R. Phillpot, and H. Gleiter. **On the thermodynamic relationship between nanocrystalline materials and glasses**. *Phys. Lett. A*, **205**[4]:274–280, September 1995. 84

[12] R. Singh, S. Prakash, R. Meyer, and P. Entel. **Phonon density of states in nanocrystalline ^{57}Fe**. *Pramana J. Phys.*, **60**[3]:547–556, March 2003. 84

[13] J. Wang, D. Wolf, S. R. Phillpot, and H. Gleiter. **Phonon-induced anomalous specific heat of a model nanocrystal by computer simulation**. In *Nanostruct. Mater.*, **6**, pages 747–750, Div. of Mater. Sci., Argonne Nat. Lab., IL, USA, January 1995. 84

[14] R. Singh and S. Prakash. **Phonons in nanocrystalline fcc nickel**. *Surf. Sci.*, **532-535**:272–275, June 2003. 84

[15] R. Singh and S. Prakash. **Vibrational properties of nanocrystalline fcc Ni_3Fe**. *Indian J. Phys.*, **77A**[3]:243–246, May 2003. 84

[16] S. Stankov, M. Miglierini, A. I. Chumakov, I. Sergueev, Y. Z. Yue, B. Sepiol, P. Svec, L. Hu, and R. Rüffer. **Vibrational thermodynamics of $Fe_{90}Zr_7B_3$ nanocrystalline alloy from nuclear inelastic scattering**. *Phys. Rev. B*, **82**[14]:144301–, October 2010. 84

[17] J. Garg, N. Bonini, B. Kozinsky, and N. Marzari. **Role of Disorder and Anharmonicity in the Thermal Conductivity of Silicon-Germanium Alloys: A First-principles Study**. *Phys. Rev. Lett.*, **106**[4]:045901–, January 2011. 84

[18] X. W. Wang, H. Lee, Y. C. Lan, G. H. Zhu, G. Joshi, D. Z. Wang, J. Yang, A. J. Muto, M. Y. Tang, J. Klatsky, S. Song, M. S. Dresselhaus, G. Chen, and Z. F. Ren. **Enhanced thermoelectric figure of merit in nanostructured n-type silicon germanium bulk alloy**. *Appl. Phys. Lett.*, **93**[19]:193121–3, November 2008. 84, 94, 97

[19] G. H. Zhu, H. Lee, Y. C. Lan, X. W. Wang, G. Joshi, D. Z. Wang, J. Yang, D. Vashaee, H. Guilbert, A. Pillitteri, M. S. Dresselhaus, G. Chen, and Z. F. Ren. **Increased Phonon Scattering by Nanograins and Point Defects in Nanostructured Silicon with a Low Concentration of Germanium**. *Phys. Rev. Lett.*, **102**[19]:196803, May 2009. 84

[20] L. Tayebi, Z. Zamanipour, M. Mozafari, P. Norouzzadeh, J.S. Krasinski, K.F. Ede, and D. Vashaee. **Thermal and Thermoelectric Properties of Nanostructured versus Crystalline SiGe**. In *2012 IEEE Green Technologies Conference*, pages –, Helmerich Advanced Technology Research Center, Tulsa, OK, USA, January 2012. IEEE IEEE Tulsa Sect. IEEE Tulsa Sect. 84

[21] N. Stein, N. Petermann, R. Theissmann, G. Schierning, R. Schmechel, and H. Wiggers. **Artificially nanostructured n-type SiGe bulk thermoelectrics through plasma enhanced growth of alloy nanoparticles from the gas phase**. *Journal of Materials Research*, **26**:1872–1878, 2011. 84, 85

[22] N. Petermann, N. Stein, G. Schierning, R. Theissmann, B. Stoib, M. S. Brandt, C. Hecht, C. Schulz, and H. Wiggers. **Plasma synthesis of nanostructures for improved thermoelectric properties**. *J. Phys. D: Appl. Phys.*, **44**[17]:174034, 2011. 85

[23] J. Rodriguez-Carvajal. **FULLPROF V (2009)**. Technical report, Laboratoire Leon Brillouin (CEA-CNRS), France, 2009. 86

[24] *LAMP, the Large Array Manipulation Program.* 86

[25] A. Migliori and J. L. Sarrao. *Resonant Ultrasound Spectroscopy: Applications to Physics, Materials Measurements, and Nondestructive Evaluation.* Wiley-Interscience, 1 edition, 1997. 86

[26] T. Claudio, G. Schierning, R. Theissmann, H. Wiggers, H. Schober, M. M. Koza, and R. P. Hermann. **Effects of impurities on the lattice dynamics of nanocrystalline silicon for thermoelectric application**. pages 1–10–, 2012. 88, 90, 98

[27] M. I. Alonso and K. Winer. **Raman spectra of c-Si$_{1-x}$Ge$_x$ alloys**. *Phys. Rev. B*, **39**[14]:10056–10062, May 1989. 88

[28] H. R. Schober and W. Petry. *Lattice Vibrations.* Wiley-VCH Verlag GmbH, 2006. 88

[29] C. Kittel. *Introduction to Solid State Physics.* Wiley, New York, 7th edition, 1995. 91, 93

[30] O. Madelung, U. Rössler, and M. Schulz, editors. *Landolt-Börnstein - Group III Condensed Matter*, **41A1a**, chapter Silicon (Si) elastic moduli of Si-I. SpringerMaterials - The Landolt-Börnstein Database, 2011. 92

[31] W. L. Bond, W. P. Mason, H. J. McSkimin, K. M. Olsen, and G. K. Teal. **The Elastic Constants of Germanium Single Crystals**. *Phys. Rev.*, **78**[2]:176–176, April 1950. 92

[32] J. D. Eshelby. *Progress in Solid Mechanics*, **2**, page 130. North Holland Publ. Co., Amsterdam, 1961. 93

[33] Friedrich Schäffler. **High-mobility Si and Ge structures**. *Semicond. Sci. Technol.*, **12**[12]:1515, 1997. 93

[34] J. P. Dismukes, L. Ekstrom, E. F. Stigmeier, I. Kudman, and D. S. Beers. **Thermal and electrical properties of heavily doped Ge-Si alloys up to 1300 K**. *J. Appl. Phys.*, **35**[10]:2899–2907, 1964. 96, 97

[35] C. B. Vining, W. Laskow, J. O. Hanson, and R. R. Van der Beek. **Thermoelectric properties of pressure-sintered Si0.8Ge0.2 thermoelectric alloys**. *J. Appl. Phys.*, **69**[8]:4333–4340, 1991. 97

[36] T. Claudio, N. Stein, D. G. Stroppa, B. Klobes, M. M. Koza, P. Kudejova, N. Petermann, H. Wiggers, G. Schierning, and R. P. Hermann. **Nanocrystalline Silicon: Lattice Dynamics and Enhanced Thermoelectric Properties**. *Energy & Environmental Science*, Submitted. 98

Chapter 5

Enhanced Debye Level in nano $Zn_{1+x}Sb$, $FeSb_2$ and NiSb: Nuclear Inelastic Spectroscopy on ^{121}Sb

Enhanced Debye Level in nano $Zn_{1+x}Sb$, $FeSb_2$ and NiSb: Nuclear Inelastic Spectroscopy on ^{121}Sb

T. Claudio[1,2], D. Bessas[1,2,5], C.S. Birkel[3,4], G. Kieslich[3], M. Panthöfer[3], I. Sergueev[1,5], W. Tremel[3], R.P. Hermann[1,2]

[1] *Jülich Centre for Neutron Science JCNS and Peter Grünberg Institut PGI, JARA-FIT, Forschungszentrum Jülich GmbH, D-52425 Jülich, Germany*

[2] *Faculté des Sciences, Université de Liège, B-4000 Liège, Belgium*

[3] *Institut für Anorganische Chemie und Analytische Chemie der Johannes Gutenberg-Universität, Duesbergweg 10-14, D-55099 Mainz, Germany*

[4] *Materials Research Laboratory, University of California, Santa Barbara, USA*

[5] *European Synchrotron Radiation Facility - F-38043 Grenoble Cedex, France*

Abstract

The ^{121}Sb partial density of phonon states in nanopowder antimonides were obtained with nuclear inelastic scattering on $Zn_{1+x}Sb$, $FeSb_2$ and NiSb prepared by a wet chemistry route. The density of phonon states is compared with the bulk counterpart. An increase of the Debye level indicative of a decrease of the isothermal speed of sound is systematically observed. This observation reveals that the decrease in speed of sound observed in nanostructured thermoelectric materials is not restricted to sintered nanocomposites.

5.1 Introduction

Nanostructured materials have been the focus of several studies, since they possess significantly different properties when compared to the equivalent bulk material. Of particular interest is the effects of nanostructuration on the lattice dynamics of these materials, because it can change its thermal and electrical properties and has been intensely investigated by means of theoretical calculations [1, 2, 3, 4, 5, 6, 7, 8, 9] and observed with methods such as inelastic neutron scattering [10, 11, 12, 13, 14, 15], Raman spectroscopy [16, 17], nuclear inelastic scattering (NIS) [14, 18], and measurements of the specific heat [19, 20].

An enhancement in the density of phonon states (DPS) at low energies for nanocrystalline materials, as well as a broadening of the bands on the DPS, was previously observed [10, 11, 13, 14, 18] and calculated [1, 2, 4, 5, 8, 9, 21]. In these studies it was suggested that these additional modes can be attributed to the vibrations of atoms located in the grain boundaries, where the atomic structure is more open than in the crystalline part of the material, resulting in a change of the force field and softening of the force constants.

Although most of the theoretical and experimental studies reported so far focus on nanocrystalline bulk materials and the role of grain boundaries and changes in the interatomic distances, investigations on nanopowders also yield information about acoustic vibrational modes confined in nanoparticles in the powder form [15, 16, 17].

Transition metal antimonides such as Zn_4Sb_3[1], $FeSb_2$ and NiSb exhibit several interesting properties for diverse applications. Whereas Zn_4Sb_3 is a well known thermoelectric material [23, 24], both $FeSb_2$ and NiSb are potential anode materials in rechargeable lithium-ion batteries [25, 26] and provided that a reduction of the the thermal conductivity is achieved, they could also be valuable thermoelectric materials [27, 28].

Thermoelectric materials are a perfect example of the use of nanostructuration to improve functional properties. They are used for waste heat recovery by converting a heat flow into electricity and vice versa and its conversion efficiency is dependent on the Seebeck coefficient, electrical conductivity and inversely proportional to the thermal conductivity of the material. Therefore, it was previously suggested [29] and observed [30, 31, 32] that one way of improving the thermoelectric properties of a material is through nanostructuring, where the thermal conductivity is decreased due to the creation of scattering centres for phonons. Furthermore, reduced speed of sound and larger unit-cell volume are also known mechanisms to decrease thermal transport.

[1] The precise stoichiometry is actually $Zn_{3.95(5)}Sb_3$ [22].

Herein, we report for the first time measurements on the lattice dynamics of nanopowder antimonides done with nuclear inelastic scattering on ^{121}Sb on $Zn_{1+x}Sb$, $FeSb_2$ and NiSb prepared by a wet chemistry route, comparing it with their bulk counterpart.

5.2 Experimental

The nanopowders were prepared by a wet chemistry route based on the reaction of Sb nanoparticles with the appropriate metal precursor. In a first step, antimony nanoparticles were produced by reduction of $SbCl_3$ with lithium triethylborohydride Li[Et_3BH]. In the case of NiSb and $Zn_{1+x}Sb$, Ni and Zn nanoparticles were prepared from the corresponding chlorides and then mixed with the antimony nanoparticles. For $FeSb_2$, a dispersion of the metal precursor, cyclopentadienyl iron(II) dicarbonyl dimer was added to the suspension of Sb nanoparticles. The details of the individual reactions, *i.e.* reaction temperatures, heating rates, holding times etc., the sizes of the obtained nanoparticles (in the order of 30 nm) and the crystal structures are reported elsewhere [33, 34, 35].

^{121}Sb nuclear inelastic scattering (NIS) [36, 37] was carried out on bulk and nano $FeSb_2$ and NiSb, and on nano $Zn_{1+x}Sb$ in 16-bunch mode at the nuclear resonance station [38] ID22N of the European Synchrotron Radiation Facility in Grenoble, France. Energy scans were performed with a temperature-controlled high resolution backscattering monochromator [39]. The sample was cooled with a closed cycle cryostat to $\sim 20\,\mathrm{K}$ inside a vacuum chamber with Kapton windows for the incoming and scattered beams and the fluorescence products. The temperature of the sample was monitored by a temperature sensor in the vicinity of the sample. The precise temperature was better determined through the Bose-Einstein statistics, comparing the signal on the Stokes and anti-Stokes sides.

The corresponding partial density of phonon states for ^{121}Sb, $g(E)$, were derived from the NIS spectra using a modification of the program DOS [40] taking into account the instrumental resolution by convoluting with a Gaussian function with the same FWHM, $\sim 1.5\,\mathrm{meV}$, a slightly higher value than the measured instrumental function, $1.2\,\mathrm{meV}$, in order to avoid unphysical termination ripples in the DPS.

5.3 Results and discussion

A comparison of the nuclear inelastic scattering spectra of bulk and nano $Zn_{1+x}Sb$, NiSb and $FeSb_2$ is given in Fig. 5.1, where the instrumental function given by the elastic scattering, *i.e.*

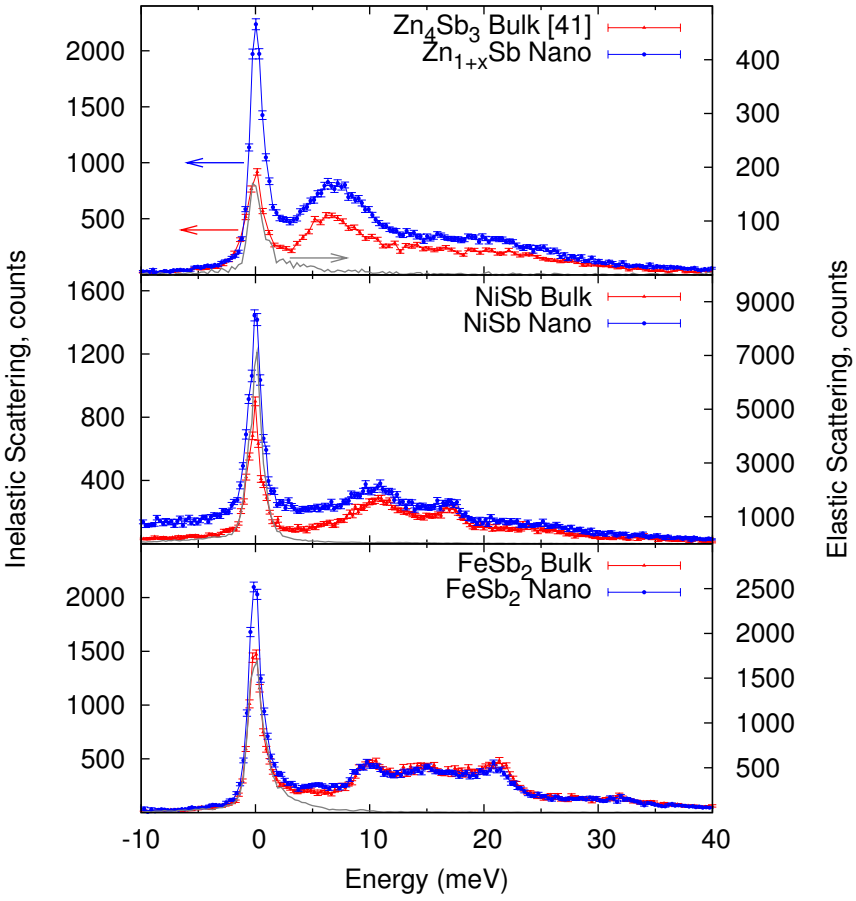

Figure 5.1: NIS spectra of nano $Zn_{1+x}Sb$, NiSb and $FeSb_2$ (blue circles) compared to the spectra of the bulk counterpart (red triangles). The elastic scattering is shown as gray line with y scale on the right side of the plots.

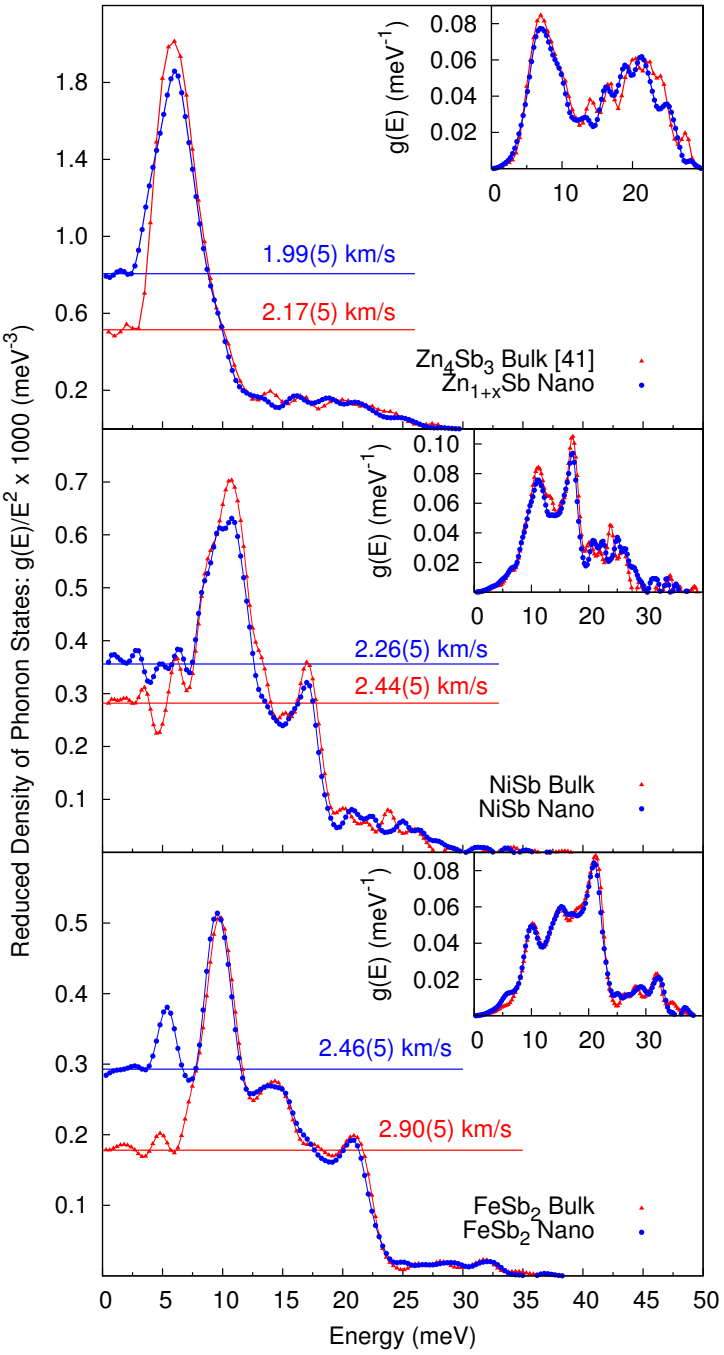

Figure 5.2: Reduced density of ^{121}Sb phonon states of nano $Zn_{1+x}Sb$, NiSb and $FeSb_2$ compared to the bulk counterpart: a decrease on the speed of sound is observed upon nanostructuration.

nuclear forward scattering (NFS), is plotted as dotted lines. The reduced partial densities of phonon states for ^{121}Sb, $g(E)/E^2$, are plotted in Fig. 5.2 and the ^{121}Sb specific density of vibrational states are plotted on the insets.

The vibrational spectra of bulk and nano $FeSb_2$ are in good agreement with each other and also with previously calculated and obtained with nuclear inelastic scattering [41] and with Raman spectroscopy [42], while the vibrational spectra of nano $Zn_{1+x}Sb$ slightly differs from the bulk Zn_4Sb_3 [43] above 12 meV probably due to its different symmetry and stoichiometry. When trying to synthesize nanoparticles of Zn_4Sb_3 with a wet chemistry approach, Birkel *et. al.* [35] obtained a new phase "$Zn_{1+x}Sb$" according to electron diffraction tomography results, with a crystal structure belonging to the space group $P\bar{1}$, whereas bulk Zn_4Sb_3 belongs to the space group $R\bar{3}c$ [22]. The vibrational spectra of bulk and nano NiSb also presents minor differences above 20 meV. Both bulk and nano NiSb were confirmed to have the same crystal structure [33, 44], $P6_3/mmc$, but with small discrepancy on the c lattice parameter, which is 0.5% larger for nano when compared to the bulk [33].

The DPS of $FeSb_2$ nanoparticles exhibits a peak at around 5 meV corresponding to acoustic phonons and is better observed in the reduced density of phonon states, $g(E)/E^2$, Fig 5.2. Such a peak was previously observed by Saviot *et al.* [15] in the inelastic neutron scattering spectra by TiO_2 nanopowder and was attributed to acoustic modes confined in the nanoparticles and compared to a Boson peak observed from glasses [14]. In a similar study carried out on nanocrystalline Si [45], such peak was also observed and attributed to a Boson peak due to amorphous SiO_2 impurities on the sample. In the present study, we have considered to attribute the low energy peak observed in nano $FeSb_2$ to a small percentage of Sb_2O_3 contribution, since the DPS of Sb_2O_3 [46] also has a peak on this energy. Modeling the data with 85 or 90% of $FeSb_2$ bulk and 15 or 10% of Sb_2O_3 would however lead not only to the presence of the peak at 5 meV, but also to a shift of the peaks at 9.5, 13.3 and 21 meV towards higher energies, which is not seen when comparing the vibrational spectra of bulk and nano $FeSb_2$. The peak at 5 meV can thus not be attributed to Sb_2O_3.

An increase of the Debye level in the low energy region (below $\sim$ 8 meV) was observed for all three nano compounds with respect to bulk in the reduced density of phonon states, Fig. 5.2, leading to a decrease of the speed of sound upon nanostructuration. The average speed of sound (v_{av}) can be extracted from the Debye level, i.e. the limit of $g(E)/E^2$ for small energies according to the relation [47]:

$$g(E) = \frac{m_r}{\langle m \rangle} \frac{V}{2\pi^2 \hbar^3 v_{av}^3} E^2, \tag{5.1}$$

where m_r is the mass of the resonant ^{121}Sb atom, $\langle m \rangle$ is the mean atomic mass and V is the volume per Sb atom and can be obtained by taking into account the density of the materials obtained from the lattice parameters published previously [33, 34, 35].

The high energy optical phonons remain unaffected from nanostructuration, *i.e.* no phonon broadening or phonon stiffening is observed.

In a simple Debye model the thermal conductivity is expressed as the product of the specific heat, the average phonon relaxation times, and the square of the speed of sound [48]. The observed increase in the Debye level corresponding to a reduction in the speed of sound by $\sim$18% for the case of $FeSb_2$ is thus expected to significantly reduce the thermal transport, by $\sim$40%, even under the assumption that there is no change in the average phonon relaxation time. The same applies to $Zn_{1+x}Sb$ and NiSb with reductions on the speed of sound of $\sim$9% and $\sim$8%, respectively. Thus an enhancement of the thermoelectric figure of merit is expected, provided that the nanoparticles can be sintered while preserving their nanostructure.

Next to the scattering on the grain boundaries such a reduction in the speed of sound thus provides a second mechanism to lower the thermal transport in nanostructured materials, and this mechanism should be systematically investigated in future research on thermal transport in nanomaterials. The origin of the reduced speed of sound itself needs to be clarified, as it could be related either to the presence of grain boundaries and/or surface effects or due to the reduced dimensions. A further effect from phonon lifetime modification was not observed herein, either because of our limited 1.2 meV resolution or because it is not significant in these range of nanoparticles sizes ($\sim$30 nm).

5.4 Conclusions

An excess of low energy phonon modes upon nanosctructuration was previously predicted [1, 2, 4, 5, 8, 9, 21] and observed [10, 11, 13, 14, 18] for the case of bulk materials due to a large amount of grain boundaries. Such an excess is observed in the present study of ^{121}Sb nuclear inelastic scattering (NIS) in nanoparticles of $Zn_{1+x}Sb$, $FeSb_2$ and NiSb prepared by a wet chemistry route although the broadening of the bands on the DPS was not observed. This excess is related to an increase of the Debye level and consequently to a decrease in the speed of sound which is suggested to also lead to a decrease of the thermal conductivity. Such a study indicates that not only grain-boundaries can affect the lattice thermal conductivity

of a material, but also a reduction on the speed of sound can be observed in the nanoparticles themselves.

5.5 Acknowledgments

The European Synchrotron Radiation Facility (ESRF - Grenoble, France) is acknowledged for synchrotron radiation beam time. The Helmholtz-University Young Investigator Group "Lattices Dynamics in Emerging Functional Materials" is acknowledged for the support of this study and W.T. acknowledges support from the DFG priority program SPP1386 "Nanostructured Thermoelectrics".

References

[1] D. Wolf, J. Wang, S.R. Phillpot, and H. Gleiter. **On the thermodynamic relationship between nanocrystalline materials and glasses**. *Phys. Lett. A*, **205**[4]:274–280, September 1995. 105, 110

[2] S.R. Phillpot, J. Wang, D. Wolf, and H. Gleiter. **Computer simulation of the structure and dynamical properties of grain boundaries in a nanocrystalline model material**. In *Materials Science & Engineering A (Structural Materials: Properties, Microstructure and Processing)*, **A204**, pages 76–82, Div. of Mater. Sci., Argonne Nat. Lab., IL, USA, December 1995. Elsevier Office of Naval Res. Office of Naval Res. 105, 110

[3] M.-S. Jeng, R. Yang, D. Song, and G. Chen. **Modeling the Thermal Conductivity and Phonon Transport in Nanoparticle Composites Using Monte Carlo Simulation**. *J. Heat Transfer*, **130**[4], April 2008. 105

[4] R. Singh and S. Prakash. **Vibrational properties of nanocrystalline fcc Ni_3Fe**. *Indian J. Phys.*, **77A**[3]:243–246, May 2003. 105, 110

[5] R. Singh, S. Prakash, R. Meyer, and P. Entel. **Phonon density of states in nanocrystalline ^{57}Fe**. *Pramana J. Phys.*, **60**[3]:547–556, March 2003. 105, 110

[6] A. I. Potapov, I. S. Pavlov, and S. A. Lisina. **Acoustic identification of nanocrystalline media**. *J. Sound Vib.*, **322**[3]:564–580, May 2009. 105

[7] X. Hui, L. X. mei, and Z. G. Xiong. **Study on the thermal properties of one-dimensional nanocrystalline**. *Electronic Components & Materials*, **21**[10]:10–12, October 2002. 105

[8] J. Wang, D. Wolf, S. R. Phillpot, and H. Gleiter. **Phonon-induced anomalous specific heat of a model nanocrystal by computer simulation**. In *Nanostruct. Mater.*, **6**, pages 747–750, Div. of Mater. Sci., Argonne Nat. Lab., IL, USA, January 1995. 105, 110

[9] S. Stankov, M. Miglierini, A. I. Chumakov, I. Sergueev, Y. Z. Yue, B. Sepiol, P. Svec, L. Hu, and R. Rüffer. **Vibrational thermodynamics of $Fe_{90}Zr_7B_3$ nanocrystalline alloy from nuclear inelastic scattering**. *Phys. Rev. B*, **82**[14]:144301–, October 2010. 105, 110

[10] B. Fultz, C. C. Ahn, E. E. Alp, W. Sturhahn, and T. S. Toellner. **Phonons in Nanocrystalline ^{57}Fe**. *Phys. Rev. Lett.*, **79**[5]:937–940, August 1997. 105, 110

[11] H. Frase, B. Fultz, and J. L. Robertson. **Phonons in nanocrystalline** Ni_3Fe. *Phys. Rev. B*, **57**[2]:898–905, Jan 1998. 105, 110

[12] S. Mentese, J.-B. Suck, and A. J. Dianoux. **Atomic dynamics of amorphous and nanocrystalline** $\mathbf{Ni_{80}P_{20}}$. In *Mater. Sci. Forum*, pages 671–676, Inst. fur Phys., Tech. Univ. Chemnitz, Germany, January 2000. Trans Tech Publications. 105

[13] S. Mentese, J.-B. Suck, and S. Janssen. **Atomic dynamics of rapidly quenched and annealed nanocrystalline** $\mathbf{Ni_{89}Hf_{11}}$. In *Physica B*, **316-317**, pages 438–440, Inst. of Phys., Mater. Res. & Liquids, Technische Univ. Chemnitz, Germany, May 2002. Elsevier Nat. Sci. Found. 105, 110

[14] A. I. Chumakov, A. Bosak, and R. Rüffer. **Contribution of acoustic modes to the density of vibrational states measured by inelastic scattering techniques**. *Phys. Rev. B*, **80**[9]:094303–, September 2009. 105, 109, 110

[15] L. Saviot, C. H. Netting, D. B. Murray, S. Rols, A. Mermet, A.-L. Papa, C. Pighini, D. Aymes, and N. Millot. **Inelastic neutron scattering due to acoustic vibrations confined in nanoparticles: Theory and experiment**. *Phys. Rev. B*, **78**[24]:245426–, December 2008. 105, 109

[16] D. Bersani, P. P. Lottici, and X. Z. Ding. **Phonon confinement effects in the Raman scattering by** $\mathbf{TiO_2}$ **nanocrystals**. *Appl. Phys. Lett.*, **72**[1]:73–75, January 1998. 105

[17] M. Maczka, M. Ptak, M. Kurnatowska, L. Kępiński, P. Tomaszewski, and J. Hanuza. % bf Phonon properties of nanosized $MnWO_4$ with different size and morphology. *J. Solid State Chem.*, **184**[9]:2446–2457, 2011. 105

[18] S. Stankov, Y. Z. Yue, M. Miglierini, B. Sepiol, I. Sergueev, A. I. Chumakov, L. Hu, P. Svec, and R. Rüffer. **Vibrational Properties of Nanograins and Interfaces in Nanocrystalline Materials**. *Phys. Rev. Lett.*, **100**[23]:235503–, June 2008. 105, 110

[19] B. Haiyang, L. Jianlin, J. Duo, and S. Jirong. **Anomalous specific heat behavior of nanocrystalline Fe at low temperatures**. *Chinese Phys. Lett.*, **12**[9]:549–552, January 1995. OK. 105

[20] L. Wang, Z. Tan, S. Meng, A. Druzhinina, R. A. Varushchenko, and G. Li. % bf Heat capacity enhancement and thermodynamic properties of nanostructured amorphous SiO_2. *J. Non-Cryst. Solids*, **296**[12]:139–142, December 2001. 105

[21] R. Singh and S. Prakash. **Phonons in nanocrystalline fcc nickel**. *Surf. Sci.*, **532-535**:272–275, June 2003. 105, 110

[22] G. J. Snyder, M. Christensen, E. Nishibori, T. Caillat, and B. B. Iversen. **Disordered zinc in** $\mathbf{Zn_4Sb_3}$ **with phonon-glass and electron-crystal thermoelectric properties**. *Nat. Mater.*, **3**[7]:458–463, July 2004. 105, 109

[23] S. Bhattacharya, R. P. Hermann, V. Keppens, T. M. Tritt, and G. J. Snyder. **Effect of disorder on the thermal transport and elastic properties in thermoelectric Zn_4Sb_3**. *Phys. Rev. B*, **74**[13]:134108–, October 2006. 105

[24] T. Caillat, J.-P. Fleurial, and A. Borshchevsky. % bf Preparation and thermoelectric properties of semiconducting Zn_4Sb_3. *J. Phys. Chem. Solids*, **58**[7]:1119–1125, July 1997. 105

[25] J. Xie, X.B. Zhao, G.S. Cao, M.J. Zhao, Y.D. Zhong, and L.Z. Deng. % bf Electrochemical lithiation and delithiation of $FeSb_2$ anodes for lithium-ion batteries. *Mater. Lett.*, **57**[30]:4673–4677, 2003. 105

[26] J. Xie, X.B. Zhao, H.M. Yu, H. Qi, G.S. Cao, and J.P. Tu. % bf Low temperature solvothermal synthesis of nanosized NiSb as a Li-ion battery anode material. *J. Alloys Compd.*, **441**[1-2]:231–235, 2007. 105

[27] P Sun, N Oeschler, S Johnsen, B B Iversen, and F Steglich. **Thermoelectric properties of the narrow-gap semiconductors FeSb 2 and RuSb 2 : A comparative study**. *Journal of Physics: Conference Series*, **150**[1]:012049, 2009. 105

[28] Chunhui Li, Jin Hu, Qing Peng, and Xun Wang. % bf Synthesis and characterization of nanocrystalline NiSb and NiSb2 at low temperature. *Mater. Chem. Phys.*, **110**[1]:106–109, 2008. 105

[29] M. S. Dresselhaus, G. Chen, M. Y. Tang, R. G. Yang, H. Lee, D. Z. Wang, Z. F. Ren, J. P. Fleurial, and P. Gogna. **New Directions for Low-Dimensional Thermoelectric Materials**. *Adv. Mater.*, **19**[8]:1043–1053, 2007. 105

[30] B. Poudel, Q. Hao, Y. Ma, Y. Lan, A. Minnich, B. Yu, X. Yan, D. Wang, A. Muto, D. Vashaee, X. Chen, J. Liu, M. S. Dresselhaus, G. Chen, and Z. Ren. **High-Thermoelectric Performance of Nanostructured Bismuth Antimony Telluride Bulk Alloys**. *Science*, **320**[5876]:634–638, 2008. 105

[31] G. H. Zhu, H. Lee, Y. C. Lan, X. W. Wang, G. Joshi, D. Z. Wang, J. Yang, D. Vashaee, H. Guilbert, A. Pillitteri, M. S. Dresselhaus, G. Chen, and Z. F. Ren. **Increased Phonon Scattering by Nanograins and Point Defects in Nanostructured Silicon with a Low Concentration of Germanium**. *Phys. Rev. Lett.*, **102**[19]:196803, May 2009. 105

[32] X. W. Wang, H. Lee, Y. C. Lan, G. H. Zhu, G. Joshi, D. Z. Wang, J. Yang, A. J. Muto, M. Y. Tang, J. Klatsky, S. Song, M. S. Dresselhaus, G. Chen, and Z. F. Ren. **Enhanced thermoelectric figure of merit in nanostructured n-type silicon germanium bulk alloy**. *Appl. Phys. Lett.*, **93**[19]:193121–3, November 2008. 105

[33] G. Kieslich, C. S. Birkel, A. Stewart, U. Kolb, and W. Tremel. **Solution Synthesis of Nanoparticular Binary Transition Metal Antimonides**. *ChemInform*, **42**[39], 2011. 106, 109, 110

[34] C. S. Birkel, Gr. Kieslich, D. Bessas, T. Claudio, R. Branscheid, U. Kolb, M. Panthöfer, R. P. Hermann, and W. Tremel. **Wet Chemical Synthesis and a Combined X-ray and Mössbauer Study of the Formation of $FeSb_2$ Nanoparticles**. *Inorg. Chem.*, **50**[22]:11807–11812, October 2011. 106, 110

[35] C. S. Birkel, E. Mugnaioli, T. Gorelik, U. Kolb, M. Panthöfer, and W. Tremel. **Solution Synthesis of a New Thermoelectric $Zn_{1+x}Sb$ Nanophase and Its Structure Determination Using Automated Electron Diffraction Tomography**. *J. Am. Chem. Soc.*, **132**[28]:9881–9889, June 2010. 106, 109, 110

[36] H.-C. Wille, Yu. V. Shvyd'ko, E. E. Alp, H. D. Rüter, O. Leupold, I. Sergueev, R. Rüffer, A. Barla, and J. P. Sanchez. **Nuclear resonant forward scattering of synchrotron radiation from ^{121}Sb at 37.13 keV**. *Europhys. Lett.*, **74**[1]:170, 2006. 106

[37] H.-C. Wille, R. P. Hermann, I. Sergueev, O. Leupold, P. van der Linden, B. C. Sales, F. Grandjean, Gary J. Long, R. Rüffer, and Yu. V. Shvyd'ko. **Antimony vibrations in skutterudites probed by ^{121}Sb nuclear inelastic scattering**. *Phys. Rev. B*, **76**[14]:140301, Oct 2007. 106

[38] R. Rüffer and A. Chumakov. **Nuclear Resonance Beamline at ESRF**. *Hyperfine Interact.*, **97-98**:589–604, 1996. 106

[39] I. Sergueev, H.-C. Wille, R. P. Hermann, D. Bessas, Yu. V. Shvyd'ko, M. Zajac, and R. Rüffer. **Milli-electronvolt monochromatization of hard X-rays with a sapphire backscattering monochromator**. *J. Synchrotron Radiat.*, **18**[5]:802–810, Sep 2011. 106

[40] V.G. Kohn and A.I. Chumakov. **DOS: Evaluation of phonon density of states from nuclear resonant inelastic absorption**. *Hyperfine Interact.*, **125**:205–221, 2000. 106

[41] M. S. Diakhate, R. P. Hermann, A. Möchel, I. Sergueev, M. Søndergaard, M. Christensen, and M. J. Verstraete. **Thermodynamic, thermoelectric, and magnetic properties of $FeSb_2$: A combined first-principles and experimental study**. *Phys. Rev. B*, **84**[12]:125210, September 2011. 109

[42] N. Lazarevic, M. M. Radonjic, D. Tanaskovic, Rongwei Hu, C. Petrovic, and Z. V. Popovic. **Lattice Dynamics of FeSb2**. *Submitted*, 2011. 109

[43] A. Möchel, I. Sergueev, H.-C. Wille, F. Juranyi, H. Schober, W. Schweika, S.R. Brown, S.M. Kauzlarich, and R.P. Hermann. **Lattice dynamics in the thermoelectric Zintl compound Yb14MnSb11**. *Phys. Rev. B: Condens. Matter Mater. Phys.*, **84**[18]:184303–, November 2011. 109

[44] Arne Kjekshus and Kjell P. Walseth. **On the Properties of the Cr(1+x)Sb, Fe(1+x)Sb, Co(1+x)Sb, Ni(1+x)Sb, Pd(1+x)Sb, and Pt(1+x)Sb Phases**. *Acta Chem. Scand.*, **23**:2621?2630, 1969. 109

[45] T. Claudio, G. Schierning, R. Theissmann, H. Wiggers, H. Schober, M. M. Koza, and R. P. Hermann. **Effects of impurities on the lattice dynamics of nanocrystalline silicon for thermoelectric application**. pages 1–10–, 2012. 109

[46] I. Sergueev and R. P. Hermann. **Private communication**. 109

[47] R. Rüffer and A. I. Chumakov. **Nuclear inelastic scattering**. *Hyperfine Interact.*, **128**:255–272, 2000. 10.1023/A:1012643918108. 109

[48] R. P. Hermann, F. Grandjean, and G. J. Long. **Einstein oscillators that impede thermal transport**. *Am. J. Phys.*, **73**[2]:110–118, February 2005. 110

Chapter 6

Conclusions and Outlook

The effects of nanostructuration on the lattice dynamics of bulk thermoelectric silicon-based materials and nanopowder antimonides were studied.

Exposing Si nanopowder prepared by a gas phase synthesis to air before sintering lead to a significant amount of SiO_2 and H impurities in the samples, resulting in a strongly reduced thermal conductivity but also reduced electronic properties of the material. Although the thermoelectric properties were not optimal, the study of the lattice dynamics showed that it is possible to evaluate the presence of amorphous SiO_2 since its contribution appeared as a Boson peak characteristic for amorphous materials. Furthermore, PDF is a suitable method to determine the average quantity of such impurities on the Si sample due the the bond length difference between Si-Si and Si-O.

Handling the Si nanopowder in an inert atmosphere throughout the production process resulted in nanocrystalline materials free of impurities. The Si samples prepared with this method showed a dependence of the thermoelectric properties on sintering time and on initial nanoparticles size. Overall, a decrease on the speed of sound was obtained upon nanostructuration resulting in a decrease also in the thermal conductivity. Compared with previously reported results on nanocrystalline Si, the samples still present a somewhat large thermal conductivity. This is however compensated by a very high power factor, giving a peak ZT of 0.57 at 973°C.

Similarly, nanostructuration combined with a 20% substitution of Si atoms by Ge atoms causes a significant reduction on the speed of sound, resulting in a 50% reduction of the thermal conductivity when compared with the bulk material. The figure of merit ZT peaked with 0.88 at a temperature of 900°C. Although the thermoelectric properties of Si-Ge are better when compare to pure Si, the latter still presented a rather large thermal conductivity, so that further optimization of the parameters leading to the reduction of the thermal conductivity could lead to an improvement of the peak ZT. Si has the advantage of being approximately 14 times cheaper than Si-Ge, and its production being more easily scalable, making it an excellent candidate for large-scale industrial application.

While silicon-based materials are used on high-temperature thermoelectric devices, antimonides such as Zn_4Sb_3 is a well-know material for room-temperature application and $FeSb_2$ has a colossal Seebeck coefficient at 12 K.

Nanopowders of $Zn_{1+x}Sb$, $FeSb_2$ and NiSb, prepared by a wet chemistry route, were studied. An increase of the Debye level in comparison with the bulk counterpart and therefore a decrease of the speed of sound was systematically observed – as in the case of nanocrystalline bulk materials. Such a study indicates that not only grain boundaries can affect the

lattice thermal conductivity of a material, but also a reduction in the speed of sound can also be observed in the nanoparticles themselves. An enhancement of the thermoelectric figure of merit is therefore expected, provided that the nanoparticles can be sintered while preserving their nanostructure, and the impurities from the wet chemistry process are kept to a minimum.

It is evident that thermoelectrics should be treated as semiconductors from a materials science point of view. That means that undesired impurities have to be avoided as far as possible, since they degrade the electronic properties – conductivity and Seebeck coefficient. This is particularly problematic for nanopowders, because they adsorb and react with impurities from surrounding media in large quantities during synthesis and handling, since they have a huge surface area. Gas phase synthesis is therefore more promising than wet chemical routes, where it is hard to avoid that precursors, side products or reaction media are incorporated into the final product. Furthermore, it is a continuous and a more easily scalable method, being therefore the preferred method for industrial applications.

Further research on the effects of nanostructuration on the lattice dynamics of Si is suggested, in order to achieve minimum possible value of thermal conductivity without negatively influencing the power factor. Research in this area should include the production of nanopowder with different nanoparticles sizes, *e.g.*, a mixture of 30 and 100 nm nanoparticles, and optimization of sintering parameters to achieve the least possible amount of defects formation and grain-growth during sintering.

Furthermore, research on the optimization of the wet chemistry routes towards nanoparticles production, leading ultimately to impurities free nanoparticles is also suggested. Such study should be followed by an optimization of the sintering parameters of the antimonides nanoparticles resulting into ideally dense nanocrystalline samples.

Appendix A

$FeSb_2$ and Sb_2O_3

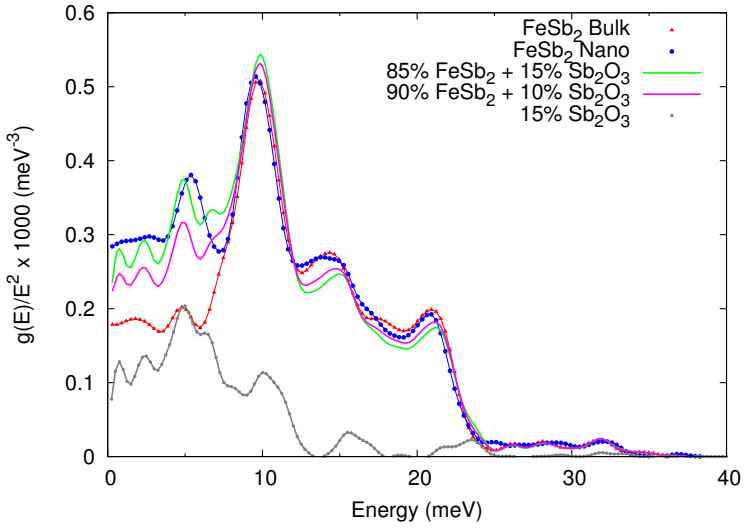

Figure A.1: Reduced density of phonon states of nano and bulk $FeSb_2$, Sb_2O_3 and sums of bulk $FeSb_2$ with Sb_2O_3: 85 + 15% and 90 + 10%.

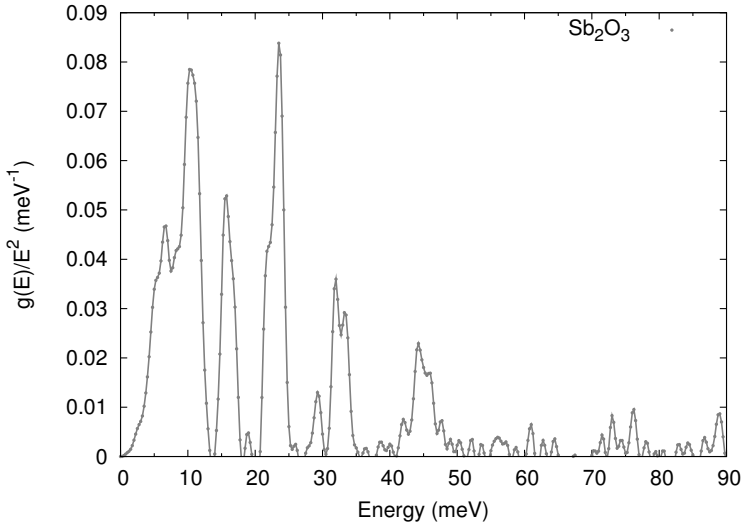

Figure A.2: Density of phonon states of Sb_2O_3 [1]

References

[1] I. Sergueev and R. P. Hermann. **Private communication**. xviii, 121

Vita

Tania Claudio Weber was born on September 16th 1980 in São Paulo, Brazil. She received her undergraduate diploma in Physics / Medical Physics from the Pontifícia Universidade Católica de São Paulo (PUC-SP) in December 2005. In May 2008 she was awarded Master of Materials Science and Engineering from the Christian-Albrechts-Universität zu Kiel, with a master thesis on "Nanocomposite Coatings for Dental Implants" under the supervision of Prof. Dr. Rainer Adelung. She carried out her doctoral research at the Forschungszentrum Jülich and the University of Liège under the supervision of Dr. Raphaël Hermann.

Publication list

2013

1. Claudio, T.; Stein, N.; Stroppa, D. G.; Klobes, B.; Koza, M. M.; Kudejova, P.; Petermann, N.; Wiggers, H.; Schierning, G. and Hermann, R. P., **Nanocrystalline Silicon: Lattice Dynamics and Enhanced Thermoelectric Properties**, *Submitted to: Energy & Environmental Science.*
2. Claudio, T.; Schierning, G.; Theissmann, R.; Wiggers, H.; Schober, H.; Koza, M. M. and Hermann, R. P., **Effects of Impurities on the Lattice Dynamics of Nanocrystalline Si for Thermoelectric Application**, *Journal of Materials Science, Springer US*, **48**: 2836 – 2845, 2013.

2011

3. Birkel, C. S.; Kieslich, G.; Bessas, D.; Claudio, T.; Branscheid, R.; Kolb, U.; Panthöfer, M.; Hermann, R.; Tremel, W., **Wet chemical synthesis and a combined X-ray and Mössbauer study of the formation of $FeSb_2$ nanoparticles**, *Inorganic Chemistry*, **50**: 11807 – 11812, 2011.
4. Birkel, C. S.; Claudio, T.; Panthöfer, M.; Birkel, A.; Koll, D.; Kieslich, G.; Schmidt, J.; Hermann, R.; Tremel, W., **Properties of spark plasma sintered nanostructured $Zn_{1+x}Sb$**, *Physica Status Solidi A*, **208**: 1913 – 1919, 2011.

2010

5. Schierning, G.; Claudio, T.; Theissmann, R.; Stein, N.; Petermann, N.; Becker, A.; Denker, J.; Wiggers, H.; Hermann, R.; Schmechel, R., **Nanocrystalline silicon compacted by spark-plasma sintering: Microstructure and thermoelectric properties**, *MRS Proceedings*, **1267**: DD01–09, 2010.
6. Wille, H. C.; Hermann, R.; Sergueev, I.; Pelzer, U.; Mchel, A.; Claudio, T.; Persson, J.; Rffer, R.; Said, A.; Shvydko, Yu., **Nuclear forward and inelastic spectroscopy on ^{125}Te and $Sb_2{}^{125}Te_3$**, *Europhysics Letters*, **91**: 62001, 2010.